Diffuse Reflectance Spectroscopy for Spine-Surgical Guidance

Losch, M.S.

DOI
10.4233/uuid:2956ebb9-25aa-4432-9766-ee3221f23ff1

Publication date
2024

Document Version
Final published version

Citation (APA)
Losch, M. S. (2024). *Diffuse Reflectance Spectroscopy for Spine-Surgical Guidance*. [Dissertation (TU Delft), Delft University of Technology]. https://doi.org/10.4233/uuid:2956ebb9-25aa-4432-9766-ee3221f23ff1

Important note
To cite this publication, please use the final published version (if applicable).
Please check the document version above.

Diffuse Reflectance Spectroscopy for Spine-Surgical Guidance

Merle Sophie Losch

Diffuse Reflectance Spectroscopy for Spine-Surgical Guidance

Dissertation

for the purpose of obtaining the degree of doctor
at Delft University of Technology
by the authority of the Rector Magnificus Prof. dr. ir. T.H.J.J. van der Hagen
chair of the Board for Doctorates
to be defended publicly on
Monday 9 December 2024 at 10:00 o'clock

by

Merle Sophie LOSCH

Master of Science in Mechanical Engineering,
RWTH Aachen University, Germany &
Ingénieure de l'École Centrale de Marseille, France
born in Aachen, Germany.

This dissertation has been approved by the promotors.

Composition of the doctoral committee:

Rector Magnificus	*chairperson*
Prof. dr. J. Dankelman	Delft University of Technology, *promotor*
Prof. dr. B.H.W. Hendriks	Delft University of Technology, *promotor*
Independent members:	
Prof. dr. S. Andersson-Engels	Tyndall National Institute, Ireland
Dr. N. Bhattacharya	Delft University of Technology
Prof. dr. ir. P. Breedveld	Delft University of Technology
Dr. T.M. van Ginhoven	Erasmus Medical Center
Other members:	
Dr. A. Elmi Terander	Karolinska Institutet, Sweden
Reserve member:	
Prof. dr. J.J. van den Dobbelsteen	Delft University of Technology

Keywords: diffuse reflectance spectroscopy, fiber optics, tissue sensing, surgical guidance, spinal fusion, medical devices

Cover design: Twenty-Four Seven Studio.

Printed by: Gildeprint.

The research leading to these results has received funding from the Netherlands Organisation for Scientific Research, domain Applied and Engineering Sciences under grant agreement No. NWO-TTW 17553.

ISBN: 978-94-6496-278-9

An electronic version of this dissertation is available at repository.tudelft.nl/.

TABLE OF CONTENTS

SUMMARY

As people's life expectancy increases, more individuals will develop degenerative diseases over their lifetime. Surgeries like spinal fusion can help manage these diseases to improve mobility and alleviate pain in the aging population. During spinal fusion, two or more adjacent vertebrae are connected to stabilize part of the spine. Since it takes several months for the bones to grow together, connecting rods and pedicle screws provide support in the meantime. Inserting these screws into the vertebrae is a delicate procedure that, if not done correctly, could harm nearby nerves and blood vessels. To find the correct screw trajectory, surgeons rely on tactile feedback and their experience, as they cannot see inside the body. To support surgeons and enhance safety, the procedure can be guided by technology. Although surgical navigation systems exist, their high cost is a barrier to widespread use. A simple and affordable alternative is tissue sensing technology, which provides insights into the structure and composition of the tissue being examined. This information helps detect the border of the vertebra during spinal fusion to prevent breaches into surrounding tissue. Even where surgical navigation is available, tissue sensing offers an extra layer of safety, for instance, if the spine has moved during surgery.

Diffuse Reflectance Spectroscopy (DRS) is a tissue sensing method that uses light to examine tissue properties. After illuminating the tissue with a broad spectrum of light, the light enters the tissue, where it is partially absorbed and partially redirected to the surface. This interaction creates a diffuse reflectance spectrum unique to each type of tissue, and the spectral shape reveals the tissue composition. In bone, the spectrum is mainly influenced by the amounts of fat, water, and collagen. This simple principle requires minimal modifications to surgical instruments to include two optical fibers, which will be connected to an external DRS console housing a light source and spectrometer.

This PhD research aimed to apply DRS for sensing tissues to detect breaches during spinal fusion. Previous research suggests fat content as a potential criterion to distinguish tissues in spine surgery, but the distribution of fat in the spine is unknown. In a preliminary study, we

therefore assessed the distribution of fat at all vertebral levels in six human cadavers using the Proton Density Fat Fraction (PDFF) from fat and water MR images. By grouping the PDFF readings according to their proximity to the vertebra contour, we established a relationship between fat content and distance from the cortical bone boundary. These initial findings set the foundation for developing a DRS device for spine surgery.

We further investigated the potential of DRS for directional tissue sensing by exploring a common challenge in fiber-optic medical devices: controlling the propagation direction of light. While DRS is simple and compatible with fiber optics, directing light emission and light collection for tissue sensing remains difficult. To address this, we reviewed the patent literature of the last two decades (2001-2021) and found a variety of innovative designs for light beam steering. We focused on the working principles (refraction/reflection, scattering, diffraction) and design strategies (within fiber, at fiber end, outside fiber) employed by the inventors. Our review provides a comprehensive overview of current light beam steering techniques and highlights opportunities for further research. We can apply these insights to build a DRS probe with confined dimensions.

Before developing our own DRS probe, we examined prior attempts to use DRS for detecting breaches in spine surgery. Previous research focused on perpendicular breaches, but overlooked breaches that can also occur at acute angles to the probe tip, which highlights the importance of directional tissue sensing. We therefore investigated how angulating the emitting fiber in DRS affects the probed volume. Our results from Monte Carlo (MC) simulations, absorption experiments, and optical phantom experiments show that outward angulation of fibers is beneficial in acute breach scenarios, while perpendicular breach detection is independent of fiber angulation. These findings demonstrate that a DRS probe with just two fibers can detect both perpendicular and acute breaches, supporting our goal of designing a simple breach detection device.

Building on this promising fiber configuration and our insights from reviewing light-beam steering, we developed a novel fiber-optic probe capable of providing directional tissue feedback by sensing in multiple

directions. Our probe design incorporates three fibers with modified tips optimized for diffuse light emission, forward light collection, and sideways light collection. This allows for directional light emission and collection despite the probe's confined dimensions. Experiments on an optical tissue phantom demonstrated that our DRS probe can detect breaches impending from the front and the side, confirming its capability for directional tissue sensing.

Miniaturizing the probe tip that steers light allows the probe to be flexible rather than rigid. This miniature tip can be combined with flexible tubing, enabling the creation of DRS probes with different shaft stiffnesses. Validating the sensing capabilities on various porcine tissues, including cancellous and cortical bone, demonstrated that this probe could provide directional tissue sensing to guide surgeons in a variety of procedures. This advancement supports DRS as a valid alternative to existing surgical guidance systems.

To incorporate DRS into spine surgery, the technology must seamlessly integrate into surgical workflows. Fiber optics allows DRS to be included in pedicle probes used during pedicle cannulation. Through MC simulations and optical phantom experiments, we assessed the impact of different tip shapes on breach detection. Comparing cone-shaped and single bevel tips to a blunt probe, we observed a gradual decrease in optical probing depth and signal-to-noise ratio (SNR) with sharper tips. However, a single bevel tip with a 30° angle strikes a balance between mechanical performance, optical probing depth, and SNR. A cone-shaped design with a larger diameter and one fiber placed at the tip also presents a viable option. These findings underscore the potential to retrofit pedicle probes with DRS, marking an important first step towards the practical integration of DRS in the operating room (OR).

Exploring the integration of DRS into a fiber-optic pedicle probe, we recognized that current DRS setups are impractical for OR use due to their bulky consoles. To address this, we attempted to integrate all necessary technology into a handheld fiber-optic probe. Our design includes laser diodes at two distinct wavelengths for tissue illumination, a photodiode for measuring collected light, a microcontroller and PCB to operate the

components, and a buzzer for audio feedback. Validation of the electronic and optical components revealed challenges with fiber coupling but demonstrated successful light emission and collection, confirming the feasibility of providing real-time tissue feedback during spine surgical procedures in a compact and affordable device.

By consolidating insights gained across our various projects, we can develop an ideal DRS probe for pedicle screw placement. This involves creating an ergonomically designed handheld probe with a sharp tip for tissue penetration and integrating fibers with modified tips to steer light for directional tissue feedback. With such a prototype, the next steps of clinical validation, regulatory compliance, and commercialization can be accomplished. This innovation promises to enhance accuracy and safety in spinal fusion surgery.

SAMENVATTING

Naarmate de levensverwachting toeneemt, zullen meer mensen in de loop van hun leven degeneratieve ziekten ontwikkelen. Operaties zoals een spinale fusie (verstijvingsoperatie van de wervelkolom) kunnen deze ziekten helpen beheersen om de mobiliteit te verbeteren en de pijn bij de ouder wordende bevolking te verlichten. Bij een spinale fusie worden twee of meer aangrenzende wervels met elkaar verbonden om een deel van de wervelkolom te stabiliseren. Omdat het enkele maanden duurt voordat de botten aan elkaar zijn gegroeid, bieden verbindingsstangen en wervelschroeven steun in de tussentijd. Het inbrengen van deze schroeven in de wervels is een delicate procedure die, als het niet correct gebeurt, schade kan toebrengen aan nabijgelegen zenuwen en bloedvaten. Chirurgen vertrouwen op tactiele feedback en ervaring om het juiste schroeftraject te vinden, aangezien ze niet in het lichaam kunnen kijken. De procedure kan geleid worden door technologie om chirurgen te ondersteunen en de veiligheid te vergroten. Hoewel er chirurgische navigatiesystemen bestaan, vormen hun hoge kosten een belemmering voor wijdverspreid gebruik. Een eenvoudig en betaalbaar alternatief is weefseldetectietechnologie, die inzicht geeft in de structuur en samenstelling van het onderzochte weefsel. Deze informatie helpt bij het detecteren van de rand van de wervel tijdens spinale fusie om breuken in het omringende weefsel te voorkomen. Zelfs als chirurgische navigatie beschikbaar is, biedt weefseldetectie een extra laag van beveiliging, bijvoorbeeld als de wervelkolom beweegt tijdens de operatie.

Diffuse reflectie spectroscopie (DRS) is een weefseldetectiemethode waarbij licht wordt gebruikt om weefseleigenschappen te onderzoeken. Nadat het weefsel met een breed lichtspectrum is belicht, dringt het licht het weefsel binnen, waar het gedeeltelijk wordt geabsorbeerd en gedeeltelijk naar het oppervlak wordt omgeleid. Deze interactie creëert een diffuus reflectiespectrum dat uniek is voor elk type weefsel, en de spectrale vorm onthult de samenstelling van het weefsel. In bot wordt het spectrum voornamelijk beïnvloed door de hoeveelheid vet, water en collageen. Dit eenvoudige principe vereist slechts minimale aanpassingen aan chirurgische instrumenten om twee optische vezels toe te voegen,

die worden aangesloten op een externe DRS-console met een lichtbron en spectrometer.

Dit promotieonderzoek was gericht op het toepassen van DRS voor weefseldetectie om breuken te detecteren tijdens spinale fusie. Eerder onderzoek suggereert dat het vetgehalte als een potentieel criterium gebruikt kan worden om weefsels te onderscheiden bij wervelkolomchirurgie, maar de verdeling van vet in de wervelkolom is onbekend. In een voorbereidende studie hebben we daarom de verdeling van vet op alle wervelniveaus in zes menselijke kadavers beoordeeld met behulp van de protondichtheid vetfractie (PDFF) uit MR-beelden van vet en water. Door de PDFF-metingen te groeperen volgens hun nabijheid tot de wervelcontour, stelden we een verband vast tussen vetgehalte en afstand tot de corticale botgrens. Deze eerste bevindingen vormden de basis voor de ontwikkeling van een DRS-apparaat voor wervelkolomchirurgie.

We onderzochten verder het potentieel van DRS voor directionele weefseldetectie door het onderzoeken van een veelvoorkomende uitdaging in vezeloptische medische apparatuur: het sturen van de voortplantingsrichting van licht. Hoewel DRS eenvoudig en compatibel is met vezeloptica, blijft het sturen van lichtemissie en -verzameling voor weefseldetectie moeilijk. Om dit aan te pakken hebben we de octrooiliteratuur van de afgelopen twee decennia (2001-2021) doorgenomen en vonden we een verscheidenheid aan innovatieve ontwerpen voor het sturen van lichtbundels. We hebben ons gericht op de werkingsprincipes (breking/reflectie, verstrooiing, diffractie) en ontwerpstrategieën (binnen de vezel, aan het uiteinde van de vezel, buiten de vezel) die door de uitvinders werden toegepast. Ons overzicht geeft een uitgebreid overzicht van de huidige technieken voor het sturen van lichtbundels en benadrukt mogelijkheden voor verder onderzoek. We kunnen deze inzichten toepassen om een DRS-sonde met beperkte afmetingen te bouwen.

Voordat we onze eigen DRS-sonde ontwikkelden, onderzochten we eerdere pogingen om DRS te gebruiken voor het detecteren van breuken in de wervelkolomchirurgie. Eerder onderzoek richtte zich op loodrechte

breuken, maar zag over het hoofd dat breuken ook kunnen optreden onder een scherpe hoek ten opzichte van de sondetip, wat het belang benadrukt van gerichte weefseldetectie. We hebben daarom onderzocht hoe het onder een hoek plaatsen van de emitterende vezel in DRS het gesondeerde volume beïnvloedt. Onze resultaten van Monte Carlo (MC) simulaties, absorptie-experimenten en optische fantoomexperimenten laten zien dat een buitenwaartse hoek van vezels gunstig is bij acute breukscenario's, terwijl de detectie van loodrechte breuken onafhankelijk is van de hoek van de vezels. Deze bevindingen tonen aan dat een DRS-sonde met slechts twee vezels zowel loodrechte als acute breuken kan detecteren, wat ons doel ondersteunt om een eenvoudig apparaat te ontwerpen voor het detecteren van breuken.

Voortbouwend op deze veelbelovende vezelconfiguratie en onze inzichten van het onderzoeken van lichtstraalbesturing, hebben we een nieuwe optische vezelsonde ontwikkeld die in staat is om gerichte weefselfeedback te geven door in meerdere richtingen te meten. Ons sonde-ontwerp bevat drie vezels met punten die geoptimaliseerd zijn voor diffuse lichtemissie, voorwaartse lichtopvang en zijwaartse lichtopvang. Dit maakt directionele lichtemissie en -verzameling mogelijk ondanks de beperkte afmetingen van de sonde. Experimenten op een optisch weefselfantoom toonden aan dat onze DRS-sonde breuken kan detecteren die van voren en van opzij komen, wat de mogelijkheid voor gerichte weefseldetectie bevestigt.

Door het miniaturiseren van de sondepunt die het licht stuurt is de sonde flexibel in plaats van stijf. Deze miniatuurtip kan gecombineerd worden met flexibele slangen, waardoor DRS-sondes met verschillende schachtstijfheden gemaakt kunnen worden. Het valideren van de detectiecapaciteiten op verschillende varkensweefsels, waaronder spongieus en corticaal bot, toonde aan dat deze sonde directionele weefseldetectie kan bieden om chirurgen te begeleiden bij een verscheidenheid aan procedures. Deze vooruitgang ondersteunt DRS als een geldig alternatief voor bestaande chirurgische geleidingssystemen.

Om DRS te integreren in de wervelkolomchirurgie moet de technologie naadloos worden geïntegreerd in de chirurgische workflows.

Glasvezeloptica maakt het mogelijk DRS op te nemen in pedikelsondes die worden gebruikt tijdens pedikelcanulaties. Door middel van MC-simulaties en optische fantoomexperimenten hebben we de invloed van verschillende tipvormen op breukdetectie beoordeeld. Bij de vergelijking van kegelvormige en enkelvoudige schuine punten met een stompe sonde zagen we een geleidelijke afname in optische sondediepte en signaal-ruisverhouding (SNR) met scherpere punten. Een enkele schuine punt met een hoek van 30° zorgt echter voor een balans tussen mechanische prestaties, optische diepte en SNR. Een kegelvormig ontwerp met een grotere diameter en één vezel aan de tip is ook een haalbare optie. Deze bevindingen benadrukken het potentieel om pedikelsondes achteraf uit te rusten met DRS en markeren een belangrijke eerste stap naar de praktische integratie van DRS in de operatiekamer (OK).

Bij het verkennen van de integratie van DRS in een vezeloptische pedikelsonde erkenden we dat de huidige DRS-opstellingen onpraktisch zijn voor gebruik in de OK vanwege hun omvangrijke consoles. Om dit aan te pakken hebben we geprobeerd om alle benodigde technologie te integreren in een handzame optische vezelsonde. Ons ontwerp bevat laserdiodes met twee verschillende golflengtes voor weefselverlichting, een fotodiode voor het meten van verzameld licht, een microcontroller en PCB om de componenten te bedienen en een zoemer voor audiofeedback. Validatie van de elektronische en optische componenten bracht problemen met vezelkoppeling aan het licht, maar toonde succesvolle lichtemissie en -verzameling, wat de mogelijkheid bevestigt om real-time weefselfeedback te geven tijdens chirurgische procedures aan de wervelkolom in een compact en betaalbaar apparaat.

Door de inzichten uit onze verschillende projecten te combineren, kunnen we een ideale DRS-sonde ontwikkelen voor het plaatsen van wervelschroeven. Dit omvat het maken van een ergonomisch ontworpen handsonde met een scherpe punt voor weefselpenetratie en het integreren van vezels met aangepaste punten om licht te sturen voor gerichte weefselfeedback. Met een dergelijk prototype kunnen de volgende stappen van klinische validatie, naleving van de regelgeving en commercialisering worden bereikt. Deze innovatie belooft de nauwkeurigheid en veiligheid bij spinale fusiechirurgie te verbeteren.

ZUSAMMENFASSUNG

Mit steigender Lebenserwartung entwickeln immer mehr Menschen im Laufe ihres Lebens degenerative Erkrankungen. Durch chirurgische Eingriffe wie etwa eine Wirbelsäulenversteifung können diese Krankheiten behandelt werden, um die Beweglichkeit der alternden Bevölkerung zu erhalten und Schmerzen zu lindern. Bei einer Wirbelsäulenversteifung werden zwei oder mehr benachbarte Wirbel miteinander verbunden, um einen Teil der Wirbelsäule zu stabilisieren. Da es mehrere Monate dauert, bis die Knochen zusammengewachsen sind, stützen in der Zwischenzeit Verbindungsstäbe und Pedikelschrauben die Wirbelsäule. Das Einsetzen dieser Schrauben in die Wirbel ist ein schwieriger Eingriff, da bei falscher Ausführung nahegelegene Nerven und Blutgefäße verletzt werden können. Um die richtige Schraubentrajektorie zu finden, müssen sich die Chirurg*innen auf ihren Tastsinn und ihre Erfahrung verlassen, da sie das Innere des Körpers nicht sehen können. Um die Chirurg*innen bei dem Eingriff zu unterstützen und mehr Sicherheit zu gewährleisten, kann die OP durch Technologie unterstützt werden. Derzeit gibt es zwar chirurgische Navigationssysteme, deren hohe Kosten stehen aber einem großflächigen Einsatz im Wege. Eine einfachere und kostengünstigere Alternative ist die Gewebemesstechnik, die Einblick in Struktur und Zusammensetzung des untersuchten Gewebes gewährt. Durch Gewebemesstechnik gewonnene Informationen ermöglichen es, den Rand des Wirbels während der Wirbelsäulenversteifung zu detektieren und so Verletzungen des umliegenden Gewebes durch unbeabsichtigte Durchbrüche zu verhindern. Selbst dort, wo bereits chirurgische Navigationssysteme zur Verfügung stehen, bringt die Gewebemessung zusätzliche Sicherheit, beispielsweise wenn sich die Wirbelsäule während der Operation bewegt.

Die diffuse Reflexionsspektroskopie (DRS) ist eine Methode der Gewebemessung, bei der Licht zur Untersuchung von Gewebeeigenschaften verwendet wird. Nachdem das Gewebe mit einem breiten Lichtspektrum beleuchtet wurde, dringt das Licht in das Gewebe ein, wo es teilweise absorbiert und teilweise an die Oberfläche zurückgestrahlt wird. Durch diese Interaktion entsteht ein diffuses Reflexionsspektrum, das für jeden Gewebetyp einzigartig ist. Die Form

dieses Spektrums lässt Rückschlüsse auf die Gewebezusammensetzung zu. Im Knochen wird es hauptsächlich durch den Gehalt an Fett, Wasser und Kollagen beeinflusst. Um DRS zu nutzen, sind nur minimale Änderungen an den chirurgischen Instrumenten erforderlich: Zwei Glasfasern werden eingebaut, die an eine externe DRS-Konsole angeschlossen werden, welche eine Lichtquelle und ein Spektrometer enthält.

Ziel dieser Doktorarbeit war es, DRS für Gewebemessung einzusetzen, um Durchbrüche bei der Wirbelsäulenversteifungsoperation frühzeitig zu erkennen. Frühere Forschungsarbeiten deuten darauf hin, dass der Fettgehalt ein potenzielles Kriterium für die Unterscheidung von Geweben in der Wirbelsäulenchirurgie sein könnte. Die Verteilung von Fett in der Wirbelsäule ist allerdings bisher noch nicht untersucht worden. In einer ersten Studie haben wir daher die Fettverteilung auf allen Niveaus der Wirbelsäule bei sechs menschlichen Leichen untersucht, und zwar mithilfe des Protonendichte-Fettanteils (PDFF) aus MRT-Bildern von Fett und Wasser. Indem wir die PDFF-Messwerte entsprechend ihrer Nähe zur Wirbelkontur gruppierten, fanden wir einen Zusammenhang zwischen Fettgehalt und Abstand vom kortikalen Knochen. Diese ersten Ergebnisse bilden die Grundlage für die Entwicklung eines DRS-Geräts für die Wirbelsäulenchirurgie.

Wir haben das Potenzial von DRS für die gerichtete Gewebemessung weiter untersucht, indem wir uns mit einer häufig vorkommenden Herausforderung bei faseroptischen medizinischen Geräten beschäftigten: der Steuerung der Ausbreitungsrichtung des Lichts. Zwar ist DRS ein einfaches und mit Faseroptik kompatibles Verfahren, doch ist es nach wie vor schwierig, die Lichtabstrahlung und -sammlung für die Gewebemessung zu steuern. Um dieses Problem zu lösen, haben wir die Patentliteratur der letzten zwei Jahrzehnte (2001-2021) durchgesehen und eine Vielzahl innovativer Designs für die Lichtstrahlsteuerung gefunden. Dabei haben wir uns auf die von der Erfindergruppe verwendeten Wirkprinzipien (Brechung/Reflexion, Streuung, Beugung) und Designstrategien (innerhalb der Glasfaser, am Glasfaserende, außerhalb der Glasfaser) konzentriert. Die gewonnenen Erkenntnisse können wir für den Bau einer DRS-Sonde mit eingeschränkten Abmessungen nutzen.

Bevor wir unsere eigene DRS-Sonde entwickeln konnten, haben wir bisherige Versuche, DRS zur Erkennung von Durchbrüchen in der Wirbelsäulenchirurgie einzusetzen, unter die Lupe genommen. Die bisherige Forschung befasste sich ausschließlich mit rechtwinkligen Durchbrüchen, übersah dabei aber, dass Durchbrüche auch im spitzen Winkel zum Instrument auftreten können, was die Notwendigkeit einer gerichteten Gewebemessung unterstreicht. Wir haben daher untersucht, wie sich bei DRS die Neigung der abstrahlenden Glasfaser auf das gemessene Volumen auswirkt. Unsere Ergebnisse aus Monte-Carlo-(MC)-Simulationen, Absorptionsexperimenten und optischen Phantomexperimenten zeigen, dass eine nach außen gerichtete Neigung der Glasfasern bei spitzen Durchbrüchen von Vorteil ist, während die Erkennung von rechtwinkligen Durchbrüchen unabhängig von der Neigung der Glasfasern möglich ist. Diese Ergebnisse zeigen, dass eine DRS-Sonde mit nur zwei Glasfasern sowohl rechtwinklige als auch spitze Durchbrüche erkennen kann, was uns in unserem Vorhaben bestärkt, ein einfaches Instrument zur Erkennung von Durchbrüchen zu entwickeln.

Auf Grundlage dieser vielversprechenden Glasfaserkonfiguration und unserer Erkenntnisse aus der Durchsicht der Patentliteratur zur Lichtstrahlsteuerung haben wir eine neuartige faseroptische Sonde entwickelt, die in der Lage ist, gerichtetes Gewebefeedback zu liefern, indem sie in mehrere Richtungen misst. Das Design umfasst drei Glasfasern mit angepassten Spitzen, die auf diffuse Lichtabstrahlung, Lichtsammlung in Vorwärtsrichtung und Lichtsammlung in seitlicher Richtung ausgelegt sind. Dies ermöglicht eine gerichtete Lichtabstrahlung und -sammlung trotz der geringen Abmessungen der Sonde. Optische Phantomexperimente zeigten, dass unsere DRS-Sonde von vorne und von der Seite her bevorstehende Durchbrüche erkennen kann, und somit für die gerichtete Gewebemessung geeignet ist.

Durch eine Miniaturisierung der Sondenspitze, die das Licht steuert, wird die Sonde biegsam statt starr. Diese kleine Spitze kann mit flexiblen Schläuchen kombiniert werden, wodurch DRS-Sonden mit unterschiedlichen Steifigkeiten hergestellt werden können. Durch Validierung der Messfunktion an verschiedenen Schweinegeweben, einschließlich Spongiosa und kortikalem Knochen, konnten wir zeigen,

dass diese Sonde eine gerichtete Gewebemessung ermöglicht, die Chirurg*innen bei einer Vielzahl von Eingriffen unterstützen kann. Dieser Entwicklungsschritt unterstreicht, dass DRS eine echte Alternative zu bestehenden chirurgischen Navigationssystemen darstellt.

Um DRS in der Wirbelsäulenchirurgie einsetzen zu können, muss die Technologie nahtlos in die chirurgischen Arbeitsabläufe integriert werden. Die Faseroptik ermöglicht es, DRS in Pedikelsonden einzubauen, die während der Pedikelkanülierung verwendet werden. Anhand von MC-Simulationen und optischen Phantomexperimenten haben wir untersucht, wie sich verschiedene Spitzenformen auf die Erkennung von Durchbrüchen auswirken. Beim Vergleich von kegelförmigen Spitzen und seitlich abgeschrägten Spitzen mit einer stumpfen Sonde beobachteten wir eine allmähliche Abnahme der Tiefe der Gewebemessung und des Signal-Rausch-Verhältnisses (SRV) mit zunehmender Schärfe der Spitze. Mit einer seitlich abgeschrägten Spitze mit einem Winkel von 30° kann jedoch ein gutes Gleichgewicht zwischen mechanischem Verhalten, Tiefe der Gewebemessung und SRV erreicht werden. Ein kegelförmiges Design mit einem größeren Durchmesser und einer Glasfaser in der Spitze wäre ebenfalls eine gangbare Option. Diese Ergebnisse verdeutlichen, dass Pedikelsonden mit DRS nachgerüstet werden können, und stellen einen wichtigen ersten Schritt dar, DRS im OP zu etablieren.

Als wir untersuchten, ob es möglich wäre, DRS in eine faseroptische Pedikelsonde einzubauen, stellten wir fest, dass die derzeitigen DRS-Geräte aufgrund ihrer sperrigen Konsolen für den Einsatz im OP unpraktisch sind. Deshalb haben wir entschieden, die gesamte erforderliche Technologie in eine tragbare faseroptische Sonde zu integrieren. Unser Prototyp umfasst Laserdioden in zwei verschiedenen Wellenlängen für die Beleuchtung des Gewebes, eine Photodiode zur Messung des gesammelten Lichts, einen Mikrocontroller und eine Leiterplatte zum Betrieb der Komponenten sowie einen Lautsprecher, um ein Tonsignal als Feedback abzugeben. Bei der Validierung der elektronischen und optischen Komponenten zeigten sich Probleme mit der Faserkopplung; die Lichtabstrahlung und -sammlung waren jedoch erfolgreich, wodurch sich bestätigt hat, dass unser kompaktes und

kostengünstiges Gerät in der Lage ist, bei chirurgischen Eingriffen an der Wirbelsäule Gewebefeedback in Echtzeit zu liefern.

Durch die Kombination aller Erkenntnisse, die wir in unseren verschiedenen Projekten gewonnenen haben, können wir eine ideale DRS-Sonde für das Einsetzen von Pedikelschrauben entwickeln. Dazu gehören eine ergonomisch gestaltete, tragbare Sonde mit einer scharfen Spitze zur Durchdringung des Gewebes und die Integration von Glasfasern mit angepassten Spitzen, um das Licht für gerichtetes Gewebefeedback zu lenken. Mit einem solchen Prototypen können die nächsten Schritte wie klinische Validierung, Zulassung und Kommerzialisierung vollzogen werden. Diese Innovation verspricht, die Genauigkeit und Sicherheit bei der Durchführung von Wirbelsäulenversteifungen zu verbessern.

1 INTRODUCTION

Over the last decades, the world has seen a considerable increase in life expectancy [1]. Despite the joy of spending more time with our loved ones, the demographic shift also brings about new challenges. To keep the aging population mobile and pain-free, the need for surgical interventions such as spinal fusion has increased as the last resort for patients who cannot find relief of their degenerative diseases through conservative treatment [2]. A key element of spinal fusion is the accurate placement of pedicle screws, providing stability to the spine during the fusion process, necessitating breach detection to ensure the success and safety of these interventions.

In the upcoming sections of this introduction, we will explore the world of spinal fusion surgery. For those unfamiliar with the field, The first section provides an overview of the anatomy of the spine. Following that, the second section covers spinal fusion, addressing the challenges associated with pedicle screw placement and presenting prevalent guidance systems. Readers already acquainted with spine surgery can join us in the third section, where the concept of tissue sensing for breach detection during pedicle screw placement is introduced. In the fourth section, we specifically discuss Diffuse Reflectance Spectroscopy (DRS) as a candidate for tissue sensing. This sets the stage for the fifth and final section, where we define the aim of this PhD research and present the thesis outline.

SPINE ANATOMY

The spine, also known as the backbone or vertebral column, is one of the defining characteristics of vertebrates, which constitute a diverse group of animals that includes mammals, reptiles, birds, and fish. The spine is composed of a set of bones, the so-called vertebrae, that are stacked on top of each other. The vertebrae are separated by intervertebral disks and interconnected by ligaments and muscles, forming a flexible and robust structure that provides support and protection for the spinal cord. This anatomical feature has evolved over millions of years, enabling vertebrates to adapt to a wide range of environments and ecological niches. Today, approximately 85,000 species of vertebrates are known, each with its unique morphology and functional adaptations [3].

The number of vertebrae varies widely depending on the species: while a snake can have more than 300 vertebrae, certain fish have no true vertebrae at all [4, 5]. Human adults typically have 33 vertebrae. Of these, seven are cervical (neck) vertebrae (denominated C1-C7), 12 are thoracic (chest) vertebrae (denominated T1-T12), five are lumbar (lower back) vertebrae (denominated L1-L5), for a total of 24 movable vertebrae. The other vertebrae constitute sacrum and coccyx. Figure 1.1 illustrates the anatomy of the human spine.

The size and shape of the vertebrae vary between levels to accommodate different anatomic needs related to forces and mobility. In principle, however, each vertebra consists of three main functional components: (1) the oval-shaped vertebral body for load-bearing, (2) the triangular-shaped vertebral arch around the spinal canal formed by pedicles and laminae that protects the spinal cord and contains the facet joints for movement, and (3) the vertebral processes where the ligaments are attached. Figure 1.2 illustrates the anatomy of vertebrae at different levels. Figure 1.3 illustrates a cervical vertebra and the structures surrounding it, specifically the spinal cord, nerves, and blood vessels.

Within the vertebra, the compact outer layer of cortical bone with a thickness of a few hundred microns [6, 7] provides structural integrity and creates a protective shell to the cancellous bone on the inside, a porous framework of trabeculae and bone marrow to limit bone weight and allow

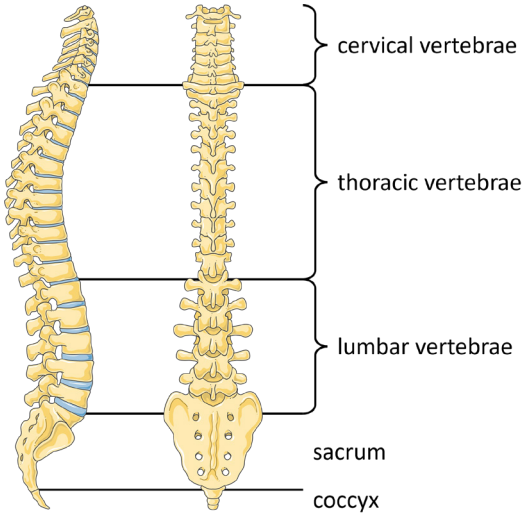

FIGURE 1.1: Spinal column in lateral view (left) and posterior view (right). Illustration adapted from Servier Medical Art under CC attribution license 3.0.

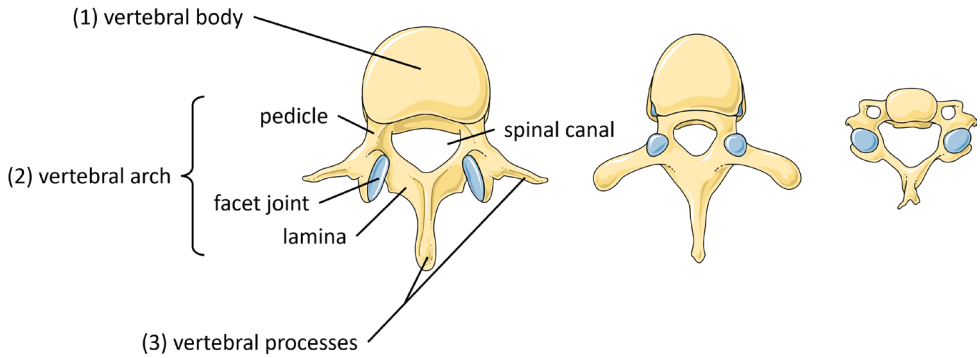

FIGURE 1.2: Anatomy of lumbar vertebra (left), thoracic vertebra (center), and cervical vertebra (right). Illustration adapted from Servier Medical Art under CC attribution license 3.0.

for shock absorption. Cortical bone is primarily composed of mineral hydroxyapatite, with a small (< 10%) organic fraction mainly consisting of the fibrous protein collagen, and water [8]. Cortical bone contains almost no fat [9]. On the other hand, cancellous bone is characterized by 25% mass (55% volume) organic material [10], with lipid fractions accounting for up to 70% [9]. Notably, within this constellation, a transition zone of descending bone density exists between the compact cortical bone and the porous cancellous bone [11], also denominated the pre-cortical zone (PCZ) [9].

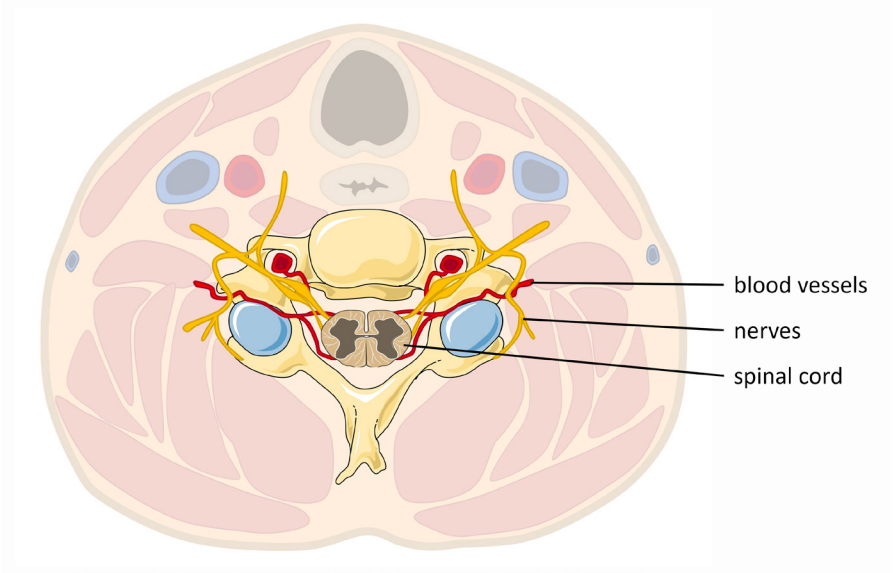

FIGURE 1.3: Cervical vertebra and surrounding structures in axial view. Illustration adapted from Servier Medical Art under CC attribution license 3.0.

As we delve into the anatomy of the spine, it becomes clear that this complex structure plays an important role in supporting and protecting our bodies. However, there are certain occasions in which the vertebral column may require surgical intervention in the form of spinal fusion.

SPINAL FUSION

Need for medical attention may arise for various reasons, such as correcting deformities, alleviating pain, following tumor removal, or in response to an acute traumatic injury [12-15]. To reduce pain or increase spine stability, these medical conditions are typically treated in a surgical intervention known as spinal fusion. This procedure involves connecting adjacent vertebrae to eliminate their movement relative to one another [16]. During the surgery, a spacer enhanced with bone graft may be inserted between the affected vertebrae to support the bones growing together. Figure 1.4 illustrates how pedicle screws and connecting rods are used as a temporary support structure until the vertebrae fuse together completely, a process which can take several months to complete [17].

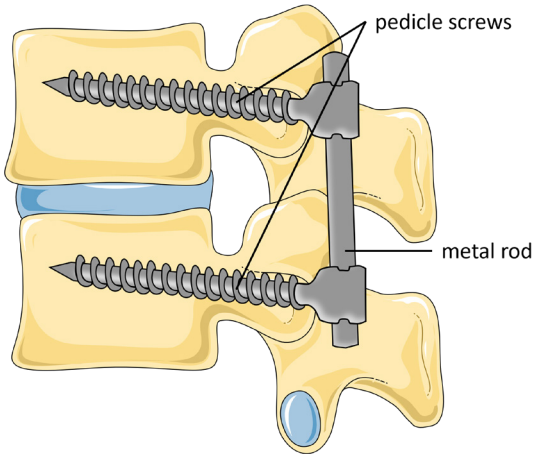

FIGURE 1.4: Spinal fusion between two vertebrae with visible pedicle screws and connecting rod. A second pair of pedicle screws with connecting rod is typically placed symmetrically on the opposite side of the vertebra. Illustration adapted from Servier Medical Art under CC attribution license 3.0.

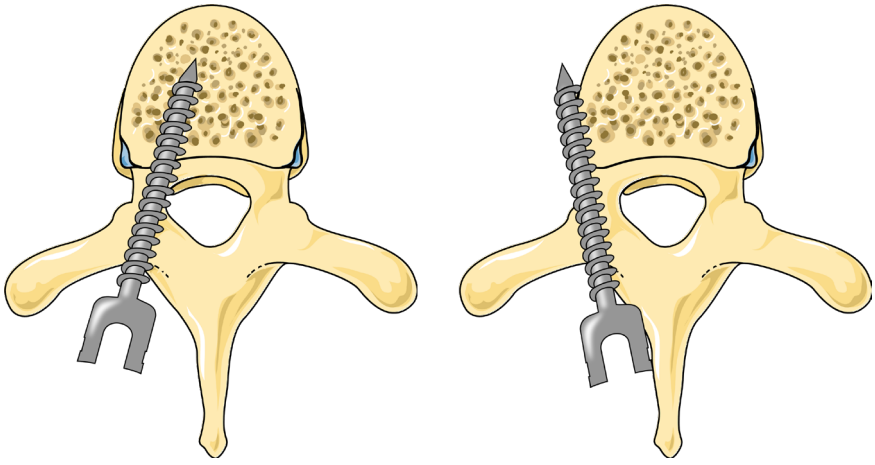

FIGURE 1.5: Pedicle screw misplacement: medial breach (left) and lateral breach (right). Illustration adapted from Servier Medical Art under CC attribution license 3.0.

Among the various steps completed in the course of a spinal fusion procedure, the placement of pedicle screws is the one that has drawn significant attention for technological advancements [18, 19], likely due to the prevalence of surgical errors in this step and the potential for technical solutions to address those errors. Figure 1.5 illustrates a medial breach, where the pedicle screw has penetrated the spinal canal, and a lateral breach, where the pedicle screw missed the vertebral body. Pedicle screw placement requires high accuracy to protect nearby neural and vascular structures [20, 21]. It has traditionally been performed using the freehand technique, which involves identifying relevant anatomical landmarks, such as the vertebral processes and arch, to determine an appropriate entry point. To prevent misplacement of the screws, surgeons rely on tactile feedback and their expertise to accurately distinguish between the softer cancellous bone and the denser, more resistive cortical bone [22]. Thus, screw placement is technically demanding and has a long learning curve [23], given that spinal anatomical landmarks and tactile feedback can be difficult to assess.

Accurate pedicle screw placement is crucial for safe surgery and optimal biomechanical stability, as misplaced screws can cause neurological injury or necessitate revision surgery [24, 25]. However, due to the complexity of the procedure and the significant reliance on the surgeon's anatomical knowledge and level of experience, accuracy rates of free-hand pedicle screw placement vary widely, with a reported misplacement frequency of around 10% [26–28]. To guide pedicle screw insertion, several methods of guidance have therefore been developed. Some of the currently available guidance systems include the use of intraoperative fluoroscopy, computer-assisted navigation, and robot-assisted surgery [24].

Fluoroscopy employs X-rays to generate real-time images of the patient anatomy during the surgical procedure that can be used to visualize pedicle positions and guide the surgeon in screw placement. Despite its utility, the use of fluoroscopy is time-consuming and introduces an added level of radiation exposure, and the accuracy achieved with fluoroscopic guidance is still influenced by factors such as operator experience and the vertebral level of operation [18, 22].

Computer-assisted navigation uses preoperative or intraoperative images to construct a three-dimensional map of the patient's anatomy to guide the placement of pedicle screws. This technology provides a real-time display of the position of surgical instruments in relation to the anatomical structures, creating a map that surgeons use to navigate to the target area during the procedure. In parallel, the field of spinal robotics has emerged, introducing surgical robots that assist with tool positioning during pedicle screw placement. Despite being in its early developmental stages, several commercially available devices, such as the Mazor X Stealth Edition (Medtronic Spine LLC, Memphis (TN), USA), ExcelsiusGPS (Globus Medical Inc, Audubon (PA), USA), and Cirq (Brainlab AG, Munich, Germany), exemplify the ongoing advancements in spinal robotics.

While the process of image registration and differences in patient positioning remain potential sources of error leading to hardware malpositioning, computer-assisted and robot-assisted methods have largely improved the accuracy of pedicle screw placement. However, the adoption of both methods is hindered by the need for expensive equipment, specialized training, and practical experience, which contributes to additional cost and time requirements that await substantiated benefits [29-31]. This limitation prevents widespread access to this technology for many surgeons and healthcare facilities, particularly as imaging within the operating room is not universally available. Based on these commonly used types of surgical guidance, there remains a need for a simple, less resource-intensive device to provide breach detection for pedicle screw placement.

TISSUE SENSING FOR BREACH DETECTION

Integrating tissue sensing into surgical instruments to examine the physical properties of the surrounding tissue, such as its acoustic, optical, mechanical, electromagnetic, or thermal characteristics, provides insights into tissue structure and composition. This information can be leveraged to detect the cortical border of vertebrae. When surgeons are provided with tissue feedback in real-time, they can adjust the trajectory of the pedicle screw to prevent screw misplacement. Such tissue sensing tools

will prove particularly valuable in settings where fluoroscopy, computer-assisted navigation, or surgical robots may not be available or feasible.

In the domain of tissue sensing for spine surgery, the PediGuard (SpineGuard SA, Vincennes, France) is the only commercially available solution to date. This system is based on the principles of Electrical Impedance Spectroscopy (EIS), a technique that assesses the electrical properties of tissues by applying a sinusoidal voltage and measuring the resulting current response. By varying the frequency of the applied signal, EIS can provide information about the tissue's electrical impedance to study properties like conductivity, capacitance, and resistance. Since different tissues have unique impedance profiles, EIS allows for the discrimination between tissues based on their electrical responses. While the PediGuard has pioneered tissue sensing in spine surgery through EIS [32, 33], it faces several challenges. One challenge is the accumulation of blood and tissue products in the pilot hole, *e.g.*, when surgeons reduce probe pressure, which can introduce inaccuracies in detecting electromagnetic fields [32, 34]. As the system can only detect changes in electrical conductivity for tissues in direct contact with the instrument tip, warnings are only possible once a breach is already occurring [32, 35]. These challenges encourage exploration into alternative approaches. Optical spectroscopy, and in particular DRS, stands out as a tissue sensing technology that leverages the interaction of electromagnetic radiation and matter to characterize tissues.

DIFFUSE REFLECTANCE SPECTROSCOPY

In tissue optics, light interacts with tissue through processes such as absorption and scattering. During absorption, light energy is captured inside the tissue, causing energy transitions in molecules to higher energetic states. Absorption depends on the energy matching between incoming light and quantum mechanical Eigenstates of tissue molecules. Infrared (IR) or visible light can induce vibrational state changes, while visible and ultraviolet (UV) light can cause quantum jumps in electronic states. Different tissues exhibit unique absorption patterns due to their different molecular composition. In addition to absorption, scattering plays a crucial role in tissue-light interactions. In contrast to Eigenstates,

scattering involves excitation to short-lived virtual states, leading to elastic or inelastic scattering. Elastic scattering conserves photon energy with changes in propagation direction. For scattering particles small compared to the excitation wavelength, Rayleigh scattering occurs that follows a mostly uniform distribution, whereas Mie scattering and geometric scattering occur for bigger particles and primarily scatter forward. Inelastic scattering, encompassing Stokes and Anti-Stokes scattering, do not conserve photon energy. Stokes scattering transfers energy to vibrational states of scattering molecules, while Anti-Stokes scattering gains energy from the molecule's vibration.

Building upon the principles of tissue optics, DRS is a promising tissue sensing technology. By directing a broad spectrum of light onto the tissue through an optical fiber, DRS induces an interplay of light scattering and absorption within the probed region, as illustrated in Figure 1.6. The interaction with tissue constituents, including cellular structures and chromophores, results in a diffuse reflectance pattern. This pattern carries information about the composition of the tissue, particularly the quantity of the key chromophores fat, water, and collagen, which exhibit varying concentrations in cancellous and cortical bone. A portion of the light is diffusely reflected back to the tissue's surface, where a second optical fiber collects the spectrum resulting from the unique optical properties of the tissue. From the distinctive shape of this collected spectrum, information about the tissue composition can be extracted [36-40].

DRS offers simple instrumentation and can be integrated into surgical devices for real-time tissue sensing during pedicle screw placement thanks to fiber-optic technology. Swamy et al. [41] initiated the integration of DRS into surgical instruments for safe pedicle screw placement. Their study, supported by Monte Carlo (MC) simulations and experimental insertions of an optical screw probe, demonstrated the ability to distinguish cancellous and cortical bone through DRS based on fat, water, and blood content to improve pedicle screw accuracy. A subsequent study by Burström et al. [9] included DRS at the tip of an integrated pedicle screw and screwdriver, proposing a support vector machine (SVM) classifier that reliably detected transitions from cancellous to cortical bone, achieving a sensitivity of 98.3% and specificity of 97.7%. They concluded that DRS can

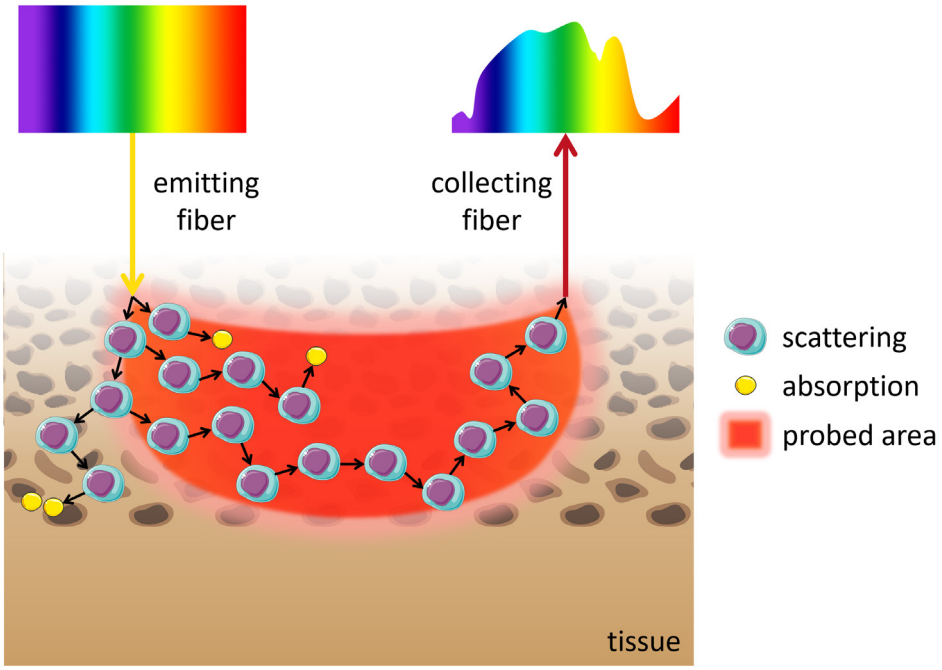

FIGURE 1.6: Illustration of Diffuse Reflectance Spectroscopy.

serve as a warning system for enhancing safety in spinal fusion surgery. In a subsequent *in-vivo* study [42], the application of DRS at the tip of a Jamshidi needle with an integrated optical K-wire was explored for breach detection. The findings underscore the robustness of DRS in quantifying fat fraction, ensuring reliability even under varying tissue perfusion and probe-handling conditions.

DRS thus holds promise for providing tissue feedback during pedicle screw placement. Particularly in scenarios where blood interference might impact conductivity measurements with the PediGuard, DRS remains unaffected when using near-infrared (NIR) wavelengths. Moreover, DRS enables sensing beyond the instrument's tip, allowing early warnings of impending cortical breaches. This 'look-ahead' distance also facilitates directional feedback, enabling surgeons to adjust the trajectory in real time during pedicle screw placement. These considerations highlight the potential of DRS for spine surgical guidance.

AIM AND OUTLINE OF THIS THESIS

To accommodate for the need for breach detection during pedicle screw placement, the aim of this PhD research is to investigate the potential of DRS for directional tissue feedback in spine surgery, and to overcome practical challenges encountered during the integration of DRS into surgical instruments and workflows.

Chapter 2 explores the composition of bone tissues in the spine. Through this investigation, we demonstrate how DRS can be used to distinguish between cancellous and cortical bone based on their different fat fractions.

Next, we explore how DRS can provide directional tissue feedback. Chapter 3 reviews how the propagation direction of light beams is controlled in fiber-optic medical devices. Chapter 4 provides insights into the impact of angulated fibers on the volume probed with DRS. Chapter 5 introduces a fiber-optic forward- and sideways-looking probe for the detection of perpendicular and acute breaches in spine surgery that establishes DRS as a compelling alternative to current surgical guidance systems.

Then, we focus on the practical implementation of DRS to transition from laboratory settings to real-world application in the operating room. Chapter 6 highlights how DRS can be integrated into fiber-optic pedicle probes to retrofit an existing surgical instrument with optical sensing for easy integration into the surgical workflow. Chapter 7 addresses the challenge of simplifying DRS from a complex setup to a compact system integrated into a handheld fiber-optic probe, ultimately aiming to create the abovementioned simple, less resource-intensive breach detection device.

Finally, Chapter 8 discusses the main findings presented in this thesis and puts them into perspective. This includes integrating findings from all chapters to develop the ideal DRS probe, addressing next steps for clinical validation, regulatory compliance, and commercialization strategies, as well as exploring potential applications beyond the scope of spine surgery.

REFERENCES

1. Lee, Ronald. "The demographic transition: three centuries of fundamental change."Journal of economic perspectives 17.4 (2002): 167-190.

2. Beschloss, Alexander, et al. "Marked increase in spinal deformity surgery throughout the United States." Spine 46.20 (2021): 1402-1408.

3. Zhang, Zhi-Qiang. Animal biodiversity: An outline of higher-level classification and survey of taxonomic richness. Magnolia press, 2011.

4. Gomez, Céline, et al. "Control of segment number in vertebrate embryos." Nature 454.7202 (2008): 335-339.

5. Ota, Kinya G., et al. "Identification of vertebra-like elements and their possible differentiation from sclerotomes in the hagfish." Nature communications 2.1 (2011): 373.

6. Ritzel, Holger, et al. "The thickness of human vertebral cortical bone and its changes in aging and osteoporosis: A histomorphometric analysis of the complete spinal column from thirty-seven autopsy specimens." Journal of Bone and Mineral Research 12.1 (1997): 89-95.

7. Bittencourt, Amandha L., et al. "Cortical bone density by quantitative computed tomography mirrors disorders of bone structure in bone biopsy of non-dialysis CKD patients." Bone Reports 16 (2022): 101166.

8. Currey, John D. "Chapter A1 Cortical Bone." Handbook of biomaterial properties (2016): 3-13.

9. Burström, Gustav, et al. "Diffuse reflectance spectroscopy accurately identifies the pre-cortical zone to avoid impending pedicle screw breach in spinal fixation surgery." Biomedical optics express 10.11 (2019): 5905-5920.

10. Hernandez, Christopher J. "Chapter A2 cancellous bone." Handbook of biomaterial properties (2016): 15-21.

11. Zebaze, Roger, et al. "A new method of segmentation of compact-appearing, transitional and trabecular compartments and quantification of cortical porosity from high resolution peripheral quantitative computed tomographic images." Bone 54.1 (2013): 8-20.

12. Weinstein, Stuart L., et al. "Adolescent idiopathic scoliosis." The lancet 371.9623 (2008): 1527-1537.

13. Deyo, Richard A., et al. "United States trends in lumbar fusion surgery for degenerative conditions." Spine 30.12 (2005): 1441-1445.

14. Deyo, Richard A., and Sohail K. Mirza. "Trends and variations in the use of spine surgery." Clinical Orthopaedics and Related Research (1976-2007) 443 (2006): 139-146.

15. Dick, Walter, et al. "A new device for internal fixation of thoracolumbar and lumbar spine fractures: the 'fixateur interne'." Spinal Cord 23.4 (1985): 225-232.

16. Boucher, Harold H. "A method of spinal fusion." The Journal of Bone & Joint Surgery British Volume 41.2 (1959): 248-259.

17. Gaines Jr, Robert W. "The use of pedicle-screw internal fixation for the operative treatment of spinal disorders." JBJS 82.10 (2000): 1458.

18. Gelalis, Ioannis D., et al. "Accuracy of pedicle screw placement: a systematic review of prospective in vivo studies comparing free hand, fluoroscopy guidance and navigation techniques." European spine journal 21 (2012): 247-255.

19. Joseph, Jacob R., et al. "Current applications of robotics in spine surgery: a systematic review of the literature." Neurosurgical focus 42.5 (2017): E2.

20. Inamasu, Joji, and Bernard H. Guiot. "Vascular injury and complication in neurosurgical spine surgery." Acta neurochirurgica 148 (2006): 375-387.

21. Gautschi, Oliver P., et al. "Clinically relevant complications related to pedicle screw placement in thoracolumbar surgery and their management: a literature review of 35,630 pedicle screws." Neurosurgical focus 31.4 (2011): E8.

22. Kim, Yongjung J., et al. "Free hand pedicle screw placement in the thoracic spine: is it safe?." Spine 29.3 (2004): 333-342.

23. Manbachi, Amir, et al. "Guided pedicle screw insertion: techniques and training." The Spine Journal 14.1 (2014): 165-179.

24. Bourgeois, Austin C., et al. "The evolution of image-guided lumbosacral spine surgery." Annals of Translational Medicine 3.5 (2015).

25. Staartjes, Victor E., et al. "Pedicle screw revision in robot-guided, navigated, and freehand thoracolumbar instrumentation: a systematic review and meta-analysis." World neurosurgery 116 (2018): 433-443.

26. Kosmopoulos, Victor, and Constantin Schizas. "Pedicle screw placement accuracy: a meta-analysis." Spine 32.3 (2007): E111-E120.

27. Mason, Alexander, et al. "The accuracy of pedicle screw placement using intraoperative image guidance systems: a systematic review." Journal of Neurosurgery: Spine 20.2 (2014): 196-203.

28. Perdomo-Pantoja, Alexander, et al. "Accuracy of current techniques for placement of pedicle screws in the spine: a comprehensive systematic review and meta-analysis of 51,161 screws." World neurosurgery 126 (2019): 664-678.

29. Härtl, Roger, et al. "Worldwide survey on the use of navigation in spine surgery." World neurosurgery 79.1 (2013): 162-172.

30. Liu, Hao, et al. "Comparison of the accuracy between robot-assisted and conventional freehand pedicle screw placement: a systematic review and meta-analysis." International journal of computer assisted radiology and surgery 11 (2016): 2273-2281.

31. Ghasem, Alexander, et al. "The arrival of robotics in spine surgery: a review of the literature." Spine 43.23 (2018): 1670-1677.

32. Bolger, Ciaran, et al. "Electrical conductivity measurement: a new technique to detect iatrogenic initial pedicle perforation." European Spine Journal 16 (2007): 1919-1924.

33. Dixon, Daniel, et al. "Accuracy of a dynamic surgical guidance probe for screw insertion in the cervical spine: a cadaveric study." European Spine Journal 26 (2017): 1149-1153.

34. Chaput, Christopher D., et al. "Reduction in radiation (fluoroscopy) while maintaining safe placement of pedicle screws during lumbar spine fusion." (2012): E1305-E1309.

35. Guillen, Phillip T., et al. "Independent assessment of a new pedicle probe and its ability to detect pedicle breach: a cadaveric study." Journal of Neurosurgery: Spine 21.5 (2014): 821-825.

36. Farrell, Thomas J., et al. "A diffusion theory model of spatially resolved, steady-state diffuse reflectance for the noninvasive determination of tissue optical properties in vivo." Medical physics 19.4 (1992): 879-888.

37. Doornbos, Richard M. P., et al. "The determination of in vivo human tissue optical properties and absolute chromophore concentrations using spatially resolved steady-state diffuse reflectance spectroscopy." Physics in Medicine & Biology 44.4 (1999): 967.

38. van Veen, Robert L. P., et al. "Determination of visible near-IR absorption coefficients of mammalian fat using time-and spatially resolved diffuse reflectance and transmission spectroscopy." Journal of biomedical optics 10.5 (2005): 054004-054004.

39. Nachabé, Rami, et al. “Estimation of lipid and water concentrations in scattering media with diffuse optical spectroscopy from 900 to 1600 nm.” Journal of biomedical optics 15.3 (2010): 037015-037015.

40. Baltussen, Elisabeth J. M., et al. “Tissue diagnosis during colorectal cancer surgery using optical sensing: an in vivo study.” Journal of translational medicine 17 (2019): 1-10.

41. Swamy, Akash, et al. “Diffuse reflectance spectroscopy, a potential optical sensing technology for the detection of cortical breaches during spinal screw placement.” Journal of biomedical optics 24.1 (2019): 017002-017002.

42. Swamy, Akash, et al. “Diffuse reflectance spectroscopy for breach detection during pedicle screw placement: a first in vivo investigation in a porcine model.” BioMedical Engineering OnLine 19 (2020): 1-12.

2

Chapter 2

Fat fraction of the spine explored in an MRI cadaver study

published as
Losch, M. S., Swamy, A., Elmi-Terander, A., Edström, E., Hendriks, B. H., & Dankelman, J. (2021). Proton density fat fraction of the spinal column: an MRI cadaver study. *BioMedical Engineering OnLine*, 20(1), 1-11.

data available at
doi.org/10.4121/13089956.

ABSTRACT

The increased popularity of minimally invasive spinal surgery calls for a revision of guidance techniques to prevent injuries of nearby neural and vascular structures. Lipid content has previously been proposed as a distinguishing criterion for different bone tissues to provide guidance along the interface of cancellous and cortical bone. This study aims to investigate how fat is distributed throughout the spinal column to confirm or refute the suitability of lipid content for guidance purposes.

Proton density fat fraction (PDFF) was assessed over all vertebral levels for six human cadavers between 53 and 92 years of age, based on fat and water MR images. According to their distance to the vertebra contour, the data points were grouped in five regions of interest (ROIs): cortical bone (–1 mm to 0 mm), pre-cortical zone (PCZ) 1–3 (0–1 mm; 1–2 mm; 2–3 mm), and cancellous bone (≥ 3 mm). For PCZ1 vs. PCZ2, a significant difference in mean PDFF of between –7.59 pp and –4.39 pp on aver- age was found. For cortical bone vs. PCZ1, a significant difference in mean PDFF of between –27.09 pp and –18.96 pp on average was found.

A relationship between distance from the cortical bone boundary and lipid content could be established, paving the way for guidance techniques based on fat fraction detection for spinal surgery.

BACKGROUND

Spinal fusion surgery is performed to treat fractures, reduce back pain or correct for spinal deformities due to scoliosis or degenerative spine conditions [1-3]. The vertebrae are typically fixed to each other with the use of metal rods anchored to the bone through pedicle screws. Pedicle screws run through the pedicle while their heads provide dedicated attachment points for the rods. However, the relatively soft tissue on the inside of the bone, the cancellous bone, is not strong enough for spine fixation. Therefore, pedicle screw fixation mainly relies on locations where the screw is in direct contact with the surrounding bone layer, the dense cortical bone [4]. Increasing the contact area between screws and cortical bone is thought to result in better fixation of the pedicle screws [5-7].

Spinal fusion is commonly carried out in a minimally invasive surgery (MIS) procedure as this shortens length of hospital stay and recovery [8, 9]. MIS is performed through several small incisions, which necessitates guidance techniques for the surgeon to compensate for the limited visibility of the surgical site. The close proximity of neural and vascular structures and the inability to adjust the trajectory of the pedicle screw after insertion present an additional challenge to screw placement [10, 11].

One possible approach to maximize the contact area between screws and cortical bone is to replace the conventionally used straight screws with a flexible anchoring device that runs along the interface of cancellous and cortical bone on a curved trajectory close to the outer edge of the vertebra. The need for reliable guidance is evident for such a device. Hence, it is crucial to determine reliable distinguishing criteria for cancellous and cortical bone that help to identify the correct trajectory. Burström et al. [12] have suggested lipid content as such a criterion and shown its potential to predict impending breaches in pedicle screw placement.

Lipids in the human body are commonly quantified using MRI. Several research groups have used this medical imaging technique to non-invasively measure fat fraction in the vertebral body to evaluate various clinical conditions such as osteoporosis [13, 14], cancer [15], and metabolic disorders such as obesity and diabetes [16, 17]. However, few studies

focusing on the distribution of fat fraction within the vertebrae for distinction of cancellous and cortical bone are available so far [18].

This study, therefore, aims to investigate the fat fraction distribution throughout the spinal column of human cadavers and to identify a possible relationship between the distance from the cortical bone boundary and lipid content. The transition area between cancellous and cortical bone is of particular interest, given that a flexible anchoring device would be located in this area.

METHODS

In this research, six human cadavers (four females, two males) with an age range of 53–92 years (mean = 77.8 years) were studied. One of the subjects examined (Cadaver 5) was known to have suffered from malignant neoplasm of the esophagus. All cadavers were donated for scientific research. Informed consent had been signed before death by the donors or after death by relatives, according to local guidelines and U.S. regulations. The study was conducted in compliance with ethical guidelines for human cadaver studies.

IMAGE ACQUISITION

MRI

The cadavers' entire spines were scanned on a 1.5 Tesla (T) whole-body scanner (Ingenia, Philips Healthcare, Best, The Netherlands) in the prone position. The temperature of the cadavers was maintained at room temperature prior to scanning.

A three-dimensional (3D) six-echo spoiled gradient-echo sequence was used for chemical shift-encoding-based water–fat separation. The typical imaging parameters used in this study were: AP field of view = 220–310 mm; FH field of view = 240–350 mm; slice thickness = 3 mm; in-plane resolution = 1.2 x 1.2 mm^2; flip angle = 5°; TR = 9.9–15.87 ms; TE1 = 1.41–1.43 ms; ΔTE = 1.2 ms. Reconstruction with a voxel size of (0.45-0.67) x (0.45-0.67) x 1.5 mm^3 yielded 45–65 sagittal slices per sequence.

To obtain whole spine coverage, the MR exam consisted of three 3D spoiled gradient-echo sequences placed on the cervical, thoracic and

lumbar spine, respectively. Total scan time per cadaver was approximately 5–10 min.

DETERMINATION OF PDFF

The scanner image reconstruction was used to separate the signals of water and fat using Philips DICOM viewer R3.0-SP04 (Philips Healthcare, Best, The Netherlands). The water–fat separation was based on a seven-peak water–fat spectral model [19].

Based on fat signal (F) and water signal (W), proton density fat fraction (PDFF) was calculated as:

$$PDFF[\%] = \frac{F}{F+W} \cdot 100\,.$$

Figure 2.1 shows the visual representation of a PDFF MR image of the mid-sagittal slice of the whole spine.

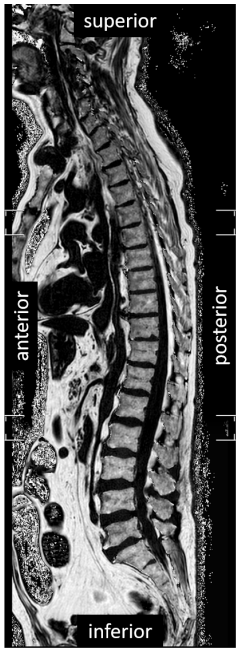

FIGURE 2.1: Mid-sagittal PDFF MR image of the whole spine (Cadaver 6).

IMAGE ANALYSIS

For each cadaver, the three mid-sagittal slices (cervical, thoracic, lumbar) plus three respective adjacent slices on each side were retained for the analysis. The image analysis procedure was performed for vertebrae C3 through L5.

ROI SELECTION

For each slice, regions of interest (ROIs) were selected on the MR image using the FIJI distribution of ImageJ [20]. The contours of the single vertebrae were found based on grayscale value of the PDFF MR image and estimated vertebra shape, as shown in Figure 2.2a. Anterior, inferior and superior walls were included in the analysis.

Burström et al.[12] have introduced the concept of a 3-mm-thick transition zone between cancellous and cortical bone, the so-called pre-cortical zone (PCZ). This idea was adopted in this work: pixels within a 3-mm distance from the vertebra contour were assigned to one of three adjacent pre-cortical ROIs of 1 mm thickness each (PCZ1, PCZ2, PCZ3). An ROI within the vertebra at a distance of more than 3 mm to the contour was considered to contain the cancellous bone. An ROI of cortical bone was defined as the first mm (−1 mm to 0 mm) outside the detected contour. The selected ROIs are shown in Figure 2.2b. An overview of the ROIs can be found in Table 2.1.

DATA EXTRACTION

Fat fraction distributions were calculated for the ROIs listed in Table 2.1 by calculating the PDFFs for all pixels included in the respective ROI using MATLAB R2019b (The MathWorks Inc., Natick (MA), USA). For each vertebra within each cadaver, the data points gathered from the different slices were merged to yield one dataset per ROI.

STATISTICAL ANALYSIS

To provide guidance in the context of spinal fusion surgery, individual variation in fat fraction is considered most important, so the data were analyzed separately for every vertebra in each of the cadavers.

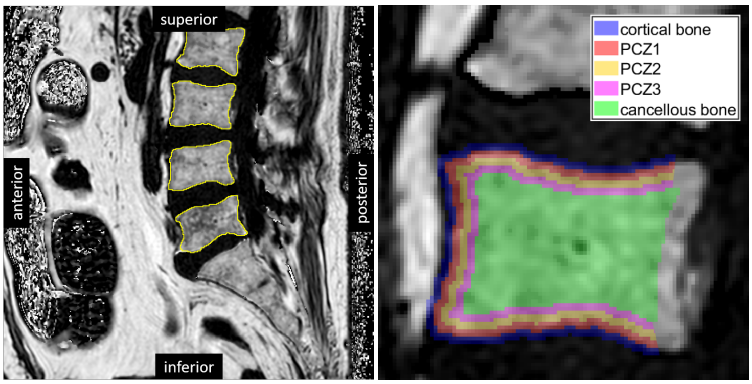

(a) (b)

FIGURE 2.2: ROI selection process: a Mid-sagittal PDFF MR image of the lumbar spine with detected vertebra contours. b Definition of the anatomical ROIs: cortical bone, pre-cortical zone (PCZ), and cancellous bone.

TABLE 2.1: Overview of the defined ROIs.

	Bone type	Distance from contour
ROI0	Cortical bone	−1 mm to 0 mm
ROI1	PCZ1	0 mm to 1 mm
ROI2	PCZ2	1 mm to 2 mm
ROI3	PCZ3	2 mm to 3 mm
ROI4	Cancellous bone	≥ 3 mm

Mean differences of the measured PDFFs were computed for the respective adjacent ROIs (cortical bone vs. PCZ1; PCZ1 vs. PCZ2; PCZ2 vs. PCZ3; PCZ3 vs. cancellous bone) as the difference of the outer ROI's mean PDFF value to the inner ROI's mean PDFF value. As reliable guidance is crucial for spinal surgery, a pair of adjacent ROIs was only considered significantly different if, after the exclusion of potential outliers, the mean differences observed for this pair consistently had the same sign for *all* vertebrae.

RESULTS

EXTRACTED PDFF DATA

For the cortical bone and the three PCZs, between 300 and 3 500 individual PDFF values per vertebra and cadaver were extracted, respectively, depending on the vertebra size. The ROI of cancellous bone contained up to 20 000 data points for the largest vertebrae.

Figure 2.3 displays the PDFF distributions obtained for the individual ROIs over all vertebral levels. The mean PDFF is displayed as a solid line. To each side, one standard deviation is highlighted in the corresponding color. The mean PDFFs and standard deviations over the whole spine are displayed to the right of each plot for the ROIs of the corresponding cadaver.

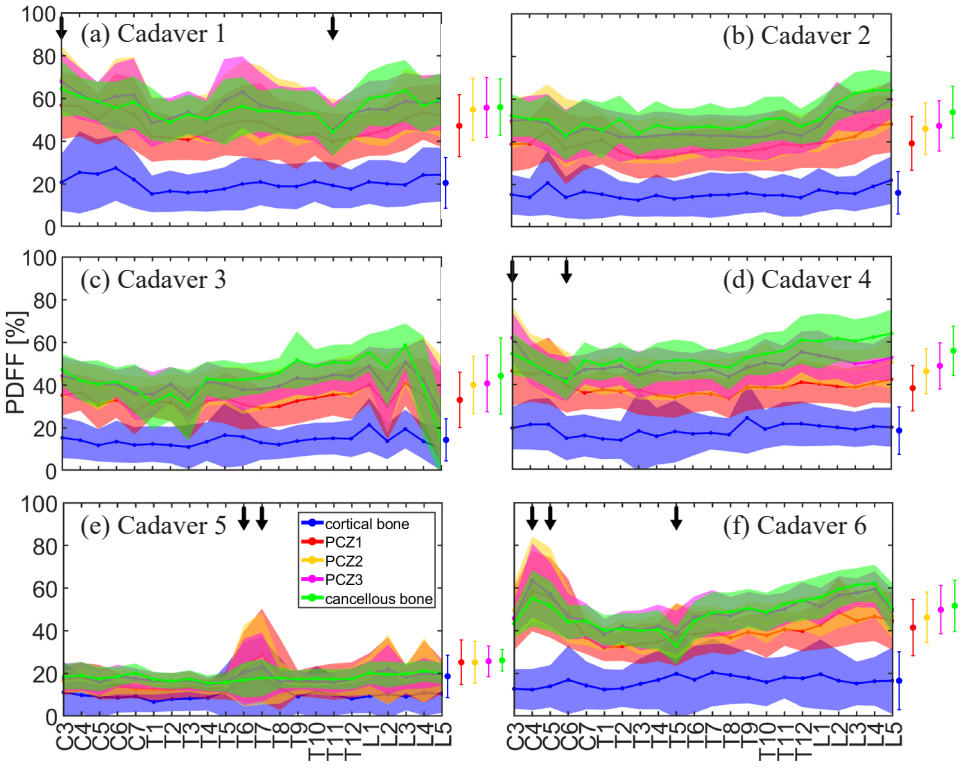

FIGURE 2.3: PDFF distributions over all vertebral levels and whole spine mean PDFFs and standard deviations.

Figure 2.3 shows similar PDFF distributions for all cadavers, with the exception of Cadaver 5, which shows very low overall PDFF in comparison to the other cadavers.

The PDFF distributions show that natural variation among the individual vertebrae exists. This variation becomes especially apparent in Cadaver 3 (Figure 2.3c). For the other cadavers, however, large deviations from the whole spine mean PDFF are rare and only occur for singular vertebrae (marked in Figure 2.3 with downward pointing arrows).

All cadavers but Cadaver 5 exhibit a mean cortical bone PDFF of around 15–20%. The curve of the cortical bone PDFF distribution is distinct from the distribution curves of the other ROIs. Mean PCZ1 PDFF lies between 30 and 50%. For each of the cadavers, the PCZ1 PDFF distribution curve is partly below the distribution curves of the remaining ROIs. PCZ2, PCZ3, and cancellous bone exhibit elevated mean PDFF values, and their PDFF distribution curves overlap to a large extent.

In Cadaver 5, the mean cortical bone PDFF is around 10%. The PDFF distribution curves for PCZ1, PCZ2, PCZ3 and cancellous bone overlap and exhibit mean values below 20%.

RESULTS OF THE STATISTICAL ANALYSIS

The box plots in Figure 2.4 display the distribution of the mean differences in the PDFF for adjacent ROIs observed for the individual vertebrae of each cadaver. The plots show that mean differences behave similarly in all cadavers, with the exception of Cadaver 5.

All cadavers but Cadaver 5 exhibit mean PDFF differences for PCZ3 vs. cancellous bone and for PCZ2 vs. PCZ3 whose plots are around or contain the value zero. The plots for PCZ1 vs. PCZ2 are below zero and display median values between −7.59 percentage points (pp) (Cadaver 1) and −4.39 pp (Cadaver 6). The plots for cortical bone vs. PCZ1 are also below zero and display median values between −27.09 pp (Cadaver 1) and −18.96 pp (Cadaver 3).

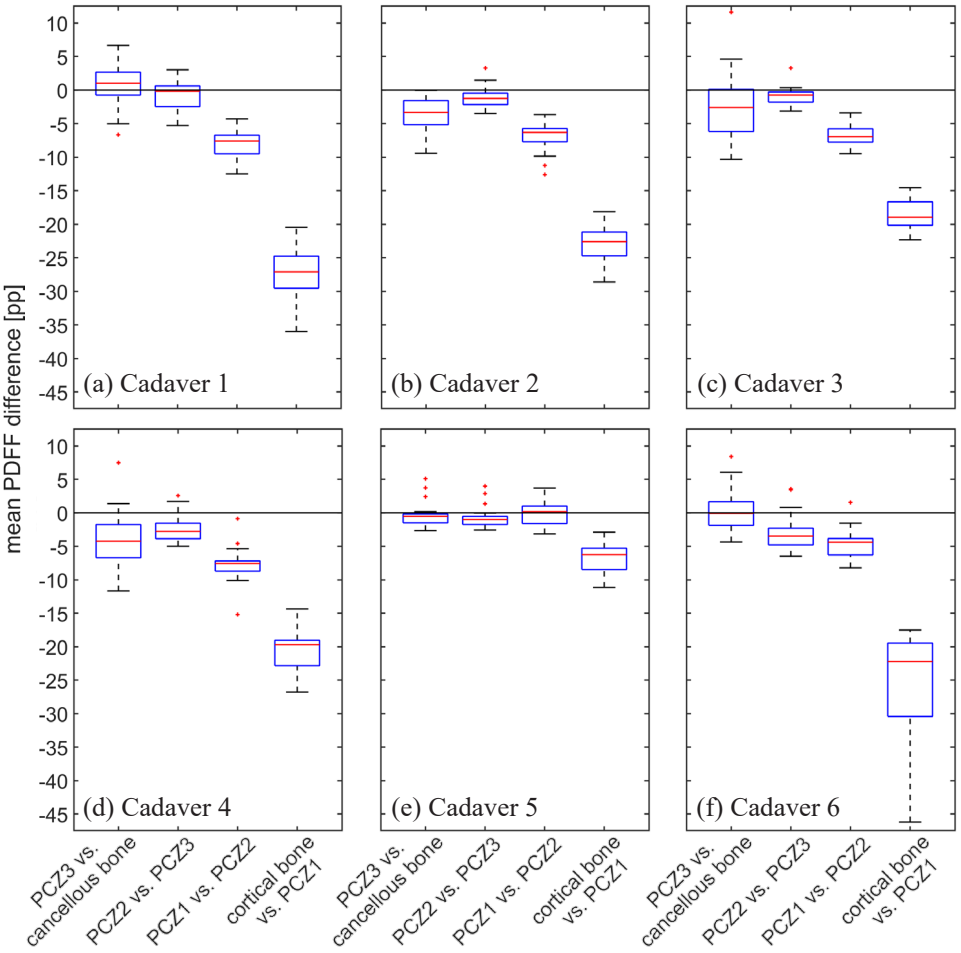

FIGURE 2.4: Mean PDFF differences for all vertebrae.

When used for guidance in spinal fusion surgery, fat fraction detection should enable the surgeon to detect the bone boundary and prevent breaching it. Assuming the surgeon to approach the outer layer (PCZ and cortical bone) from the inside of the bone, the first observed mean difference is at the interface of cancellous bone and PCZ3. After excluding the outliers, this difference is between −11.64 pp (Cadaver 4) and +6.66 pp (Cadaver 1) for the examined samples. For the transition from PCZ3 towards PCZ2, the mean PDFF difference varies from −6.48 pp (Cadaver 6) to +3.02 pp (Cadaver 1).

A difference in the mean PDFF of between −12.48 pp (Cadaver 1) and −1.53 pp (Cadaver 6) is found from PCZ2 towards PCZ1. The mean PDFF in the cortical bone changes by between −46.19 pp (Cadaver 6) and −14.34 pp (Cadaver 4) as compared to PCZ1.

For Cadaver 5, the plots of the mean PDFF differences for PCZ3 vs. cancellous bone, for PCZ2 vs. PCZ3 and for PCZ1 vs. PCZ2 all contain the value zero. The plot for cortical bone vs. PCZ1 is below zero and displays a median value of −6.25 pp.

DISCUSSION

In this study, we have investigated the distribution of PDFF in human cadaver vertebrae, with a particular focus on the transition zone between the cancellous and cortical regions of the bone (PCZ). As a flexible anchoring device would be affixed in the PCZ along the outer edge of the vertebra, the area around the spinal cord was considered irrelevant for the given application and was thus not part of the analysis.

The cadavers included in this study had a mean age of 77.8 years and belonged to the patient cohort of older adults, which is the most common cohort for spinal fusion surgery. Patients in this cohort may suffer from back pain due to various clinical conditions including degenerative disk disease and spinal stenosis [2]. Measurements of PDFF in the cancellous bone from this *ex-vivo* study are in line with the results of previous *in-vivo* research on similar patient cohorts [13, 21, 22].

Similar PDFF distributions and mean PDFFs were observed for all cadavers, except for Cadaver 5. The study results show lower PDFF for Cadaver 5 compared to the rest of the cadavers studied. This subject was found to suffer from malignant neoplasm of the esophagus, which may be the cause of the low PDFF found across all spinal levels. Patients with active malignancy have a higher chance of perioperative complications and are less likely to be considered for spinal fusion surgery [23, 24]. The PDFF measurements for Cadaver 5 can therefore be assumed to be non-representative of vertebral body fat fraction in spinal surgery patients. The mean PDFF difference between cortical bone and PCZ1 found for this cadaver suggests that guidance based on fat fraction may still be

possible for patients with active malignancies, but parameters would have to be assessed separately for these patients.

For the other cadavers, the observed PDFF distributions suggest that cortical bone can be distinguished from the remaining ROIs. Fat fraction seems to increase gradually from cortical bone through PCZ1 up to the three innermost ROIs (PCZ2, PCZ3, and cancellous bone). As the PDFF distributions of these three ROIs overlap, no distinction based on PDFF measurements seems possible here.

Statistical analysis confirms these findings: when examining the mean PDFF difference of PCZ3 vs. cancellous bone, no significance is found, as both positive and negative values are observed. Equally, for the mean PDFF difference of PCZ2 vs. PCZ3, the observed values do not consistently have the same sign, hence these zones are not considered significantly different.

When advancing from PCZ2 towards PCZ1, a first significant drop in the mean PDFF can be observed. For the examined samples, the average difference was between −7.59 pp (Figure 2.4a) and −4.39 pp (Figure 2.4f). Although consistently negative, the absolute values of the observed differences are small for some vertebrae, and it needs to be verified whether they can reliably serve for guidance in spinal fusion surgery.

When further advancing from PCZ1 towards cortical bone, another significant decrease in the mean PDFF is found. For the examined samples, the average difference was between −27.09 pp (Figure 2.4a) and −18.96 pp (Figure 2.4c). This decrease is in the same order of magnitude as the total mean cortical bone PDFF, and can, therefore, very likely be detected intra-operatively, and thus prevent the surgeon from traversing the cortical bone boundary.

For singular vertebrae, the PDFF curves reveal unusually large deviations from the whole spine mean. These vertebrae also show an altered anatomy on the PDFF MR images. Modic changes that come along with degenerative edema can lead to elevated grayscale values, which are associated with a high PDFF [25]. Another cause for large deviations

from the whole spine mean are sclerotic lesions, which can, for instance, manifest as bone islands – intramedullary condensations of cortical bone which appear as areas with low signal intensity.

In Cadaver 3, which reveals a particularly high variation in PDFF (Figure 2.3c), several vertebrae exhibit dark spots. Possible explanations are an underlying malignancy with metastases that have destroyed the bone partially, or posterior vertebral scalloping that is a possible result of a variety of pathologies such as degenerative spine conditions, dural ectasia, and intraspinal tumors deforming the vertebra [26]. The influence of such anomalies on lipid content in the vertebrae needs to be researched, although the mean differences acquired in this study do not reveal substantial discrepancies for vertebrae with an altered anatomy.

Furthermore, it has been shown previously that the PDFF changes over the course of a lifetime [27]. This study focused on the most common patient cohort of older adults, and none of the examined cadavers belonged to the other patient cohort of adolescents suffering from spinal deformities [1]. A further study investigating fat fraction distribution in the vertebrae of this patient cohort is encouraged.

It could be argued that the vertebral fat content of cadavers may not represent the *in-vivo* fat content due to postmortem changes. However, a study by Lamoureux et al. [28] showed that bovine and equine percentage of fat in bone marrow does not change within 30–60 days after necropsy, regardless of the storage condition. In an *in-vivo* human study by de Boer et al. [29] fat content was assessed on tissue samples both before and after resection. Comparison of the measurements did not yield any significant differences.

LIMITATIONS

The model used for water–fat separation assumes that objects are scanned at body temperature. Although this model is relatively stable to variations in temperature, the calculated PDFF values might be slightly biased, as the cadavers examined in this study were not scanned at body temperature but at room temperature.

Selection of the vertebra contours was done by manually detecting high grayscale values on the MR image. Although the process was kept consistent for the entire dataset, it is prone to bias. Using CT images as ground truth for vertebra contour detection is recommended for future studies. Another possible approach to mitigate the bias is to increase the magnetic field strength from 1.5 T to 3 T for better separation of fat and water, thereby creating a higher contrast between cortical and cancellous bone on the MR images [30]. Image acquisition with an increased in-plane resolution could decrease the pixel size and thus increase the number of data points for each ROI.

The cortical bone ROI was grown automatically based on the detected vertebra contour and the assumption of a uniform cortical thickness of 1 mm. Swamy et al.[31] have shown cortical bone thickness to vary between 1 and 3 mm. However, cortical bone at a distance of more than −1 mm from the vertebra contour is expected to show an equal or lower PDFF compared to the cortical bone ROI as defined in this study, creating an even larger mean difference between cortical bone and PCZ1.

Lastly, investigating PDFF distributions across additional slices and other 3D planes could provide further insights, especially concerning the PDFF distribution in the pedicle area, a crucial region for screw placement.

CONCLUSION

This study investigated the fat fraction distribution, quantified through MRI, throughout the spinal column of six human cadavers. Lipid content was found to be related to the distance from the cortical bone boundary, and significant mean PDFF differences between cortical bone and the PCZ were found. Hence, in this study, fat fraction is found to be a valid criterion for distinction between the different bone tissues in vertebrae and has the potential to provide guidance in spinal fusion surgery.

REFERENCES

1. Weinstein, Stuart L., et al. "Adolescent idiopathic scoliosis." The lancet 371.9623 (2008): 1527-1537.

2. Deyo, Richard A., et al. "United States trends in lumbar fusion surgery for degenerative conditions." Spine 30.12 (2005): 1441-1445.

3. Dick, Walter, et al. "A new device for internal fixation of thoracolumbar and lumbar spine fractures: the 'fixateur interne'." Spinal Cord 23.4 (1985): 225-232.

4. Eswaran, Senthil K., et al. "Cortical and trabecular load sharing in the human vertebral body." Journal of Bone and Mineral Research 21.2 (2006): 307-314.

5. Luther, Neal, et al. "Comparison of navigated versus non-navigated pedicle screw placement in 260 patients and 1434 screws: screw accuracy, screw size, and the complexity of surgery." Clinical Spine Surgery 28.5 (2015): E298-E303.

6. Rajasekaran, Shanmuganathan, et al. "Accuracy of pedicle screw insertion by AIRO® intraoperative CT in complex spinal deformity assessed by a new classification based on technical complexity of screw insertion." European Spine Journal 27 (2018): 2339-2347.

7. Solitro, Giovanni F., et al. "Currently adopted criteria for pedicle screw diameter selection." International journal of spine surgery 13.2 (2019): 132-145.

8. Oppenheimer, Jeffrey H., et al. "Minimally invasive spine technology and minimally invasive spine surgery: a historical review." Neurosurgical focus 27.3 (2009): E9.

9. Goldstein, Christina L., et al. "Perioperative outcomes and adverse events of minimally invasive versus open posterior lumbar fusion: meta-analysis and systematic review." Journal of Neurosurgery: Spine 24.3 (2016): 416-427.

10. Kosmopoulos, Victor, and Constantin Schizas. "Pedicle screw placement accuracy: a meta-analysis." Spine 32.3 (2007): E111-E120.

11. Staartjes, Victor E., et al. "Pedicle screw revision in robot-guided, navigated, and freehand thoracolumbar instrumentation: a systematic review and meta-analysis." World neurosurgery 116 (2018): 433-443.

12. Burström, Gustav, et al. "Diffuse reflectance spectroscopy accurately identifies the pre-cortical zone to avoid impending pedicle screw breach in spinal fixation surgery." Biomedical optics express 10.11 (2019): 5905-5920.

13. Yeung, David K. W., et al. "Osteoporosis is associated with increased marrow fat content and decreased marrow fat unsaturation: a proton MR spectroscopy study." Journal of Magnetic Resonance Imaging: An Official Journal of the International Society for Magnetic Resonance in Medicine 22.2 (2005): 279-285.

14. Li, Xiaojuan, et al. "Quantification of vertebral bone marrow fat content using 3 Tesla MR spectroscopy: reproducibility, vertebral variation, and applications in osteoporosis." Journal of Magnetic Resonance Imaging 33.4 (2011): 974-979.

15. Schraml, Christina, et al. "Multiparametric analysis of bone marrow in cancer patients using simultaneous PET/MR imaging: Correlation of fat fraction, diffusivity, metabolic activity, and anthropometric data." Journal of Magnetic Resonance Imaging 42.4 (2015): 1048-1056.

16. Bredella, Miriam A., et al. "Vertebral bone marrow fat is positively associated with visceral fat and inversely associated with IGF-1 in obese women." Obesity 19.1 (2011): 49-53.

17. Baum, Thomas, et al. "Does vertebral bone marrow fat content correlate with abdominal adipose tissue, lumbar spine bone mineral density, and blood biomarkers in women with type 2 diabetes mellitus?." Journal of Magnetic Resonance Imaging 35.1 (2012): 117-124.

18. Swamy, Akash, et al. "Validation of diffuse reflectance spectroscopy with magnetic resonance imaging for accurate vertebral bone fat fraction quantification." Biomedical optics express 10.8 (2019): 4316-4328.

19. Ren, Jimin, et al. "Composition of adipose tissue and marrow fat in humans by 1H NMR at 7 Tesla." Journal of lipid research 49.9 (2008): 2055-2062.

20. Schindelin, Johannes, et al. "Fiji: an open-source platform for biological-image analysis." Nature methods 9.7 (2012): 676-682.

21. Kühn, Jens-Peter, et al. "Proton-density fat fraction and simultaneous R2* estimation as an MRI tool for assessment of osteoporosis." European radiology 23 (2013): 3432-3439.

22. Schwartz, Ann V., et al. "Vertebral bone marrow fat associated with lower trabecular BMD and prevalent vertebral fracture in older adults." The Journal of Clinical Endocrinology & Metabolism 98.6 (2013): 2294-2300.

23. Copeland, Graham P., et al. "POSSUM: a scoring system for surgical audit." British Journal of Surgery 78.3 (1991): 355-360.

24. de Cássia Braga Ribeiro, Karina, and Luiz Paulo Kowalski. "APACHE II, POSSUM, and ASA scores and the risk of perioperative complications in patients with oral or oropharyngeal cancer." Archives of Otolaryngology–Head & Neck Surgery 129.7 (2003): 739-745.

25. Fields, Aaron J., et al. "Measuring and reporting of vertebral endplate bone marrow lesions as seen on MRI (Modic changes): recommendations from the ISSLS Degenerative Spinal Phenotypes Group." European Spine Journal 28 (2019): 2266-2274.

26. Wakely, Suzanne L. "The posterior vertebral scalloping sign." Radiology 239.2 (2006): 607-609.

27. Baum, Thomas, et al. "Anatomical variation of age-related changes in vertebral bone marrow composition using chemical shift encoding-based water–fat magnetic resonance imaging." Frontiers in Endocrinology 9 (2018): 141.

28. Lamoureux, Jennifer L., et al. "The effect of environmental storage conditions on bone marrow fat determination in three species." Journal of veterinary diagnostic investigation 23.2 (2011): 312-315.

29. de Boer, Lisanne L., et al. "Using DRS during breast conserving surgery: identifying robust optical parameters and influence of inter-patient variation." Biomedical optics express 7.12 (2016): 5188-5200.

30. Soher, Brian J., et al. "A review of MR physics: 3T versus 1.5T." Magnetic resonance imaging clinics of North America 15.3 (2007): 277-290.

31. Swamy, Akash, et al. "Diffuse reflectance spectroscopy, a potential optical sensing technology for the detection of cortical breaches during spinal screw placement." Journal of biomedical optics 24.1 (2019): 017002-017002.

3

Chapter 3

A patent review of light beam steering in fiber-optic medical devices

published as

Losch, M. S., Kardux, F., Dankelman, J., & Hendriks, B. H. (2022). Steering light in fiber-optic medical devices: a patent review. *Expert Review of Medical Devices*, *19*(3), 259-271.

ABSTRACT

Steering light is relevant to many medical applications that require tissue illumination, sensing, or modification. To control the propagation direction of light beams, a great variety of innovative fiber-optic medical devices have been designed.

This review provides a comprehensive overview of the patent literature on light beam control in fiber-optic medical devices. The Web of Science Derwent Innovation Index database was scanned, and 81 patents on fiber-optic devices published in the last 20 years (2001-2021) were retrieved and categorized based on the working principle to steer light (refraction/reflection, scattering, diffraction) and the design strategy that was employed (within fiber, at fiber end, outside fiber).

Patents describing medical devices were found for all categories, except for generating diffraction at the fiber end surface. The insight in the different designs reveals that there are still several opportunities to design innovative devices that can collect light at an angle off-axis, reduce the angular distribution of light, or split light into multiple beams.

INTRODUCTION

BACKGROUND

Optical fibers are commonly integrated into medical devices for remote light delivery and collection because of their high flexibility, low propagation loss, compatibility, and tolerance to electromagnetic interference [1]. The usefulness of fiber-optic devices has been shown for various medical applications, such as temperature, pressure and shape sensing [2-7], tissue illumination and modification [8-10], and spectral tissue sensing [8-10]. A conventional optical fiber is made up of a core that carries the light, a cladding, and a buffer coating. The refractive index of the cladding is slightly lower than the refractive index of the core. Because of this difference in refractive index, light incident on the core-cladding interface with an angle greater than a certain threshold, known as the critical angle, is reflected back into the core – a phenomenon known as total internal reflection. Thanks to total internal reflection, light can travel along the longitudinal axis of the optical fiber core to the distal end of a device.

When using fiber-optic medical devices for illumination, spectral tissue sensing, and cell modification, the light leaves the distal end of the device and interacts with the surrounding tissue. The optical characteristics and shape of the distal end determine how light is emitted to or collected from tissue [9, 11]. A conventional distal end design is a flat polished fiber tip [11]. As light leaves and enters the distal end of the device in axial direction, the utility of such a conventional fiber-optic device is limited.

Modified distal end designs for light beam control could have great potential to expand the range of possible applications, for example: emitting and collecting light at an angle off-axis allows for side-looking tissue spectroscopy, improved laser ablation and tissue welding; the angular distribution of light can be increased for uniform irradiation as required in photodynamic therapy or for photodisinfection or, on the contrary, decreased for beam focusing in laser surgery; finally, splitting light into multiple beams allows for multi-spot pattern generation as required in laser photocoagulation. For these applications, new fiber-optic

devices are needed that can control the propagation direction of light beams and steer them as desired to meet various challenges:

(1) emit light at an angle off-axis;

(2) collect incident light at an angle off-axis;

(3) increase the angular distribution of light;

(4) decrease the angular distribution of light;

(5) split light into multiple beams.

GOAL AND STRUCTURE

This review provides a comprehensive overview of the patent literature on light beam control in medical devices. It investigates how various distal end designs can steer light in the desired direction and identifies new design challenges in this field of research. All selected patents are categorized based on the underlying working principle to steer light and the employed design strategy to incorporate this principle into the distal end of a fiber-optic medical device to provide insights into future technological directions for the identification of new design challenges for steering light. Section 2 reports the method of the patent search and the search results. Section 3 explains the categorization of the fiber-optic devices. Section 4 treats the different distal end designs found for devices employing refraction and reflection. Section 5 treats the different distal end designs found for devices employing scattering. Section 6 treats the different distal end designs found for devices employing diffraction. The types of distal end designs and their effect on the light beam propagation direction are discussed in relation to the temporal distribution of the categorized patents in Section 7. Finally, Section 8 provides the conclusion, and Section 9 presents our expert commentary on this topic.

METHOD

PATENT SEARCH METHOD

A patent search was conducted on distal end designs of fiber-optic medical devices for remote light delivery and collection, using the Web of Science Derwent Innovation Index (DII) patent database. The search query

consisted of a logical conjunction (AND) of keywords in two categories: object (targeting devices including a light guide for remote light delivery and collection) and location (targeting patents describing specifically the distal end of fiber-optic devices). The patent search was not restricted to devices with one specific function; however, a combination of keywords within a third category, imaging applications (targeting imaging devices disposing of complex optical systems for light beam focusing), was added to the search query as a logical complement (NOT) to exclude patents irrelevant to this review. Moreover, the search query was limited within classification P3: *Health and amusement*, levels P31-P34. These levels of the DII classification system are comparable with classification A61: *Medical or veterinary science; hygiene* of the general cooperative patent classification (CPC). The search was restricted to patents linked to the World Intellectual Property Organization (WO*), the United States (US*), or Europe (EP*), published within the last 20 years. The entire search query was: *TI = ((light* OR laser* OR optic*) AND (fiber* OR *guide OR probe OR needle OR delivery)) AND TI = (end OR distal OR tip OR exit OR aperture) AND DC = (P31 OR P32 OR P33 OR P34) AND PN = (WO* OR US* OR EP*) NOT TI = (imag* OR tomograph* OR scan* OR camera OR microscop*) Timespan: 2001-2021.*

ELIGIBILITY CRITERIA

The search was restricted to devices for use inside the body with direct light-tissue interaction for illumination, spectral tissue sensing, or cell modification via laser surgery or light-induced therapy. The following eligibility criteria were applied:

- application domain: patent describes an optical fiber for remote light delivery or collection **in the human body**
- function: light **directly interacts with tissue** for illumination, spectral tissue sensing, or cell modification
- direction control: patent describes an optical feature at the distal end of the device that **steers light** in the desired direction
- language: patent is **available in English**

PATENT SEARCH RESULTS

The patent search query returned 1197 patents from the DII database (last update 1 December 2021). The titles, abstracts, and figures of these patents were manually checked based on the eligibility criteria. All criteria need to be fulfilled for the patent to be included in the review. This selection resulted in 166 patents being potentially useful. All search results from the DII database included a link to the Espacenet database, which allows for users to access the complete text. The full text of the 166 potentially valuable patents was further examined by reading the patents' claims and descriptions, and by in-depth analysis of the figures. After checking these patents, 15 duplicates were identified, and 84 patents were excluded. The final selection resulted in 67 relevant patents. For all relevant patents, the cited patents were scanned for new relevant information, resulting in 14 additional patents that met all of the criteria. Finally, 81 patents were included in this review, see Figure 3.1a.

CATEGORIZATION

There are four working principles for steering a light beam in the desired direction [12]:

(1) refraction;

(2) reflection;

(3) scattering;

(4) diffraction.

Refraction is defined as the change in direction of a transmitted light beam after it enters a second medium. Reflection is defined as the change in direction of a light beam at an interface that returns the light beam back to the original medium. The angle of incidence of the light beam on the surface and the material properties of the two media determine the intensity and direction of the refracted and reflected light beam. Another way to steer light is scattering: multiple changes in refractive index force the light beam to randomly change direction in a series of reflection events, resulting in diffuse light scattering. Lastly, a fundamentally different method to steer a light beam is diffraction. Diffraction is defined as the

bending of light after encountering a small opening or obstacle. The light beam does not bend in one direction; instead, a diffraction pattern is generated by the interference of different wave fronts. Diffraction is predominant for apertures and obstacles with sizes in the range of the wavelength of the incident light.

For refraction and reflection, an interface between two media is required; for scattering, a volume causing many reflection events is required; for diffraction, a small aperture or obstruction is required. Within a fiber-optic medical device, these design requirements can be met by changing the geometry or material of the optical fiber core and cladding, resulting in a change in the total internal reflection pattern within the fiber itself. Another option is changing the shape and material properties of the optical fiber core end surface. Finally, a regular optical fiber can be used with an extra optical element added outside the fiber. In summary, there are three design strategies for steering a light beam in the desired direction:

(1) modifying the total internal reflection pattern inside the optical fiber;

(2) modifying the optical fiber core end surface;

(3) adding an optical element outside the optical fiber.

Hence, all distal end designs of the fiber-optic medical devices included in this review are categorized based on the working principle to steer light (Level 1) and the design strategy that was employed (Level 2), see Figure 3.1b. Some patents describe various designs for achieving light beam steering using the same underlying working principle. Likewise, one device can include multiple optical features to steer the light in the desired direction using different underlying working principles. Therefore, a single patent can be assigned to multiple categories.

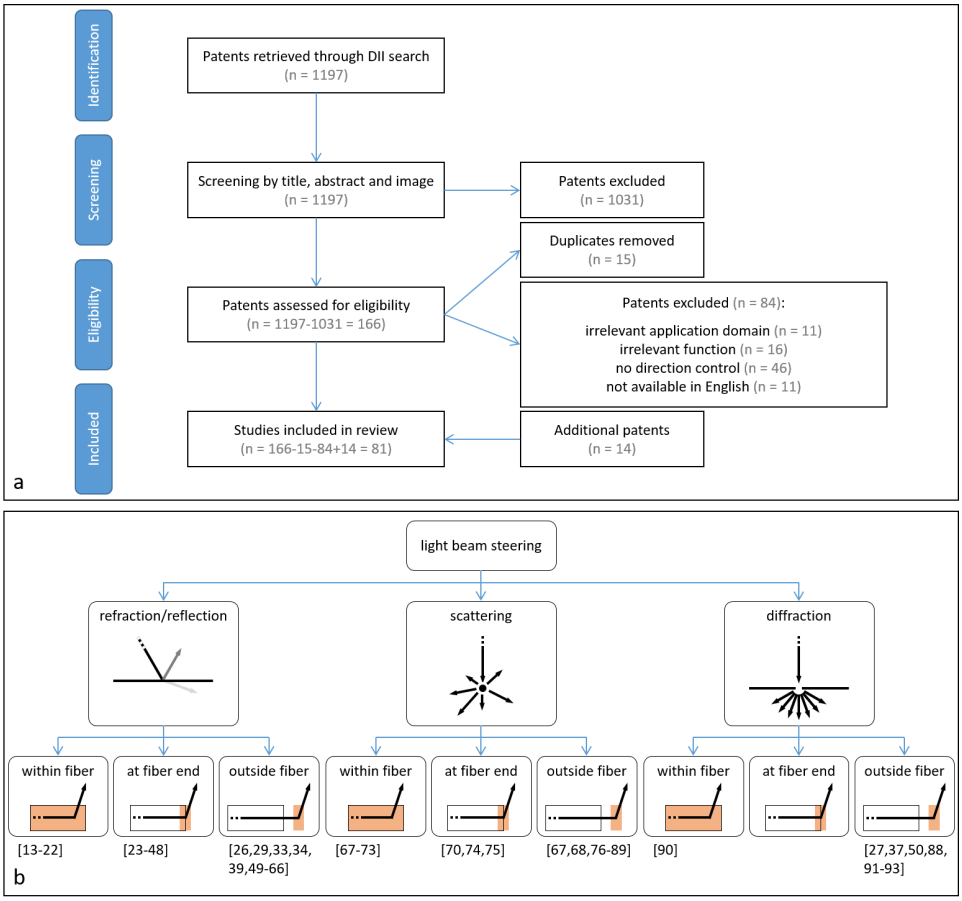

FIGURE 3.1: a Schematic representation of the patent selection method. b Distal end designs of fiber-optic medical devices that can steer light in the desired direction, categorized based on the working principle to steer light (Level 1) and the design strategy that was employed (Level 2). References are given in brackets.

REFRACTION AND REFLECTION

MODIFYING THE TOTAL INTERNAL REFLECTION PATTERN INSIDE THE OPTICAL FIBER

Ten patents describe devices with customized distal ends that use the existing interface between the core and the cladding within an optical fiber to steer light in the desired direction [13-22]. Usually, the longitudinal axis of an optical fiber within a medical device is parallel to the longitudinal axis of the device itself. However, fiber-optic medical devices can have one or more optical fibers with a bent distal section inserted into a curved path within the housing of the device [13-18]. The total internal reflection of light along the bent section enables light to leave or enter the optical fiber at an angle off the device's longitudinal axis. In other words, the bent segment generates a fiber terminating tip that faces the side. The most basic designs use one optical fiber, which is curved away from the central axis to emit light to the side, see Figure 3.2a [13-15]. Kern et al. [16] describe a unique design where the fiber is first curved away from the central axis and then curved towards it to achieve a larger curve radius. Two other patented devices include distal end designs with numerous bent optical fibers, one or more of which emit light and one or more of which collect light [17, 18].

It is also possible to twist several optical fibers around the central axis of the device [19, 20]. As described by Farley [19], several fibers can be twisted to form a helix, with the terminating tips of all optical fibers being angularly separated. This produces a multi-spot pattern of light on the target tissue. Cottrel and Foster [20] describe a device that can both emit and collect light from the side using twisted optical fibers. This device includes seven optical fibers in a six-around-one configuration. The six outside fibers are twisted into side-fire fibers and arranged along the device's longitudinal axis in a linear array. At least one of the optical fibers acts as a light source, while the other fibers collect the light after interaction with the tissue, see Figure 3.2b.

Instead of bending the optical fiber, it is also possible to remove the material of the cladding at the distal section of the fiber to generate a side-facing tip [21, 22]. The slot within the cladding generates an interface

where light does not reflect entirely, allowing it to exit the fiber in radial direction. Multiple slots in the optical fiber allow light to leave at multiple locations along the length of the fiber, see Figure 3.2c.

MODIFYING THE OPTICAL FIBER CORE END SURFACE

Twenty-six patents describe devices with a modified optical fiber core end surface [23-48]. The core end surface is the distal end of the core where the light beam leaves or enters the fiber. Different core end surface designs can cause different light propagation patterns.

Fifteen patents describe distal end designs including optical fibers with a slanted core end surface [23-37]. When light reaches the fiber tip, it is redirected by the slanted core end surface, causing light to leave or enter the optical fiber at an angle relative to the device's longitudinal axis. Depending on the angle and material properties of the slanted surface, which vary among devices, the light beam can be reflected or refracted, see Figure 3.2d. A standard design includes one optical fiber with a slanted core end surface. This surface creates an interface between optical fiberglass, typically silica, and a tissue region [23, 24]. Because of the slanted fiber tip, light approaches the surface at an oblique angle to the surface normal and refracts into the tissue, leaving the device at a small angle to its longitudinal axis. A reflective coating can be applied to the surface to generate reflection, and thereby increase the emitting angle [25-31]. A reflective coating can be a metal coating or a multilayer dielectric coating. Another method to generate a reflective surface at the slanted fiber tip is by adding a thin layer of air between a beveled tip of a light delivery fiber and a short stub fiber [32]. Total internal reflection occurs at the interface between the fiber core and the air layer because the refractive index of air is significantly lower than that of the optical fiber core. More advanced designs include multiple optical fibers with slanted surfaces that can emit light towards the tissue and collect light from the tissue [33-37]. The emitting and collecting fibers' core end surfaces can be in the same cross-sectional plane [33, 37] or separated in longitudinal direction to increase the distance between various core end surfaces [34-37]. The device described by Huang et al. [33] contains a slanted collecting fiber tip without a reflective coating. Therefore, light is collected from the tissue at a small angle to the device's longitudinal axis. The other

devices contain a reflective slanted surface to enable light delivery to and collection from tissue off-axis.

Another possible fiber core end design is a conical shape as described in seven patents [23, 38-43]. The cone can be polished either positively [23, 38-41] or negatively [42, 43]. For a standard positively polished tip, the conical surface forms an interface between two media: fiberglass and tissue [23, 38-40]. Most light rays that strike the cone wall for the first time reflect totally, as their incidence angle is greater than the critical angle. These reflected light rays then strike the opposing wall of the cone with an incident angle lower than the critical angle, causing radial refraction of the light beam into the tissue, see Figure 3.2e. The device of Scheller [41] describes a unique positively polished cone-shaped fiber tip design with four slanted surfaces that split the light into four separate beams that travel in individual directions. Two devices include a design for a negatively polished tip [42, 43]. This surface always contains a reflective coating that ensures that all light that strikes the cone is reflected into the tissue [42, 43] or collected from the tissue [43] in radial direction.

Four patents describe distal end designs with specifically shaped core end surfaces [44-47] that enable light to leave the optical fiber in axial and radial direction. In these devices, the fiber core end includes a series of slanted or cone-shaped surfaces. The light incident on these surfaces is reflected or refracted into the tissue in radial direction, see Figure 3.2f.

Lastly, Auld [48] describes a special fiber core end surface. In this device, the fiber tip is a conventional flat polished surface perpendicular to the fiber's longitudinal axis. However, a coating with a monolayer of hollow glass microspheres is attached to the core end surface. These microspheres provide a significant change in refractive index by the glass-air-glass interface. The light beam entering these spheres refracts four times, resulting in light being emitted into the tissue with a wide angular distribution, see Figure 3.2g.

ADDING AN OPTICAL ELEMENT OUTSIDE THE OPTICAL FIBER

Twenty-three patents describe distal end designs that redirect light by an optical element outside the optical fiber [26, 29, 33, 34, 39, 49-66]. In these devices, light exits the optical fiber in axial direction and propagates into

an additional distal tip of the medical device (said to be coupled to the distal end of the optical fiber). For example, this can be done by affixing the distal tip to the distal end of the buffer layer of the optical fiber [49] or to the stripped fiber core [29]. The body of the distal tip can consist of various bio-compatible and transparent materials. The distal tip can include different optical elements.

Eleven patents describe designs including one or more reflective surfaces fixed within an additional distal tip [29, 34, 39, 49-56]. In four of these devices, the distal tip has one single inclined reflective surface that is optically coupled to one optical fiber and redirects light off the fiber axis into the tissue [29, 49-51], see Figure 3.2h. This surface can consist of various materials such as polymer, glass, metal, or ceramic. To decrease leakage of light in undesired directions, it can have a metal or dielectric coating, or it can be entirely made of a highly reflective metal such as gold or silver. Alternatively, it is possible to create a highly reflective surface by adding an air cavity behind an inclined surface made of glass [51]. In three devices, the reflective surface coupled to one optical fiber can have a conical shape [39, 52], directing light into the tissue in radial direction, or a curved shape [53], converging or diverging the light rays. In two patents, one single reflective surface is coupled to multiple optical fibers [54, 55], allowing for light delivery to and collection from tissue off-axis. After exiting an optical fiber, light is redirected off the fiber axis into the tissue by a reflecting surface, and the scattered light from the tissue is redirected back into another optical fiber by the same reflective surface. The reflective surface can be convex [55], straight inclined [54], or step-wise inclined [55], see Figure 3.2i. In two more patents, multiple reflective surfaces are separately linked to individual optical fibers [34, 56]. These devices are also used to emit and collect light at an angle off-axis.

Another optical component that can be added outside the optical fiber to steer a light beam is a lens, as described in twelve patents [26, 33, 57-66]. A lens redirects a light beam due to refraction, changing its angular distribution. Lenses can be divided into converging and diverging lenses. In six devices, the distal tip includes a converging lens [26, 33, 57-60]. These converging lenses can be semi-spherical [57, 58] or convex lenses [26, 33, 58-60]. In most standard designs, a converging lens focuses a light

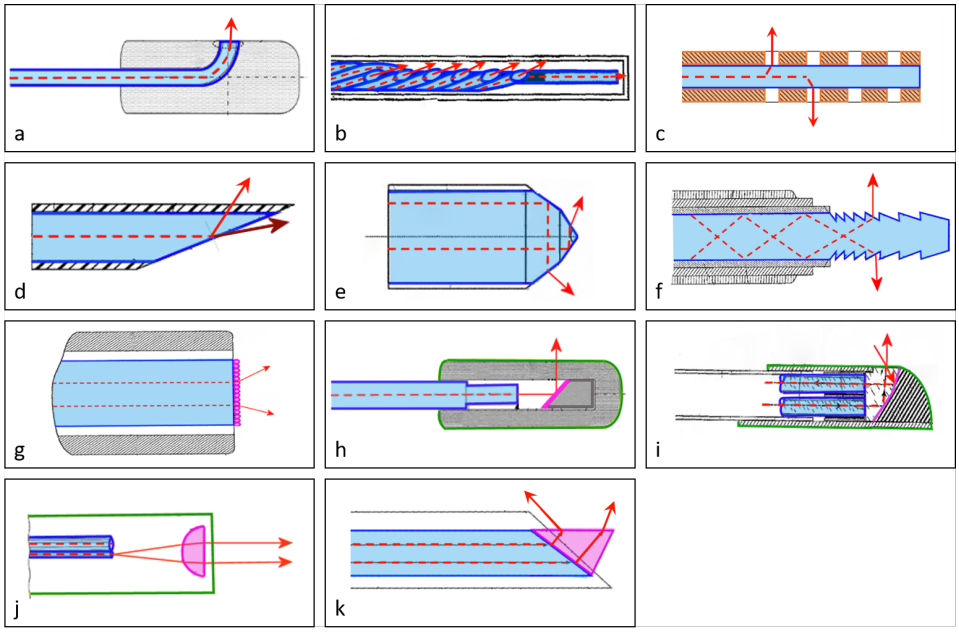

FIGURE 3.2: Distal end designs of fiber-optic medical devices to steer a light beam towards the tissue with refraction and reflection. In the design sketches, blue lines delimitate the fiber core; dashed red lines indicate the center of the light beam within the fiber; red arrows indicate the light leaving the fiber. a Bent fiber with path curved away from the central axis of the device (adapted from [14]). b Twisted fibers in six-around-one configuration (adapted from [20]). c Fiber with removed fiber cladding (orange) that forms a side-facing tip (adapted from [21]). d Fiber tip with slanted core end surface with reflected (bright red) and refracted (dark red) light beam (adapted from [24]). e Fiber tip with cone-shaped core end surface (adapted from [40]). f Fiber tip with multiple slanted surfaces in axial direction (adapted from [46]). g Fiber with micro-sphere coating (pink) at core end surface (adapted from [48]). h Distal tip (green) with slanted surface (pink) (adapted from [49]). i Distal tip (green) with varying bevel reflecting surface (pink) (adapted from [55]). j Distal tip (green) with semi-spherical lens (pink) (adapted from [49]). k Fiber with prism (pink) (adapted from [66]).

beam on a specific tissue area [26, 33, 57-60], see Figure 3.2j. The same converging lens can also collect light from this specific tissue area to one or more collecting fibers [33, 57]. Smith [60] describes a special design including a converging lens and a faceted surface. The faceted surface receives light from the optical fiber and refracts it into different beam elements, which are then focused into multi-spots by a convex lens. In six devices, the distal tip includes a diverging lens [61-66]. This can be a semi-spherical [61-63], gradient-index [64], or concave [65] lens. Diverging

lenses illuminate a wide area in the tissue. Nagale et al. [66] describe a special type of diverging lens, which is a triangular prism. The distal tip of this device consists solely of a prism that is directly coupled to the optical fiber. A light beam entering the prism refracts at the first face and then refracts again at the second face. As a result, light is emitted radially with a wide angular distribution. The prism can also rotate, allowing light to be emitted into the tissue in a 360° range, see Figure 3.2k.

SCATTERING

MODIFYING THE TOTAL INTERNAL REFLECTION PATTERN INSIDE THE OPTICAL FIBER

Devices that diffusely scatter light into the tissue by special features within the core or cladding of the fiber are described in seven patents [67-73]. In all of these devices, light is redirected within an optical fiber through scattering events caused by multiple changes in the refractive index. The scattering causes light to strike the interface between the core and the cladding from various angles. The angle can be lower than the critical angle for total internal reflection, resulting in diffuse light exiting the optical fiber in radial direction along its length. In a simple design, a scattering region containing scattering particles [67, 68] or nanovoids [69] is incorporated into the distal section of the optical fiber core. Examples of scattering particles that can be embedded within the optical fiber core are titania or silica. Nanovoids are small bubbles that can be formed, for example, by focusing a high-power laser on an optical fiber. Because the refractive index of both particles and nanovoids is different from that of the host medium, they generate scattering events, see Figure 3.3a. Luloh et al. [70] describe a device with an entire core made of translucent instead of transparent material. The changes in refractive index within the translucent material cause scattering events all along the core.

A device can also have a scattering region within the optical fiber cladding, as described in two patents [71, 72]. In the device of Skutnik [71], a region of the cladding consists of a nanoporous structure including scattering particles, which can be diamond dust, titania, alumina, powdered sapphire, powdered zirconia, or powdered quartz, see Figure 3.3b. In the device of Mersch [72], a region of the cladding consists of multiple rough surfaces.

Lastly, a distal end design can include a scattering region that is formed by distorting part of the optical fiber core and cladding [73]. A deformation pattern is created in parts of the optical fiber by a series of controlled tension, heating, elongation and cooling cycles. This deformation pattern generates light scattering within the distorted regions, see Figure 3.3c.

MODIFYING THE OPTICAL FIBER CORE END SURFACE

Three patents describe distal ends with a redesigned optical fiber core end surface that diffusely scatters light into the tissue [70, 74, 75]. A transparent spherical portion can be formed at the fiber tip [70, 74]. Before the light beam refracts into the tissue, the curved surface of the spherical portion evokes several reflection events through total internal reflection. Due to the many reflection events of separate light rays, light scatters in multiple directions, enabling wide dispersion of light into the tissue, see Figure 3.3d.

Another approach to diffuse light is to create a rough fiber core end surface [75]. Hamada [75] describes a cone-shaped fiber tip design with a rough surface finish that generates light scattering due to light interaction with the irregularities on the rough surface, see Figure 3.3e.

ADDING AN OPTICAL ELEMENT OUTSIDE THE OPTICAL FIBER

Sixteen patents describe devices that achieve light scattering by a separate diffuser tip joined to the distal end of an optical fiber [67, 68, 76-89]. Light leaves the optical fiber core in axial direction and enters the diffuser tip.

Thirteen devices describe a diffuser tip that consists of a transparent host medium including scattering particles [67, 68, 76-86]. The host medium can be composed of polymeric materials such as epoxy, polyurethane, or similar materials. Scattering particles used in diffuser tips are alumina, silica, or titania. The most basic design of a diffuser tip includes one region with scattering material [67, 68, 76-80], see Figure 3.3f. When a light beam enters the scattering material and strikes a particle, scattering events occur that cause light to leave the diffuser tip diffusely. The region with scattering material can have a cylindrical [67, 68, 76-78], semi-spherical [79], or conical shape [80], which will affect the illumination profile of the

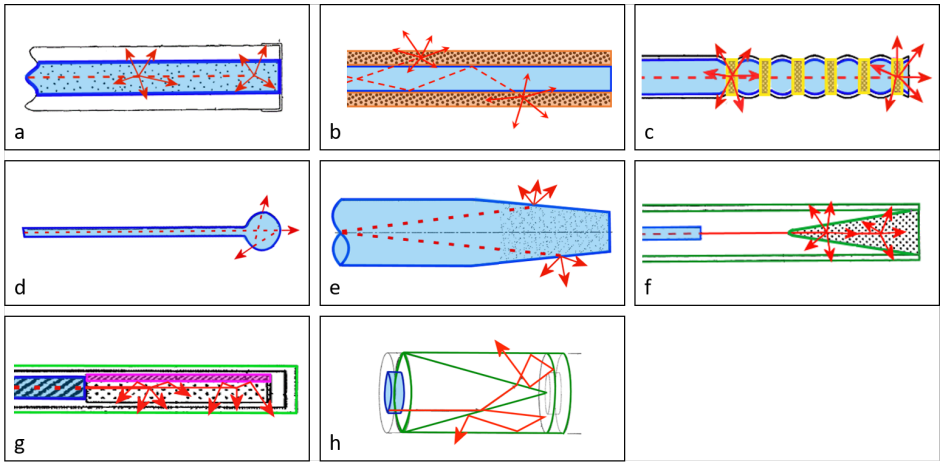

FIGURE 3.3: Distal end designs of fiber-optic medical devices to steer a light beam towards the tissue with scattering. In the design sketches, blue lines delimitate the fiber core; dashed red lines indicate the center of the light beam within the fiber; red arrows indicate the light leaving the fiber. a Fiber with scattering particles (black dots) within fiber core (adapted from [69]). b Fiber with scattering particles (black dots) within cladding (orange) (adapted from [71]). c Fiber including distorted scattering regions (yellow) (adapted from [73]). d Fiber tip with sphere-shaped core end surface (adapted from [74]). e Fiber tip with rough, cone-shaped fiber core end surface (adapted from [75]). f Diffuser tip with conical region (green) including scattering particles (black dots) (adapted from [80]). g Diffuser tip (green) including scattering particles (black dots) and reflector surface (pink) (adapted from [84]). h Diffuser tip with multiple reflective surfaces (green) (adapted from [87]).

diffusely reflected light. A more advanced diffuser tip can also include several layers of scattering particles with different scattering properties [81, 82]. These properties are chosen to ensure uniform emission of light along the length of the diffuser tip. The diffuser tip with scattering particles can also include an additional reflective surface [84-86]. In such devices, the reflective surface acts as a shield to reflect the diffuse light exclusively in the desired direction. The reflective shield can be designed such that the light diffuses in axial direction with a wide angular distribution [86] or in axial and radial direction [84, 85], see Figure 3.3g. Smith [83] describes a special diffuser tip containing a scattering region with a polymer-dispersed liquid crystal. In the absence of an electric field, the crystals in the polymer are randomly oriented, scattering the incoming light. When an electric field is applied on the diffuser tip, the crystal molecules within the polymer align parallel to the electric field. Because the aligned crystal

molecules reduce the material's scattering coefficient, light beam diffusion is reduced when an electric field is applied.

Four patents describe cylindrical diffuser tip designs that generate light scattering by several reflection events within a volume surrounded by reflective surfaces [78, 87-89]. A basic example is given by Henriksson [87]. This diffuser tip consists of two or more materials with different refractive indices. Therefore, there are at least two interfaces: one between the two materials and another between the outer material and the surrounding tissue. Light is reflected several times between these interfaces before refracting into the tissue. This results in a scattered light beam that leaves the diffuser tip in several directions, see Figure 3.3h. In addition, one of the reflective surfaces within the diffuser tip can also have a rough texture to increase light diffusion [78, 89]. Kikuchi and Kobayashi [88] describe a special diffuser tip. In this device, light that is scattered in several reflection events passes through a phosphor layer before leaving the diffuser tip, generating photoluminescence in random directions.

DIFFRACTION

MODIFYING THE TOTAL INTERNAL REFLECTION PATTERN INSIDE THE OPTICAL FIBER

One patent describes a distal end design with a modified optical fiber core to induce diffraction [90]. This patent discloses a device that includes an optical fiber with a diffraction grating. A diffraction grating is an optical element with evenly spaced slots or grooves that divide the element into sections. Between the boundaries of the individual sections, there are small openings. If the size of these openings is in the range of the wavelength of the incident light, diffraction of light occurs. The diffraction direction is strongly dependent on both the shape of the diffraction grating and the wavelength of the incident light. As a result, well-defined diffraction gratings can steer light of specific wavelengths in the desired direction. In the device described by Zerfas [90], the diffraction grating is an angled optical grating aligned along a plane non-normal to the longitudinal axis of the optical fiber. This grating can be a fiber Bragg grating that is designed to redirect light of a specific wavelength off the fiber axis while transmitting light of other wavelengths, see Figure 3.4a.

MODIFYING THE OPTICAL FIBER CORE END SURFACE

No patents were found in this category.

ADDING AN OPTICAL ELEMENT OUTSIDE THE OPTICAL FIBER

Seven patents describe devices where light is redirected by diffraction outside the optical fiber [27, 37, 50, 88, 91-93]. Light leaves the optical fiber in axial direction and propagates into an additional distal tip containing a diffractive optical element. A basic example of a diffractive optical element is a single small aperture [37]. Size and shape of this aperture determine how light propagates between the optical fiber terminating end and the region lateral to the probe.

Another commonly used diffractive optical element is a diffraction grating. The most basic designs include one diffraction grating, which is optically coupled to the terminating end face of the optical fiber [27, 50, 88]. This grating can be a transmission grating [27, 88] or a reflective grating [50]. Fairneny [27] gives a basic example of a device including a transmission grating located in the outer part of the additional distal tip. This grating can have a saw tooth pattern or any other pattern, including one or more curves. The device emits light to the tissue with a defined intensity and a wide angular distribution, see Figure 3.4b. Kikuchi and Kobayashi [88] describe a distal tip design including a Fresnel lens. If the section sizes of the Fresnel lens are in the range of the wavelength of the incident light, the control is predominantly diffractive. Yu et al. [50] describe a device including a reflective grating. The reflective grating is an inclined surface with a periodic pattern. This surface redirects light off the fiber axis and can be used to shape the light beam to a specific illumination profile such as a line, a donut, or split beams.

Three patents describe more advanced distal tips [91-93]. In these designs, the optical fiber terminating end is optically coupled to a gradient index (GRIN) lens, which is optically coupled to a diffraction grating. The GRIN lens collimates and expands the light that exits the optical fiber core. This collimated light strikes the diffraction grating, which diffracts every light beam into several narrow beams at a desired angular separation to create a multi-spot diffraction pattern with high intensity on the target tissue, see Figure 3.4c.

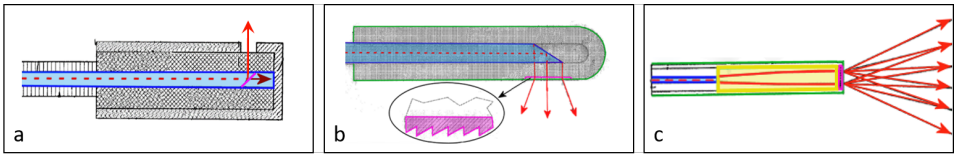

FIGURE 3.4: Distal end designs of fiber-optic medical devices to steer a light beam towards the tissue with diffraction. In the design sketches, blue lines delimitate the fiber core; dashed red lines indicate the center of the light beam within the fiber; red arrows indicate the light leaving the fiber. a Angled grating (pink) within fiber core with reflected (bright red) and transmitted (dark red) light beam (adapted from [90]). b Distal tip (green) with transmission grating (pink) (adapted from [27]). c Distal tip (green) with GRIN-lens (yellow) and diffraction grating (pink) (adapted from [93]).

DISCUSSION

This review provides an overview of all patents found on the distal end design of fiber-optic medical devices that can steer light in the desired direction before or after interacting with tissue. The comprehensive titles and abstracts written by experts based on the claims and the novelty of the patents provided by the DII database facilitated a complete overview of the patent literature. Nine categories were identified based on the working principle to steer light and the design strategy that was employed. Of the 81 relevant patents, 80% have been published and filed by companies, 16% by individual inventors, and only 4% by academic institutions, indicating that this research field is primarily industry-driven. Furthermore, because 58% of the patents are still valid in the United States or in at least one European country, light beam steering by the distal end design of a fiber-optic device seems to be feasible and a relevant research subject. The distribution of the various categories across the active patents demonstrates that light beam steering can be achieved using a variety of unique designs.

According to the temporal distribution of patents over the different categories, see Figure 3.5a, it becomes clear that refraction/reflection is the most common method for light beam steering at the distal end of fiber-optic medical devices in the last 20 years. A possible explanation is that achieving refraction/reflection within a fiber-optic device is simple, and many unique designs are possible, each with a different effect on the propagation direction of light. As can be seen in the temporal distribution,

an optical element outside the optical fiber and a modified core end surface are most commonly used to achieve refraction/reflection. To accomplish scattering, an optical element outside the optical fiber is the most popular strategy. The temporal distribution also shows that this research involves only few devices that use diffraction to steer light. This can be due to the high complexity of diffraction gratings, which is not needed for the functionality of most devices included in this review. However, devices with a diffraction grating exist in a variety of other applications, including imaging devices and pressure and temperature sensors [6, 94].

As previously stated, light beam control in medical devices can be used to meet one of five challenges:

(1) emit light at an angle off-axis;

(2) collect incident light at an angle off-axis;

(3) increase the angular distribution of light;

(4) decrease the angular distribution of light;

(5) split light into multiple beams.

An overview of the challenges that can be met with different distal end designs is given in Figure 3.5b.

Emitting light at an angle off-axis is a challenge that has been thoroughly investigated. All designs include an optical element that induces refraction/reflection or diffraction to direct the light. However, an interface to reflect or refract (96%) light in a specific direction is prevalent compared to a diffraction grating (4%). Using diffraction to emit light at an angle off-axis is a more complex method that could only be useful if the emitted light must have specified features, such as a specific pattern or wavelength. Among the devices that use refraction/reflection, there is no clear preference for one design strategy to emit light at an angle off-axis, as the best strategy depends heavily on the function and the target area of the fiber-optic device. A trade-off must be found between the device's complexity and a number of desirable features, including compactness, light intensity, longevity, reduced overheating, and patient safety [32].

Light collection at an angle to the device's longitudinal axis is a challenge with little diversity in the developed designs: all collecting devices included in this review were developed for tissue spectroscopy and make use of refraction or reflection. As refraction/reflection can equally direct a light beam consisting of different wavelengths from a specific tissue region into an optical fiber with a small cross-section, it is a convenient approach for the collection of spectral information off-axis. Patents exist for all of the design strategies. However, none of the patents using the reflective surface inside the optical fiber, such as bent and twisted fibers, are active anymore. This indicates that the design may not have given the desired results, since the respective patents were not extended.

Emitting light with a wide angular distribution is a design challenge that has been thoroughly investigated. The use of a scattering element (76%) is clearly preferred over diverging lenses or coatings (21%) and diffraction gratings (3%). This is because the two latter only increase the angular distribution of a light beam propagating in one specific direction, whereas scattering elements offer the possibility of uniform light distribution over 360°, as required by various applications such as light-induced therapy or illumination [11, 95, 96]. Among scattering devices, the number of results within each design category demonstrates a clear preference for using a diffuser tip outside the optical fiber to scatter the light. This design strategy has the advantage that it does not require complex fabrication, and the use of scattering particles within an external diffuser tip makes it possible to control the scattering effect by varying the size, material or concentration of the particles [97].

In contrast to the findings for increasing the angular distribution, there is little variation in the designs to decrease the angular distribution of light: all seven devices include a converging lens outside the optical fiber. Because light exiting the optical fiber is always slightly divergent due to total internal reflection within the fiber, placing an optical component outside the optical fiber is the only design option to reduce the angular distribution [11]. Variety exists in the choice of the converging lens: it can be refractive (86%) or diffractive (14%). Using diffraction requires a more complex design; however, diffraction lenses have the advantage of being

compact and lightweight, and allow to select a desired wavelength of operation.

The last challenge for light beam control is to split the beam into multiple narrow beams, which is accomplished by only seven devices included in this review. These designs can use a diffraction grating (71%) or a faceted surface that induces refraction/reflection (29%). A diffraction grating is most frequently used because it can serve additional purposes, such as separating light of different wavelengths or creating a multi-spot pattern. Because diffraction gratings include microscopic features that make them challenging to fabricate within the optical fiber core or core end surface [98], using an optical element outside the optical fiber is preferred over other design strategies.

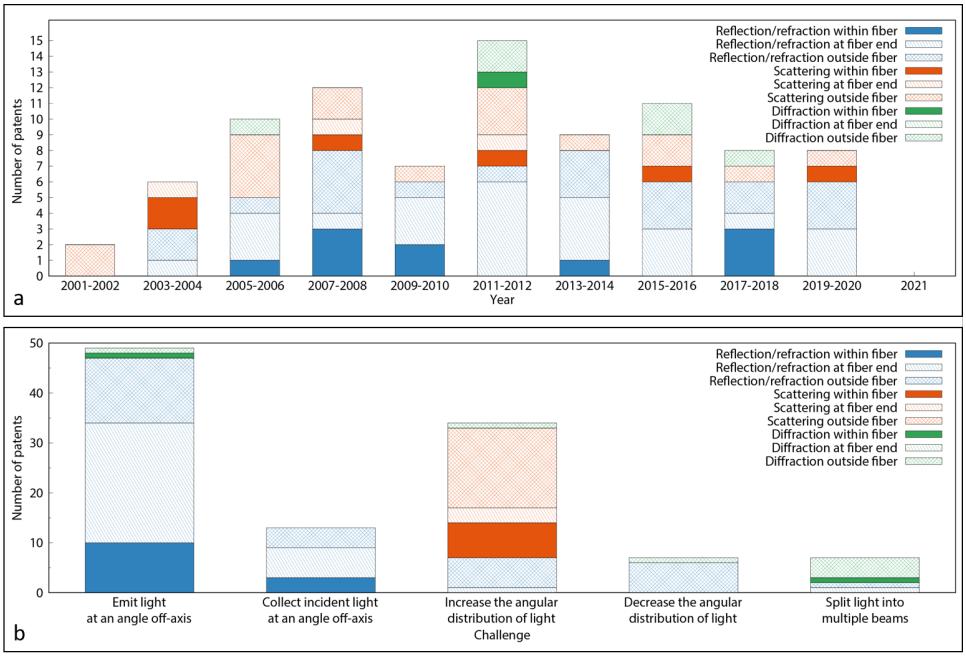

FIGURE 3.5: a Temporal distribution of distal end designs described in relevant patents published between 2001-2021, categorized based on the working principle to steer light and the design strategy that was employed. b Distribution of distal end designs described in relevant patents over challenges met, categorized based on the working principle to steer light and the design strategy that was employed.

CONCLUSION

This review article provides a comprehensive overview and categorization of the patent literature on distal end designs of fiber-optic medical devices that can steer light in the desired direction. The medical section of the Web of Science DII database was reviewed, and a total of 81 patents published during the last 20 years were discussed. The possible distal end designs were categorized based on the working principle and design strategy for light beam control.

The most common way for steering a light beam in the desired direction is by refraction or reflection. This working principle is preferred to emit and collect light at an angle off-axis and to decrease the angular distribution of light. Scattering with an optical element outside the optical fiber is preferred to increase the angular distribution of light, whereas diffraction with an optical element outside the optical fiber is preferred to split light into multiple beams.

This overview of different distal end designs can be used to identify new design challenges. One of the challenges is to implement diffraction gratings within the optical fiber or at the fiber core end surface. Furthermore, this review reveals that there are still several opportunities to design innovative devices that can collect light at an angle off-axis, reduce the angular distribution of light, or split light into multiple beams. The focus of new designs must remain on optimizing light beam control, mechanical robustness, and patient safety.

EXPERT OPINION

DESIGN SUITABILITY FOR MEDICAL PURPOSES

The retrieved patents show that remote light delivery is an issue relevant to various applications involving tissue diagnostics and therapeutics. Spectroscopic devices use light to assess tissue type and status based on its optical properties [99]. Physicians apply spectroscopy to recognize diseases [100] and to distinguish tumors from healthy tissue [101]. On the other hand, photodynamic therapy is used to treat cancer by destroying malignant cells with a combination of light energy and a photosensitive

drug [102]. Light can also provide treatment for various other medical conditions, such as benign prostatic hyperplasia [103], kidney and bladder stones [104], or incontinence [105]. New designs can support tissue diagnostics and therapeutics in hardly accessible locations of the body by providing light delivery to and collection from tissue off-axis.

In this review, it became apparent that some medical disciplines are especially demanding of light beam control. Prevalent medical disciplines mentioned in the patents are ophthalmology [13, 16, 19, 23, 24, 41, 48, 59-64, 67, 68, 70, 79, 83, 91, 93], cardiovascular surgery [15, 39, 40, 42, 43, 46, 52, 55, 65, 80, 84], and dentistry [21, 22, 74, 75].

Ophthalmology is a discipline in which optimal illumination is crucial to guarantee surgical safety and effectiveness [106]. Therefore, light diffusion has found its way into surgical practice in the last decennia. New designs contribute to the growing diversity of surgical illumination options. A second widespread ophthalmologic application is laser photocoagulation, a surgery frequently carried out to prevent vision loss in patients affected by diabetes [107], retinopathy of prematurity [108], and other ocular indications. Nagpal et al. [109] have shown that multi-spot photocoagulation leads to faster, less painful procedures with less collateral damage than standard laser treatment, while achieving similar retinopathy regression in diabetic patients. New designs to create multi-spot patterns therefore show great potential for application in laser photocoagulation.

In cardiovascular surgery, light is employed for vessel ablation, blood embolization and tissue welding. Laser procedures for the ablation and reparation of blood vessels have been carried out since the 1970s [110, 111]. New designs help to create more versatile tools for this standard surgical procedure.

Dental applications of light beam steering include the treatment of plaque (bacterial microfilms) and tartar (calcified deposits) on teeth and gums by photodisinfection. Photodisinfection employs light of specific wavelengths to eradicate a broad variety of oral microorganisms to prevent or treat oral diseases without inducing resistance [112]. New designs provide better

elimination of pathogens by monitoring dosimetry and direction of the administered light.

In all of the abovementioned applications, light is already being employed for illumination, spectral tissue sensing, or cell modification, which shows the validity of the applications proposed in the patents. Better light beam steering can improve these procedures and make the innovative devices usable in areas inaccessible with conventional fiber-optic probes.

FURTHER RESEARCH

This review focuses on the distal end of fiber-optic devices that steer light towards the tissue or collect light after interacting with tissue. The search was restricted to devices with direct light tissue interaction for illumination, spectral tissue sensing, laser surgery, or light-induced therapy. Therefore, this research does not include other fiber-optic devices such as imaging devices and temperature, pressure and shape sensors, even though these devices also exert a high level of light control. Especially diffraction is used in many imaging devices to produce multi-spot patterns on tissue. Including imaging devices could thus provide a more detailed overview of all possible distal end designs. Furthermore, because fiber-optic devices are not only used in the medical field, the results of other fields could also lead to a more extensive overview with new creative ideas for steering light in the desired direction.

This review was based on the patent literature published in the last 20 years to provide an overview of the latest distal end designs to steer a light beam. As patents do not present any performance results, additional exploration of the corresponding scientific literature will provide more insights in the technical feasibility for choosing the optimal design for a particular application, and might even reveal certain designs that have not been patented by their inventors.

Furthermore, many applications impose additional requirements on the device, such as certain mechanical properties, prevention of overheating, removal of debris, and patient safety. These are crucial factors to take into consideration in future developments of fiber-optic medical devices.

FIVE-YEAR VIEW

The temporal distribution of distal end designs shows that light beam steering has become more popular throughout the 2000s, with a peak in the development of new devices in 2011-2012 when fifteen new patents were issued within two years. Since then, the number of new inventions has remained on a stable level of around ten new patents/two years, indicating that this field is more consolidated now, but still very active with new designs emerging all the time.

The distribution of patents included in this review over the different categories reveals a gap in the development of devices that use diffraction inside the optical fiber or at the fiber core end surface to steer a light beam. This indicates that these two design strategies still have innovative potential in the development of fiber-optic devices for illumination, spectral tissue sensing, or cell modification. For example, a slanted core end surface including a diffractive grating could direct light of a specific wavelength off the fiber axis with the desired illumination profile or multi-spot pattern, while directing light of another wavelength in axial direction.

The number of different designs for steering light, as well as the number of designs disclosed in active patents show that there are only few devices that can collect light at an angle off-axis, reduce the angular distribution of light, or split light into multiple beams. This implies that numerous new developments are possible to address these design challenges. For example, only five designs described in active patents can collect incident light under an angle [33, 34, 36, 56]. Of these designs, only the devices described in three patents [34, 36, 56] can collect incident light perpendicular to the fiber's longitudinal axis. Because these patents only describe collecting fibers that are integrated into biopsy devices or catheters, a design for light collection off-axis can still be developed for a wide range of applications.

Finally, next to the conventional optical fibers treated in this review, there is an ongoing development of special fibers, which has led to inventions such as microstructured optical fibers [113, 114], polarization maintaining fibers [115], and low-loss optical fibers [116]. When such trends are picked up by the medical industry, the combination of the light beam steering

principles explored in this review with special fibers will result in a great range of new medical devices.

REFERENCES

1. Méndez, Alexis. "Optics in medicine." Optics in Our Time (2016): 299-333.
2. Floris, Ignazio, et al. "Fiber optic shape sensors: A comprehensive review." Optics and Lasers in Engineering 139 (2021): 106508.
3. Roriz, Paulo, et al. "Optical fiber temperature sensors and their biomedical applications." Sensors 20.7 (2020): 2113.
4. Poeggel, Sven, et al. "Optical fibre pressure sensors in medical applications." Sensors 15.7 (2015): 17115-17148.
5. Correia, Ricardo, et al. "Biomedical application of optical fibre sensors." Journal of Optics 20.7 (2018): 073003.
6. Schena, Emiliano, et al. "Fiber optic sensors for temperature monitoring during thermal treatments: An overview." Sensors 16.7 (2016): 1144.
7. Amanzadeh, Moe, et al. "Recent developments in fibre optic shape sensing." Measurement 128 (2018): 119-137.
8. Jelínek, Filip, et al. "Minimally invasive surgical instruments with an accessory channel capable of integrating fibre-optic cable for optical biopsy: A review of the state of the art." Proceedings of the Institution of Mechanical Engineers, Part H: Journal of Engineering in Medicine 228.8 (2014): 843-853.
9. Keiser, Gerd, et al. "Review of diverse optical fibers used in biomedical research and clinical practice." Journal of biomedical optics 19.8 (2014): 080902-080902.
10. Yu, Xia, et al. "Micro-and nano-fiber probes for optical sensing, imaging, and stimulation in biomedical applications." Photonics Research 8.11 (2020): 1703-1724.
11. Utzinger, Urs, and Rebecca R. Richards-Kortum. "Fiber optic probes for biomedical optical spectroscopy." Journal of biomedical optics 8.1 (2003): 121-147.

12. Tipler, Paul A., and Gene Mosca. Physics for scientists and engineers. Macmillan, 2007.

13. Auld, Jack R. "Ophthalmic endoilluminators with directed light". US patent US 9066678 B2. (2011)

14. Hanley, Brian M. "Side-firing laser fiber with internal bent fiber and related methods". US patent US 8657812 B2. (2009)

15. Munger, Gareth T. "Magnetically enabled optical ablation device". US patent US 20070049909 A1 (2006)

16. Kern, Thomas. "Vitreous cutter with integrated illumination system". US patent US 10307290 B2 (2016)

17. Hendriks, Bernardus H. W. "Obtaining optical tissue properties". US patent US 20090326385 A1 (2007)

18. Mansour, Hebah N. "Methods and sensors for monitoring internal tissue conditions". US patent US 7930015 B2 (2006)

19. Diao, Chenguang. "Multi-fiber multi-spot laser probe with articulating beam separation". US patent US 20200390603 A1 (2020)

20. Cottrell, William J. "Side-firing linear fiber optic array for interstitial optical therapy and monitoring using compact helical geometry". US patent US 2009/0221921 A1 (2007)

21. Bollinger, James E. "Method and apparatus for disinfecting or sterilizing a root canal system using lasers targeting water". WO patent WO 2009/064947 A1 (2008)

22. Bruder, George. "Synergistic ultrasonic, sonic or electric energy and light transmitting probe for disinfection of root canals during an endodontic procedure". US patent US 11090135 B2 (2017)

23. Grieshaber, Hans R. "Method and device for the pathology analysis of the Schlemm's canal". US patent US 8747299 B2 (2011)

24. Yadlowsky, Michael J. "Illuminated microsurgical instrument including optical fiber with beveled end face". US patent US 9561085 B2 (2014)

25. Harschack, Alexander. "High Durability Side Fire Optical Fiber for High Power Applications". US patent US 2011/0166562 A1 (2010)

26. Williamson, Steven L. "Focusing fiber optic". US patent US 7039275 B2 (2002)

27. Fairneny, Ty. "Side Fire Laser Assembly With Diffractive Portion". US patent US 2011/0299557 A1 (2011)

28. Hasenberg, Thomas C. "Surgical laser system and laser fiber". US patent US 10426547 B2 (2018)

29. Loeb, Marvin P. "Novel devices for effective and uniform shrinkage of tissues and their unique methods of use". US patent US 2014/0088571 A1 (2013)

30. Yeik, Glenn D. "Side firing optical fiber device for consistent, rapid vaporization of tissue and extended longevity". US patent US 2014/0107630 A1 (2013)

31. Hixon, Jessica. "Laser fiber capillary apparatus and method". US patent US 2009/0326525 A1 (2009)

32. Pinnow, Douglas A. "Apparatus and methods for side-fire optical fiber assembly suitable for medical applications". US patent US 10603109 B2 (2018)

33. Huang, Zhiwei. "Diagnostic instrument and methods relating to raman spectroscopy". US patent US 2015/0216417 A1 (2013)

34. Reich, Christian. "Side-looking lung biopsy device". US patent US 10405838 B2 (2015)

35. Ramanujam, Nirmala. "Side-firing probe for performing optical spectroscopy during core needle biopsy". US patent US 2005/0203419 A1 (2005)

36. Braun, Augustinus L. “Biopsy device”. EP patent EP 2265161 B1 (2009)

37. Zuluaga, Andres F. “Side firing fiber optic array probe”. US patent US 2005/0165315 A1 (2004)

38. Rizoiu, Ioana M. “Modified-output fiber optic tips”. EP patent EP 1711849 B1 (2005).

39. Griffin, Stephen E. “Radial emissions from optical fibers”. US patent US 10092356 B2 (2015)

40. Seymen, Ali A. “Fiber probe that emits a pair of ring beams for laser ablation”. US patent US 2020/0237439 A1 (2018)

41. Scheller, Gregg D. “Multiple Target Laser Probe”. US patent US 2008/0051770 A1 (2007)

42. Neuberger, Wolfgang. "Endoluminal laser ablation device and method for treating veins”. US patent US 9693826 B2 (2009)

43. Tang, Jing. “Shaped fiber ends and methods of making same”. US patent US 2009/0227993 A1 (2009)

44. Rabiner, Robert A. “Systems and methods for internal bone fixation”. US patent US 8906030 B2 (2012)

45. Bissig, Alois. “Light delivery device”. US patent US 9067059 B2 (2009)

46. Wu, Xinmin. “Fiber optic laser surgical instrument having a radial dispersion pattern”. US patent US 10543042 B2 (2014)

47. Shang, Hua. “Photodynamic therapy diagnostic device capable of optical fiber puncture”. US patent US 10463876 B1 (2019)

48. Auld, Michael D. “Optic fiber instrument with microsphere diffraction surface”. WO patent WO 2006/084124 A2 (2006)

49. Hanley, Brian. “Side-firing laser fiber with protective tip and related methods”. US patent US 2018/0214211 A1 (2018)

50. Yu, Honggang. "Side-fire laser fiber having a molded reflective surface". EP patent EP 3270810 B1 (2015)

51. Sudarshanam, Venkatapuram S. "Side-firing optic fiber tip with length-based beam diameter". WO patent WO 2010/075368 A1 (2009)

52. Frenz, Martin. "Apparatus for applying light to a vessel wall". US patent US 7108692 B2 (2003)

53. Brown, Joe D. "Interchangeable forward or sidefiring tip with stand off catheter". US patent US 2019/0018195 A1 (2018)

54. Furnish, Simon M. "Miniature fiber optic spectroscopy probes". WO patent WO 2007/146254 A2 (2007)

55. Fulghum, Stephen. "Optical probe for Raman scattering from arterial tissue". US patent US 2007/0038123 A1 (2006)

56. Furnish, Simon M. "Catheter probe arrangement for tissue analysis by radiant energy delivery and radiant energy collection". US patent US 8386023 B2 (2011)

57. Jono, Junichi. "Probe". US patent US 8942523 B2 (2011)

58. Li, Jamie. "Laser assembly having adjustable focusing lenses". US patent US 9987090 B2 (2011)

59. Diao, Chenguang. "Multi-fiber multi-spot laser probe with simplified tip construction". US patent US 2020/0397614 A1 (2020)

60. Smith, Ronald T. "BSS-only multi-sport laser probe". US patent US 10111778 B2 (2014)

61. Maholtra, Madan. "Wide angle illumination system and method". US patent US 2017/0333151 A1 (2016)

62. Smith, Ronald T. "Beveled Tip Surgical Wide-Angle Illuminator". US patent US 2009/0161384 A1 (2008)

63. Hickingbotham, Dyson. "Surgical wide angle illuminator". EP patent EP 1522290 B1 (2004)

64. Charles, Steven T. “Gradient index surgical illuminator”. US patent US 7824089 B2 (2007)

65. Paamand, Rune T. “Optical energy delivery and sensing apparatus”. GB patent GB 2562526 B (2017)

66. Nagale, Sandra. “Methods and devices for targeted ablation of tissue”. US patent US 10695128 B2 (2016)

67. Mirsepassi, Alireza. “Diverging light from fiber optics illumination delivery system”. US patent US 10859748 B2 (2020)

68. Peterson, Erik W. “Application of highly scattering materials to surgical illumination”. US patent US 10441156 B2 (2015)

69. Neuberger, Wolfgang. “Medical light diffusers for high power applications and their manufacture”. WO patent WO 2008/024397 A2 (2007)

70. Luloh, K. Peter. “Apparatus and method for illuminating a field of view within an eye”. US patent US 2003/0169603 A1 (2003)

71. Skutnik, Bolesh J. “Device and method to scatter optical fiber output”. US patent US 6810184 B2 (2002)

72. Mersch, Steven H. “Durable fiber optic diffuser tip and method of making same”. US patent US 6576163 B2 (2001)

73. Sinofsky, Edward L. “System and method for optical fiber diffusion”. WO patent WO 2010/051463 A2 (2009)

74. Williams, Jill A. “Method and apparatus for filling a dental root canal”. US patent US 7306459 B1 (2005)

75. Hamada, Kazunori. “Dental laser radiation chip”. US patent US 8224138 B2 (2010)

76. Loebel, Nicolas. “Fiber optic probe for use in a medical device and method of making it”. EP patent EP 1778118 B1 (2005)

77. Levin, Philip. “Light-wand and balloon catheters”. WO patent WO 2008/066943 A2 (2007)

78. Maitland, Duncan J. "System for diffusing light from an optical fiber or light guide". US patent US 7386203 B2 (2006)

79. Nappi, Richard B. "Ophthalmic distal light diffusers and methods of making". WO patent WO 2005/052643 A2 (2004)

80. Bays, Roland. "Conical light diffuser and method of making". WO patent WO 2003/065880 A2 (2003)

81. Gowda, Ashok. "Light diffusing tip". US patent US 7412141 B2 (2007)

82. Intintoli, Alfred J. "Light-dispersive probe". US patent US 6893432 B2 (2002)

83. Smith, Ronald T. "Surgical variable-angle illuminator". US patent US 8152798 B2 (2006)

84. Ward, Jim. "Ablative treatment of atrial fibrillation via the coronary sinus". US patent US 7731715 B2 (2004)

85. Furuta, Koichiro. "Illumination device". US patent US 9753270 B2 (2015)

86. Yoshida, Koji. "Light diffusing element and light guide for endoscopes equipped with the light diffusing element". US patent US 8849079 B2 (2011)

87. Henriksson, Paer H. "A system for providing insertable probes". WO patent WO 2011/161126 A1 (2011)

88. Kikuchi, Satoru. "Illumination optical system for endscope and endoscope". US patent US 2014/0357948 A1 (2014)

89. Moor, Robert N. "Source-insensitive cylindrical light diffuser and visual indicator system for phototherapy". US patent US 2017/0340898 A1 (2016)

90. Zerfas, Jeffrey W. "Methods and apparatus related to a side-fire assembly that has an optical grating". US patent US 8870858 B2 (2010)

91. Murakami, Naho. "Ophthalmic laser treatment apparatus". US patent US 9023017 B2 (2008)

92. Kirkegaard, Henriette S. "A medical probe assembly". WO patent WO 2018/113887 A2 (2017)

93. Smith, Ronald T. "Multi-spot laser probe". US patent US 8951244 B2 (2010)

94. Yelin, Dvir, et al. "Doppler imaging using spectrally-encoded endoscopy." Optics express 16.19 (2008): 14836-14844.

95. Algorri, Jose F., et al. "Light technology for efficient and effective photodynamic therapy: A critical review." Cancers 13.14 (2021): 3484.

96. Soukos, Nikolaos S., et al. "Photodynamic therapy for endodontic disinfection." Journal of endodontics 32.10 (2006): 979-984.

97. Li, Mucong, et al. "Internal-illumination photoacoustic tomography enhanced by a graded-scattering fiber diffuser." IEEE transactions on medical imaging 40.1 (2020): 346-356.

98. Hill, Kenneth O., and Gerald Meltz. "Fiber Bragg grating technology fundamentals and overview." Journal of lightwave technology 15.8 (1997): 1263-1276.

99. Jacques, Steven L. "Optical properties of biological tissues: a review." Physics in Medicine & Biology 58.11 (2013): R37.

100. Richards-Kortum, Rebecca, and Eva Sevick-Muraca. "Quantitative optical spectroscopy for tissue diagnosis." Annual review of physical chemistry 47.1 (1996): 555-606.

101. Evers, Daniel J., et al. "Optical spectroscopy: current advances and future applications in cancer diagnostics and therapy." Future oncology 8.3 (2012): 307-320.

102. Dolmans, Dennis E. J. G. J., et al. "Photodynamic therapy for cancer." Nature reviews cancer 3.5 (2003): 380-387.

103. Kuntz, Rainer M. "Laser treatment of benign prostatic hyperplasia." World journal of urology 25.3 (2007): 241-247.

104. Rodríguez, Dayron, and Dianne E. Sacco. "Minimally invasive surgical treatment for kidney stone disease." Advances in chronic kidney disease 22.4 (2015): 266-272.

105. Ogrinc, Urška B., et al. "Novel minimally invasive laser treatment of urinary incontinence in women." Lasers in surgery and medicine 47.9 (2015): 689-697.

106. McCannel, Colin A. "Illumination considerations for vitreous surgery." Saxena S, Meyer CH, Ohji M, Akduman L: Vitreoretinal Surgery. London. Jaypee Brothers Medical Publishers (2012): 8-14.

107. Diabetic Retinopathy Study Research Group. "Preliminary report on effects of photocoagulation therapy." American journal of ophthalmology 81.4 (1976): 383-396.

108. Iverson, Deborah A., et al. "Laser photocoagulation for threshold retinopathy of prematurity." Archives of Ophthalmology 109.10 (1991): 1342-1343.

109. Nagpal, Manish, et al. "Comparison of laser photocoagulation for diabetic retinopathy using 532-nm standard laser versus multispot pattern scan laser." Retina 30.3 (2010): 452-458.

110. Bass, Lawrence S., and Michael R. Treat. "Laser tissue welding: A comprehensive review of current and future." Lasers in surgery and medicine 17.4 (1995): 315-349.

111. Esenaliev, Rinat O., et al. "Laser ablation of atherosclerotic blood vessel tissue under various irradiation conditions." IEEE transactions on biomedical engineering 36.12 (1989): 1188-1194.

112. Wilson, M. "Photolysis of oral bacteria and its potential use in the treatment of caries and periodontal disease." Journal of Applied Microbiology 75.4 (1993): 299-306.

113. Eggleton, Benjamin J., et al. "Microstructured optical fiber devices." Optics Express 9.13 (2001): 698-713.

114. Russell, Philip S. J. "Photonic-crystal fibers." Journal of lightwave technology 24.12 (2006): 4729-4749.

115. Noda, Juichi, et al. "Polarization-maintaining fibers and their applications." Journal of Lightwave Technology 4.8 (1986): 1071-1089.

116. Kapron, Felix P., et al. "Radiation losses in glass optical waveguides." Applied Physics Letters 17.10 (1970): 423-425.

4

Chapter 4
Improved breach detection with angulated fibers

published as
Losch, M. S., Kardux, F., Dankelman, J., & Hendriks, B. H. (2023). Diffuse reflectance spectroscopy of the spine: improved breach detection with angulated fibers. *Biomedical Optics Express*, 14(2), 739-750.

data available at
doi.org/10.4121/20332305.

ABSTRACT

Accuracy in spinal fusion varies greatly depending on the experience of the physician. Real-time tissue feedback with diffuse reflectance spectroscopy has been shown to provide cortical breach detection using a conventional probe with two parallel fibers. In this study, Monte Carlo simulations and optical phantom experiments were conducted to investigate how angulation of the emitting fiber affects the probed volume to allow for the detection of acute breaches. Difference in intensity magnitude between cancellous and cortical spectra increased with the fiber angle, suggesting that outward angulated fibers are beneficial in acute breach scenarios. Proximity to the cortical bone could be detected best with fibers angulated at θ_f = 45° for impending breaches between θ_p = 0° and θ_p = 45°. An orthopedic surgical device comprising a third fiber perpendicular to the device axis could thus cover the full impending breach range from θ_p = 0° to θ_p = 90°.

INTRODUCTION

Various diseases require patients to undergo spine surgery to correct for a deformity, to eliminate pain, or to treat an instability or fracture [1-3]. The prevailing treatment modality for these conditions is spinal fusion: a surgical procedure in which two or more vertebrae are "fused" together so that motion between them no longer occurs. The vertebrae are fixated in place using pedicle screws and connection rods. Pedicle screws are traditionally placed with the freehand technique, relying on anatomical landmarks for appropriate entry point selection [4, 5]. The complex nature of the procedure coupled with the heavy reliance on anatomical knowledge results in high variability in accuracy rates of pedicle screw placement of between 27.6% and 100% reported in literature [6]. Commonly used image guidance systems include conventional fluoroscopy, two-dimensional and three-dimensional navigation [7]; however, Mason et al. [8] found up to 50.3% of screws were still misplaced when using conventional fluoroscopy, and up to 19.1% when using three-dimensional fluoroscopic navigation. As the spine is a very vulnerable anatomic region, exposing nearby neural and vascular structures to risk in the case of screw misplacement, real-time tissue feedback at the tip of the pedicle screw is required such that misplacement can be detected during insertion, allowing for on-the-fly trajectory adjustment by the surgeon.

Endoscopic ultrasound imaging allows for tissue characterization in the vertebra based on the acoustic properties of bone [9]. Low frequencies provide the most favorable conditions for cortical breach detection but offer very limited image resolution [10, 11]. The variation of local tissue electrical impedance along the screw trajectory allows for the anticipation of cortical breaches through continuous conductivity measurements [12]. It does, however, not provide local signal direction.

Optical technologies enable directed measurements. Although Raman spectroscopy can be used to distinguish bone from other tissues based on their inelastic scattering behavior [13], signal weakness leads to long acquisition times and makes it less suited for real-time surgical application. Photoacoustic imaging can be used during spine surgery to distinguish compact, high-amplitude signals originating from cortical bone from

diffuse, low-amplitude cancellous bone signals [14, 15]. Implementing photoacoustics into small surgical devices is still challenging, and the required components tend to be expensive [16].

In diffuse reflectance spectroscopy (DRS), light of different wavelengths is emitted into a biological tissue, in which it is either absorbed or scattered. The scattered light can be collected, resulting in a spectrum that maps the corresponding reflectance to every wavelength. From the magnitude and shape of the spectrum, characteristic absorption and scattering properties of the tissue can be derived [17-19]. These properties depend on the tissue composition and thus allow different tissues to be distinguished. DRS can be used to study the spectral characteristics of bone tissue in real time in a non-harmful way, and its relatively simple instrumentation allows for the integration into orthopedic surgical devices [20, 21]. Previous studies have therefore proposed DRS measurements along the pedicle screw trajectory to assess fat content of the bone. The fat content varies along the transition zone of cancellous and cortical bone [22] and can be assessed to reliably anticipate cortical breaches [23-25].

These studies on DRS of the spine have used a conventional probe with two parallel fibers. However, studies on DRS for diagnostics of epithelial and dermatological conditions have shown promising results for manipulating the probed volume with the help of obliquely oriented fibers [26, 27]. Wang et al. [26] have analyzed photon propagation through Monte Carlo (MC) simulations (λ = 500 nm) and found that detection shifts toward superficially scattered photons when the detector is angulated toward the emitting fiber. This fiber constellation, they conclude, could be used for stronger reflectance acquisition of the epithelial layer at a shallow depth, whereas angulating the collecting fibers away from the emitter primarily allows for the detection of photons scattered within the underlying stromal layer. Thilwind et al. [27] have investigated depth selectivity with obliquely oriented emitting fibers through two-layered optical phantom experiments and MC simulations in the NIR range. They found that angulating the emitting fiber toward the detector allows for selective probing of the epidermis by reducing contributions from the underlying layer of the dermis, whereas outward angulation allows for more selective probing of deeper layers.

In this study, we investigate how fiber angulation can further improve cortical breach detection to enhance spine surgery. We assume that fiber angulation does not only influence the probing depth, but will affect the probed volume entirely. As breaches typically impend at non-perpendicular angles due to anatomical conditions and entry point recommendations [28], fiber angulation may specifically help to anticipate cortical breaches impending at acute angles. We conduct MC simulations and compare them with absorption experiments to evaluate the effect of fiber angulation on the probed volume. We then conduct optical phantom experiments to evaluate the capability of breach detection with DRS for different fiber angulations in a variety of breach scenarios. While perpendicular breach detection is possible regardless of the fiber angulation, higher fiber angles allow for earlier detection of acute breaches.

DRS SETUP

A conventional probe for DRS contains two parallel optical fibers placed at a fiber distance d_f. Angulating one of these fibers will change the collected DRS signal. With the orientation of the collecting fiber fixed along the axis of the optical probe, we define the fiber angulation θ_f as the angulation of the emitting fiber away from the collecting fiber, in the plane of the two fibers.

Our DRS setup comprises a custom-designed optical probe (Figures 4.1a,b, CAD files available at Ref. [50]), equipped with two fibers (step-index multimode fiber optic patch cables, core diameter 200 µm, numerical aperture (NA) = 0.22, low OH, Thorlabs Inc., Newton (NJ), USA) at a fiber distance d_f = 1.4 mm to emit and collect light to and from the tissue. Due to constructive constraints, the collecting fiber cannot be placed in the frontal plane of the emitting fiber, but is in fact placed slightly behind the emitting fiber (lateral distance d_{fl} = 1 mm, transverse distance d_{ft} = 1 mm), see Figure 4.1c. The light emitting fiber can be angulated in the frontal plane to angles θ_f [°] ∈ {0, 15, 30, 45} and is connected to a tungsten halogen broadband light source with an integrated shutter (HAL-S, Avantes, Apeldoorn, The Netherlands). The light collecting fiber is oriented along the axis of the optical probe and is connected to a NIR

spectrometer with an InGaAs detector (S330-2 NIR, HORIBA Scientific, Piscataway (NJ), USA) to collect light at 255 distinct wavelengths between 839.65 nm and 1724.27 nm. The DRS setup is shown in Figure 4.1d. The system is controlled using Philips custom-developed software.

Before the DRS measurements, the system was calibrated using a Spectralon white reference standard (WS-1-SL, Labsphere Inc., North Sutton (NH), USA). Both fibers were oriented along the axis of the optical probe, which was placed perpendicular to the standard at a distance of 3.2 mm, and an intensity calibration spectrum was acquired to compensate for any wavelength-dependent sensitivities in the setup.

METHODS

EFFECT OF FIBER ANGULATION ON THE PROBED VOLUME

MONTE CARLO SIMULATIONS

MC simulations were run to provide insight into the variation in probed volume for different fiber angulations. The simulations were carried out in MCmatlab [29], a radiative transfer equation (RTE) solver based on the mcxyz model developed by Jacques and Li [30] that conveniently combines the computational speed of C with the versatility of MATLAB. 10^9 photons of a wavelength of 1211 nm, corresponding to the most prominent absorption peak of fat in the NIR range [31], were emitted into a single-layer cancellous bone model (μ_a (1211 nm) = 1.4220, μ'_s (1211 nm) = 19.5129, g = 0.9 [24]) to investigate possible photon paths taken within this layer. The model dimensions were 4.0 mm x 4.0 mm x 3.0 mm with a resolution of 100 bins/mm (simulation run for 400 x 400 x 300 voxels).

The setup of the simulation is illustrated in Figure 4.2a. The light source emitted light at a fiber angulation θ_f [°] ∈ {0, 15, 30, 45}. To model the DRS setup as closely as possible, the emitted light was approximated by a top-hat beam with a focal plane intensity distribution width of $1/2e^2$ times the optical fiber core diameter (200 µm) and an angular intensity distribution half-angle of $1/e^2$ times the inverse sine of the optical fiber NA (0.22). The light collector was defined as an optical fiber (core diameter 200 µm, NA = 0.22) at a fiber distance d_f = 1.4 mm.

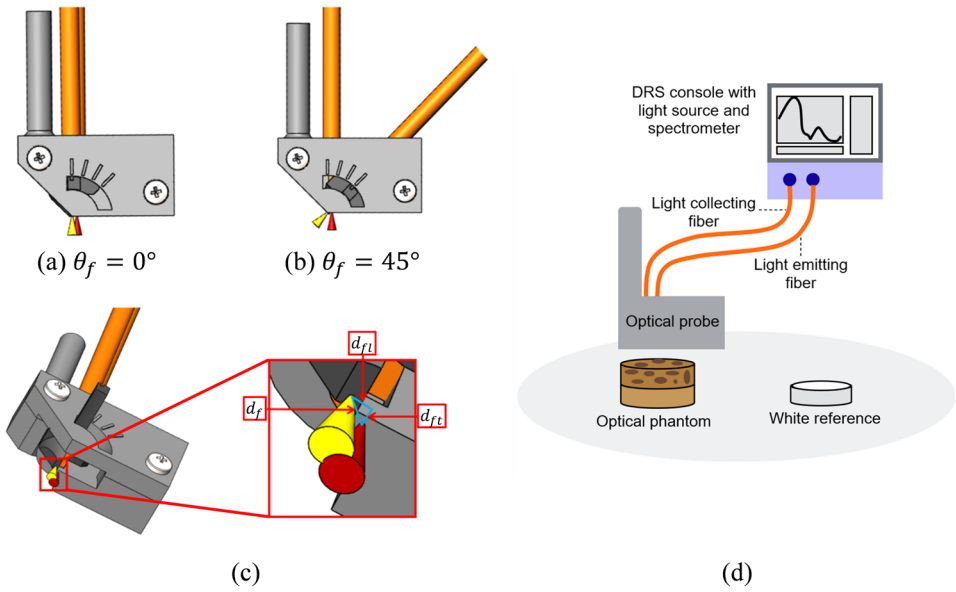

FIGURE 4.1: a-b Illustration of the custom-designed optical probe. c Detailed view of the fiber constellation. d Illustration of the DRS setup. Direction and location of the emitting fiber are indicated with a yellow cone, direction and location of the light collecting fiber are indicated with a red cone.

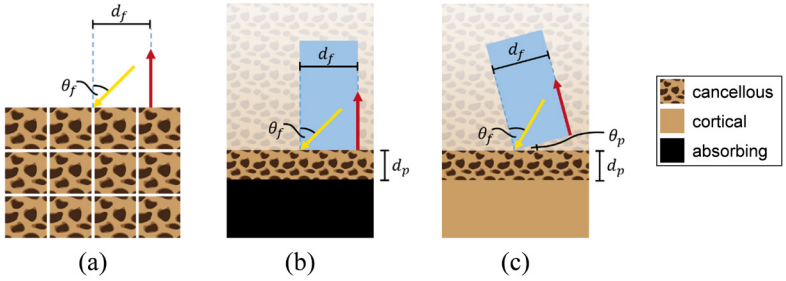

FIGURE 4.2: Illustration of the fiber angulation setup for a the simulation b the absorption experiment c the optical phantom experiment. The simulation was run for 400 x 400 x 300 voxels. The pose of the optical probe is indicated in blue for the experimental setups. Direction and location of the emitting fiber are indicated with a yellow arrow, direction and location of the light collecting fiber are indicated with a red arrow.

ABSORPTION EXPERIMENTS

The results of the MC simulations were experimentally validated in an absorption experiment on a two-layered model consisting of a fully absorbing bottom layer and a cancellous bone-mimicking top layer. The fully absorbing layer consisted of matt black tape (HPX GB4850, Option Tape Specialties NV, Temse, Belgium). The cancellous bone-mimicking layer consisted of pure coconut milk with a fat content of 18% (Go-Tan B.V., Kesteren, The Netherlands), which is a cheap and simple alternative to the Intralipid 20% IV fat emulsion (Baxter International Inc., Deerfield (IL), USA) commonly used for tissue-mimicking phantoms [32-34]. Inhomogeneity in lipid droplet size – which will be less controlled for an aliment like coconut milk than for Intralipid, an approved intravenous nutritional product – will affect the scattering properties; the absorption properties, however, are most likely not affected [31]. Absorption in the NIR range is also comparable among animal fat and plant-based fat as shown by the same study (for beef lipid vs. 100% lipid sunflower oil).

The setup of the absorption experiment is illustrated in Figure 4.2b. The probe was mounted onto a manual 25 mm linear translation stage (Thorlabs Inc., Newton (NJ), USA). At various distances to the absorbing layer d_p [mm] $\in \{0, 0.2, \dots, 3\}$, diffuse reflectance was measured with the DRS setup described above, varying the fiber angulation θ_f [°] $\in \{0, 15, 30, 45\}$. The probe was oriented perpendicular to the interface of the two model layers. Light intensity was measured at $\lambda = 1211$ nm; ten intensities were obtained at every distance. Integration time was set to 1000 ms.

EFFECT OF FIBER ANGULATION ON THE CAPABILITY OF BREACH DETECTION

To enhance spine surgery with a DRS probe with modified fiber angulation, it should allow to anticipate cortical breaches in a variety of different scenarios. A breach scenario is defined by two parameters θ_p and d_p that describe the pose of the optical probe relative to the tissue interface, which we assume to be locally plane. The probe angulation θ_p describes the angulation of the probe relative to the tissue interface. As this study aims at investigating how a modified fiber angulation can help to anticipate

acute breaches, the probe is always angulated in favor of the modified probe (*i.e.* in opposite direction of the fiber angulation), in the fiber plane. The distance to breach d_p describes the shortest distance between the distal end of the emitting fiber and the tissue interface.

OPTICAL PHANTOM EXPERIMENTS

To study the effect of fiber angulation on the measured diffuse reflectance spectrum and its influence on detecting proximity to the cortical bone boundary, an experiment was conducted on a two-layered optical phantom consisting of a cortical bone-mimicking bottom layer and a cancellous bone-mimicking top layer. The cortical bone-mimicking layer was made of water and gelatin following the production process described by Azizian Amiri et al. [35] (without addition of a lipid component). Demineralized water was mixed with NaCl (ALDI Inkoop B.V., Culemborg, The Netherlands), to which barium sulfate (Acros Organics B.V.B.A., Geel, Belgium) was added as a scattering agent. 15% gelatin (250 bloom porcine gelatin powder, Dr. Oetker, Bielefeld, Germany) was added as emulsifier and gelling agent, and sodium benzoate (Natural Spices B.V., Mijdrecht, The Netherlands) was added as a preservative. The quantities for 100 ml of phantom are listed in Table 4.1. As for the absorption experiment, the cancellous bone-mimicking layer consisted of pure coconut milk with a fat content of 18%.

TABLE 4.1: Composition of the cortical bone-mimicking layer.

water (ml)	NaCl (g)	barium sulfate (g)	gelatin (g)	sodium benzoate (g)
100	1	3	15	0.1

The setup of the optical phantom experiment is illustrated in Figure 4.2c. The probe was mounted onto a manual 25 mm linear translation stage (Thorlabs Inc., Newton (NJ), USA). At various distances to the interface of the two phantom layers d_p [mm] $\in$ {0, 0.25, ... , 2.5}, diffuse reflectance spectra were obtained with the DRS setup described above, varying the fiber angulation θ_f [°] $\in$ {0, 15, 30, 45}. The probe was angulated by θ_p [°] $\in$ {0, 15, 30, 45}. Ten spectra were registered and averaged at every location. Integration time was set to 1000 ms. The experiment was repeated three times at different points within the phantom. The averaged

spectra were filtered with a third-order Savitzky-Golay filter with a frame length of 11 to remove noise. The effect of the fiber angulation on the measured diffuse reflectance spectrum was determined for a wavelength range from 1000 nm to 1400 nm. All spectra were normalized to λ_0 = 1211 nm. Additionally, from these normalized spectra, the change in maximal intensity when approaching the interface was retained to allow for the quantitative comparison of the performance between different fiber angulations in a breach scenario. The total increase in intensity at the interface (d_f = 0 mm) was statistically evaluated in an analysis of variance (ANOVA) with post-hoc Tukey's honest significant difference (HSD) test at a significance level of 5%.

RESULTS

EFFECT OF FIBER ANGULATION ON THE PROBED VOLUME

To provide insight into the probed volume for angulated fibers, Figure 4.3a shows the normalized fluence rate of collected photons for θ_f = 0° orthogonally projected onto the plane of the two fibers. The normalized fluence rate is a three-dimensional matrix of the accumulated energy deposited into the voxels as photon packets propagate through the simulation volume, normalized to the input power and divided by the absorption coefficient to yield the irradiance of every voxel [29]. The normalized fluence rate is overlaid with the approximated probed volume (comprising the paths followed by 68.3% (mean ± 1 std) of all detected photons) for all simulated fiber angulations (θ_f [°] ∈ {0, 15, 30, 45}). The plot shows that the probed volume can be manipulated with the help of obliquely oriented fibers. The effect is predominant in the superficial tissue close to the emitting fiber, where the emitted light is deflected outward and propagates through a wider tissue volume for higher angulations. Along the photon path, the difference in probed volume among the fiber angles decreases. Close to the collecting fiber, the probed volume is completely unaffected by the fiber angulation. The probing depth is similar for all fiber angulations.

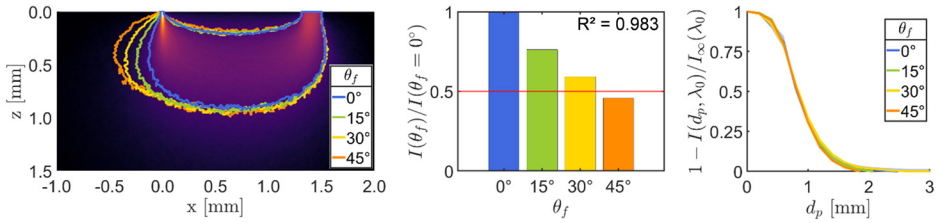

(a) (b) (c)

FIGURE 4.3: a Projected normalized fluence rate of collected photons for θ_f = 0° with indication of approximated probed volume (comprising the paths followed by 68.3% of all detected photons) for different fiber angles. b Photon count for different fiber angles relative to the photon count observed for θ_f = 0°. Red line indicates half of the original photon count. c Absorption ratio per distance to the absorbing layer for different fiber angles.

The MC simulations show that the total photon count decreases linearly with the angulation (R^2 = 0.983), as shown in Figure 4.3b. For θ_f = 45°, the photon count has decreased to less than half of the photon count observed for θ_f = 0°.

Figure 4.3c shows the ratio of absorbed photons per distance to the absorbing layer (calculated based on the photon count at the respective distance relative to the photon count observed for $d_p \rightarrow \infty$) for different fiber angles. The mean absorption ratio for θ_f = 0° is displayed as a solid line together with the 95% confidence interval highlighted in the same color. The mean absorption ratios for the other fiber angulations were plotted as solid lines in the same plot to illustrate how the fiber angulation influences probing depth and sensitivity of DRS to certain tissue depths. Despite the observation that the probed volume changes with θ_f, the absorption experiment shows that the curves for the mean absorption ratios for fiber angles θ_f > 0° lie within the confidence interval of the mean absorption ratio for θ_f = 0°.

EFFECT OF FIBER ANGULATION ON THE CAPABILITY OF BREACH DETECTION

To illustrate the influence of obliquely oriented fibers on the detection of proximity to the cortical bone boundary, Figures 4.4 and 4.5 show typical plots of the normalized reflectance spectra for approaching the

interface at the two most extreme angles θ_p = 0° and θ_p = 45°, respectively, for different fiber angulations θ_f. All spectra are plotted relative to the normalized reflectance spectrum acquired on the pure cancellous bone-mimicking phantom ($d_p \rightarrow \infty$) for the respective fiber angulation. In this way, we reconstruct a pedicle screw placement scenario in which a reference spectrum is acquired on cancellous bone at the start of the procedure. Continuous measurements along the screw trajectory allow to detect deviation from this reference spectrum, which indicates a change in tissue properties and warns the surgeon of an impending cortical breach.

A gradual change in spectrum is observed for approaching the cortical layer (blue to yellow) for all angles θ_p and θ_f. For θ_p = 0° (Figure 4.4), the difference in intensity between cancellous and cortical bone-mimicking phantom is of similar magnitude for all fiber angles θ_f.

For θ_p = 45° (Figure 4.5), the cortical curve for θ_f = 0° is visibly flatter than for approaching the interface perpendicularly, and the spacing between the spectral lines of individual distances is decreased. The spectral curves for the other fiber angulations are increasingly steeper, with the intensity difference for θ_f = 45° being the steepest and experiencing only minor change compared to θ_p = 0°.

From the plots of all probe angulations (θ_p = 15° and θ_p = 30° not shown), it can be observed that the spectral curves for low fiber angulations flatten when the probe is angulated with regard to the interface. Higher fiber angulations produce steep spectra with intensity differences remaining at a similar magnitude even when the probe is angulated.

The performance of different fiber angulations in a breach scenario can be quantitatively compared with the help of the change in maximal intensity when approaching the interface, as illustrated in Figure 4.6. The mean normalized change observed in the three experiments is displayed as a solid line together with the standard deviation highlighted in the same color. The steepness of the curve as well as the total increase in intensity provide information about how well a fiber angulation performs in a breach scenario. Asterisks indicate that the total increase in intensity at the interface is significantly different for two fiber angulations.

As indicated by the spectral curves in Figures 4.4 and 4.5, the curves in Figure 4.6 show a consistently increasing maximal intensity for approaching the interface. This is the case for all fiber angles and breach scenarios, with the exception of θ_f = 0° where the increase in maximal intensity is followed by a decrease at short distances to the interface (d_p ≤ 0.25 mm) in the acute breach scenarios.

For θ_p = 0°, no significant differences in total increase of maximal intensity at the interface were found in the ANOVA. For θ_p = 15°, Tukey's HSD revealed that all fiber angulations yield total increases that are significantly different from that of θ_f = 0°. For θ_p = 30°, all fiber angulations yield total increases that are significantly different from that of θ_f = 0°. Additionally, the increase for θ_f = 45° is significantly different from those for all other fiber angulations. For θ_p = 45°, the total increases for θ_f = 30° and θ_f = 45° are significantly different from that of θ_f = 0°.

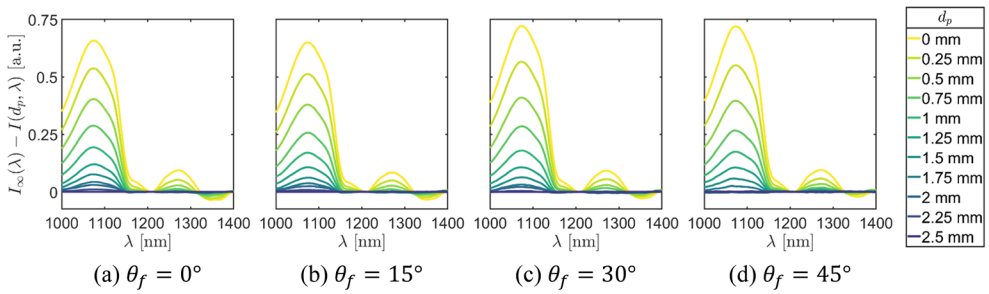

(a) $\theta_f = 0°$ (b) $\theta_f = 15°$ (c) $\theta_f = 30°$ (d) $\theta_f = 45°$

FIGURE 4.4: Normalized reflectance spectra (λ_o = 1211 nm) for different distances to the interface relative to the normalized reflectance spectrum of the pure cancellous bone-mimicking phantom, θ_p = 0°.

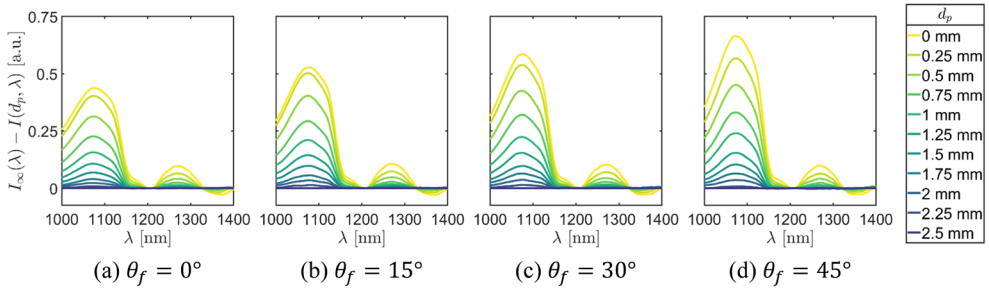

(a) $\theta_f = 0°$ (b) $\theta_f = 15°$ (c) $\theta_f = 30°$ (d) $\theta_f = 45°$

FIGURE 4.5: Normalized reflectance spectra (λ_o = 1211 nm) for different distances to the interface relative to the normalized reflectance spectrum of the pure cancellous bone-mimicking phantom, θ_p = 45°.

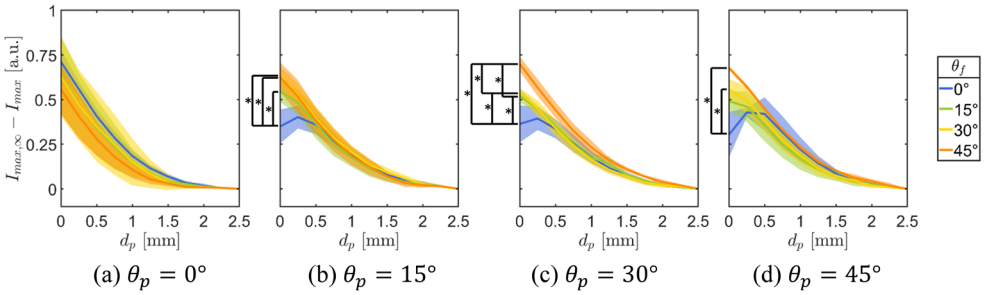

FIGURE 4.6: Normalized change in maximal intensity (λ_o = 1211 nm) for different fiber angles.

DISCUSSION

The results from the MC simulations show that the probed volume around the emitting fiber can be manipulated with the help of angulated fibers. The high anisotropy factor g of biological tissues [36] accounts for the fact that, in a single scattering event, photons are typically scattered in the forward direction as described by the Henyey-Greenstein scattering function [37]. The propagation direction of photons close to the emitter hence heavily depends on the fiber angulation. At higher tissue depths, however, and after a high number of scattering events, total light diffusion occurs, and photons travel regardless of their initial propagation direction [38]. Angulation therefore has only limited potential to change the probed volume, and the probing depth remains unchanged by the fiber angulation.

These observations are confirmed by the absorption experiment that indicates that photons emitted at higher angles θ_f may follow a different path, but this deflection generally occurs within tissue of the same depth, as the ratio of photons absorbed at every distance to the absorbing layer is not influenced by θ_f. Angulating the emitting fiber away from the collector hence does not influence the probing depth or sensitivity of DRS to certain tissue depths.

The influence of fiber angulation on the probing depth has previously been investigated in the context of epithelial precancer detection [26] and for the diagnosis of precancerous skin lesions [27]. In both studies, the aim of the researchers was to decrease the detection depth of DRS

with the help of a short fiber distance and oblique fibers in order to probe superficial layers without the contribution of underlying tissue layers. The selected fiber distances, in combination with fibers angulated toward each other, lead to a low number of scattering events [27] and indeed allow for selective probing of surface tissue layers. In contrast, we in our study aim at manipulating the probed volume in order to sense sideways and allow for the earlier detection of non-perpendicular breaches, which is why we selected a larger fiber distance for higher detection depth. With our setup, we emit photons away from the detector, so photons propagate outward and travel further before their detection. After a high number of scattering events, light is totally diffuse, and the probing depth is not influenced by the fiber angle.

The MC simulations further show that the total photon count decreases for oblique fibers, leading to a lower signal-to-noise ratio (SNR) for higher fiber angles. For θ_f = 45°, the photon count, and thus also the SNR, has decreased by half compared to the photon count for two parallel fibers. This is because of the angular dependence of light scattering. In bone tissue, mineralized structures cause tissue anisotropy [39], leading to a tendency toward forward scattering that causes more photons to travel away from the detector when emitted at higher angles. A second reason is that the length of the average path taken by a photon before reaching the detector increases when the photon is emitted at a higher angle. On this longer path, more absorption events take place according to Beer-Lambert law [40], leading to a lower photon count at the detector. The decrease in total reflectance is in line with findings from previous studies [26].

This decreased SNR does not seem to have a negative influence on the capability of breach detection, as shown by the results of the optical phantom experiments. Difference in intensity between cancellous and cortical bone-mimicking phantom could be observed for all probe and fiber angulations.

For θ_p = 0°, the difference in intensity between cancellous and cortical bone-mimicking phantom is independent from the fiber angulation θ_f. This is in line with the findings from the MC simulations and absorption

experiments that the probing depth and sensitivity of DRS to certain tissue depths are unaffected by angulating the emitting fiber away from the collector. It indicates that perpendicular breach detection is possible regardless of the fiber angulation.

For $\theta_p > 0°$, the difference in intensity between cancellous and cortical bone-mimicking phantom increases with the fiber angulation θ_f. Hence, the influence of approaching the cortical layer becomes more evident in the spectra for higher fiber angles. This increase in spectral change indicates earlier detection of proximity to the cortical bone boundary with angulated fibers for breaches impending at acute angles.

This is supported by the change in maximal intensity observed for different fiber angulations. The curves show that all fiber angulations succeed to detect breaches thanks to an increase in intensity when approaching the cortical layer. Performance of all fiber angles is similar in a perpendicular breach scenario, whereas higher fiber angles perform better for acute breaches, as shown in the ANOVA.

For acute breach angles, the spectra observed for $\theta_f = 0°$ experience a decrease at short distances to the interface. This reflectance change at the interface is most likely due to a refractive index mismatch, causing specular reflection at the interface of the two phantom layers. At higher fiber angulations, this effect is not produced due to the constellation of emitting and collecting fiber that decreases the susceptibility to detect specular reflection [41]. This decrease also explains the significant difference observed in the ANOVA. Only for $\theta_p = 30°$, the highest fiber angle ($\theta_f = 45°$) performs significantly better than all other fiber angulations.

Overall, our results show that breaches of all tested scenarios can be detected with any fiber constellation, although higher fiber angles tend to perform better in acute breach scenarios. This indicates that manufacturers should aim to produce probes with high fiber angles (*e.g.*, $\theta_f = 45°$) capable of detecting breaches at both $\theta_p = 0°$ and $\theta_p = 45°$. Small deviations of angle during the production process will however not restrain the probe's ability to detect breaches.

LIMITATIONS

In our MC simulations, emitter and collector are placed in the same frontal plane (y = 0 mm). In our DRS setup, however, the collecting fiber needed to be placed at a (short) transverse distance to the emitter due to constructive constraints. As the total fiber distance was identical for simulations and experiments (d_f = 1.4 mm), we neglect the influence of the transverse distance and assume that the angulation occurs in the plane of the two fibers both times.

Another simplification in our experiments is the use of coconut milk for the cancellous bone-mimicking phantom. This choice is justified by the findings of Nachabé et al. [31].

Generally, phantoms can represent the optical tissue properties of vertebrae only to a limited extent, especially since the fat content of the cancellous bone-mimicking phantom was only 18%, which is much lower than the actual fat content of cancellous bone in vertebrae [22, 42]. However, this makes our study results applicable to many more medical scenarios in which DRS is used to distinguish tissues based on their fat content, such as for instance tumor detection and margin assessment in oncology [43-45] and needle guidance in anesthesia [46, 47]. In actual vertebrae, we would expect the difference in spectrum to be even more pronounced due to the elevated fat content of the cancellous bone.

It is an arbitrary choice to angulate the emitting fiber, but due to the time reversal invariance of Maxwell's equations, we assume the reverse process to be almost the same as the forward process. Thus, angulating either of the fibers will yield the same spectral curves. Yet, in an orthopedic surgical device, alternatives to implement light beam steering need to be found, as fiber bending is limited to the minimum bending radius of the selected optical fiber and constrained by the dimensions of the device (typically in the range of a few millimeters). Possible solutions for emitting or collecting light at an angle off-axis are reflection/refraction or diffraction of light within the probe [48]. Light beam steering with the help of optical elements such as mirrors, however, will cause divergence within the probe. This can influence the probed volume observed in our MC simulations as well as the spectra observed in our experiments, and moreover leads to further

reduction of the SNR. Converging optical elements can solve the loss of photons and increase the SNR. The space around the optical elements should be filled up with fully transparent material with a refractive index matched to blood to prevent light reflection and refraction at the interface between probe and tissue.

Although both, reflectance spectra and quantitative comparison, show a clear trend for the difference in intensity when approaching the cortical layer at acute angles with different fiber angulations, the ANOVA only reveals significance for comparing curves of θ_f = 0° and higher fiber angles, mainly thanks to the decreased intensity at the interface for two parallel fibers. The low significance of the curve comparisons among higher fiber angles can be attributed to the limited number of experiments conducted (n = 3). More experiments would be needed to establish if there are indeed significant differences in performance between fiber angles.

Finally, more elaborate data interpretation with the help of spectral fitting [31] or a classification algorithm [25, 49] is needed before DRS can actually be used during surgery.

CONCLUSION

DRS can enhance spine surgery by allowing to detect impending cortical breaches. This study investigated how fiber angulation can help to anticipate specifically non-perpendicular cortical breaches. With our results from MC simulations, absorption experiments and optical phantom experiments, we show how the use of obliquely oriented fibers allows to manipulate the probed volume to detect proximity to the cortical layer at acute angles. The increased difference in intensity for higher fiber angles suggests that cortical breach detection benefits from fiber angulation.

An orthopedic surgical device comprising two optical fibers to emit light off-axis (θ_f = 45°) and collect light along the device axis can be used to detect proximity to the cortical bone boundary along the pedicle screw trajectory for impending breaches between θ_p = 0° and θ_p = 45°. Adding a third fiber to collect light perpendicular to the device axis (at θ_f = 45° to the off-axis emitter) allows to cover the full impending breach range from θ_p = 0° to θ_p = 90°.

REFERENCES

1. Weinstein, Stuart L., et al. "Adolescent idiopathic scoliosis." The lancet 371.9623 (2008): 1527-1537.
2. Deyo, Richard A., et al. "United States trends in lumbar fusion surgery for degenerative conditions." Spine 30.12 (2005): 1441-1445.
3. Dick, Walter, et al. "A new device for internal fixation of thoracolumbar and lumbar spine fractures: the 'fixateur interne'." Spinal Cord 23.4 (1985): 225-232.
4. Boucher, Harold H. "A method of spinal fusion." The Journal of Bone & Joint Surgery British Volume 41.2 (1959): 248-259.
5. Kim, Yongjung J., et al. "Free hand pedicle screw placement in the thoracic spine: is it safe?." Spine 29.3 (2004): 333-342.
6. Kosmopoulos, Victor, and Constantin Schizas. "Pedicle screw placement accuracy: a meta-analysis." Spine 32.3 (2007): E111-E120.
7. Bourgeois, Austin C., et al. "The evolution of image-guided lumbosacral spine surgery." Annals of Translational Medicine 3.5 (2015).
8. Mason, Alexander, et al. "The accuracy of pedicle screw placement using intraoperative image guidance systems: a systematic review." Journal of Neurosurgery: Spine 20.2 (2014): 196-203.
9. Mujagic, Muris, et al. "Development of a method for ultrasound-guided placement of pedicle screws." IEEE transactions on ultrasonics, ferroelectrics, and frequency control 55.6 (2008): 1267-1276.
10. Bossy, Emmanuel, et al. "Attenuation in trabecular bone: A comparison between numerical simulation and experimental results in human femur." The Journal of the Acoustical Society of America 122.4 (2007): 2469-2475.

11. Aly, Al-Hassan, et al. "On ultrasound imaging for guided screw insertion in spinal fusion surgery." Ultrasound in medicine & biology 37.4 (2011): 651-664.

12. Bolger, Ciaran, et al. "Electrical conductivity measurement: a new technique to detect iatrogenic initial pedicle perforation." European Spine Journal 16 (2007): 1919-1924.

13. Fullwood, Leanne M., et al. "Evaluation of a multi-fibre needle raman probe for tissue analysis." Biomedical Vibrational Spectroscopy 2016: Advances in Research and Industry. Vol. 9704. SPIE, 2016.

14. Shubert, Joshua, and Muyinatu A. Lediju Bell. "Photoacoustic imaging of a human vertebra: implications for guiding spinal fusion surgeries." Physics in Medicine & Biology 63.14 (2018): 144001.

15. Gonzalez, Eduardo A., et al. "Combined ultrasound and photoacoustic image guidance of spinal pedicle cannulation demonstrated with intact ex vivo specimens." IEEE Transactions on Biomedical Engineering 68.8 (2020): 2479-2489.

16. Liu, Li, et al. "A photoacoustics-enhanced drilling probe for radiation-free pedicle screw implantation in spinal surgery." Frontiers in Bioengineering and Biotechnology 10 (2022): 1000950.

17. Farrell, Thomas J., et al. "A diffusion theory model of spatially resolved, steady-state diffuse reflectance for the noninvasive determination of tissue optical properties in vivo." Medical physics 19.4 (1992): 879-888.

18. Evers, Daniel J., et al. "Optical spectroscopy: current advances and future applications in cancer diagnostics and therapy." Future oncology 8.3 (2012): 307-320.

19. Doornbos, Richard M. P., et al. "The determination of in vivo human tissue optical properties and absolute chromophore concentrations using spatially resolved steady-state diffuse reflectance spectroscopy." Physics in Medicine & Biology 44.4 (1999): 967.

20. Duperron, Matthieu, et al. "Diffuse reflectance spectroscopy-enhanced drill for bone boundary detection." Biomedical optics express 10.2 (2019): 961-977.

21. Fisher, Carl, et al. "Perspective on the integration of optical sensing into orthopedic surgical devices." Journal of Biomedical Optics 27.1 (2022): 010601.

22. Losch, Merle S., et al. "Proton density fat fraction of the spinal column: an MRI cadaver study." BioMedical Engineering OnLine 20 (2021): 1-11.

23. van Veen, Robert L. P., et al. "Determination of visible near-IR absorption coefficients of mammalian fat using time-and spatially resolved diffuse reflectance and transmission spectroscopy." Journal of biomedical optics 10.5 (2005): 054004-054004.

24. Swamy, Akash, et al. "Diffuse reflectance spectroscopy, a potential optical sensing technology for the detection of cortical breaches during spinal screw placement." Journal of biomedical optics 24.1 (2019): 017002-017002.

25. Burström, Gustav, et al. "Diffuse reflectance spectroscopy accurately identifies the pre-cortical zone to avoid impending pedicle screw breach in spinal fixation surgery." Biomedical optics express 10.11 (2019): 5905-5920.

26. Wang, Adrien M. J., et al. "Depth-sensitive reflectance measurements using obliquely oriented fiber probes." Journal of biomedical optics 10.4 (2005): 044017-044017.

27. Thilwind, Rachel E., et al. "Improved depth resolution in near-infrared diffuse reflectance spectroscopy using obliquely oriented fibers." Journal of biomedical optics 14.2 (2009): 024026-024026.

28. Chung, Kook J., et al. "Ideal entry point for the thoracic pedicle screw during the free hand technique." International orthopaedics 32 (2008): 657-662.

29. Marti, Dominik, et al. "MCmatlab: an open-source, user-friendly, MATLAB-integrated three-dimensional Monte Carlo light transport solver with heat diffusion and tissue damage." Journal of biomedical optics 23.12 (2018): 121622-121622.

30. Jacques, Steve L., et al. mcxyz (2019): https://omlc.org/software/mc/mcxyz/index.html.

31. Nachabé, Rami, et al. "Estimation of lipid and water concentrations in scattering media with diffuse optical spectroscopy from 900 to 1600 nm." Journal of biomedical optics 15.3 (2010): 037015-037015.

32. Driver, Ian, et al. "The optical properties of aqueous suspensions of Intralipid, a fat emulsion." Physics in Medicine & Biology 34.12 (1989): 1927.

33. Flock, Stephen T., et al. "Optical properties of Intralipid: a phantom medium for light propagation studies." Lasers in surgery and medicine 12.5 (1992): 510-519.

34. Pogue, Brian W., and Michael S. Patterson. "Review of tissue simulating phantoms for optical spectroscopy, imaging and dosimetry." Journal of biomedical optics 11.4 (2006): 041102-041102.

35. Azizian Amiri, Sara, et al. "Tissue-mimicking phantom materials with tunable optical properties suitable for assessment of diffuse reflectance spectroscopy during electrosurgery." Biomedical Optics Express 13.5 (2022): 2616-2643.

36. Tuchin, Valery V. "Tissue optics and photonics: light-tissue interaction." Journal of Biomedical Photonics & Engineering 1.2 (2015): 98-134.

37. Henyey, Louis G., and Jesse L. Greenstein. "Diffuse radiation in the galaxy." Astrophysical Journal, vol. 93, p. 70-83 (1941). 93 (1941): 70-83.

38. Vo-Dinh, Tuan. "Biomedical Photonics." (2003).

39. Tuchin, Valery V. "Tissue optics and photonics: biological tissue structures." Journal of Biomedical Photonics & Engineering 1.1 (2015): 3-21.

40. Swinehart, Donald F. "The beer-lambert law." Journal of chemical education 39.7 (1962): 333.

41. Fanjul-Vélez, Félix, et al. "Application of classification algorithms to diffuse reflectance spectroscopy measurements for ex vivo characterization of biological tissues." Entropy 22.7 (2020): 736.

42. Ruschke, Stefan, et al. "Measurement of vertebral bone marrow proton density fat fraction in children using quantitative water–fat MRI." Magnetic Resonance Materials in Physics, Biology and Medicine 30 (2017): 449-460.

43. Evers, Daniel J., et al. "Diffuse reflectance spectroscopy: towards clinical application in breast cancer." Breast cancer research and treatment 137 (2013): 155-165.

44. de Boer, Lisanne L., et al. "Fat/water ratios measured with diffuse reflectance spectroscopy to detect breast tumor boundaries." Breast cancer research and treatment 152 (2015): 509-518.

45. Evers, Daniel J., et al. "Optical sensing for tumor detection in the liver." European Journal of Surgical Oncology (EJSO) 39.1 (2013): 68-75.

46. Rathmell, James P., et al. "Identification of the Epidural Space with Optical Spectroscopy: An In Vivo Swine Study." The Journal of the American Society of Anesthesiologists 113.6 (2010): 1406-1418.

47. Balthasar, Andrea, et al. "Optical detection of peripheral nerves: an in vivo human study." Regional Anesthesia & Pain Medicine 37.3 (2012): 277-282.

48. Losch, Merle S., et al. "Steering light in fiber-optic medical devices: a patent review." Expert review of medical devices 19.3 (2022): 259-271.

49. Gunaratne, Rajitha, et al. "Wavelength weightings in machine learning for ovine joint tissue differentiation using diffuse reflectance spectroscopy (DRS)." Biomedical Optics Express 11.9 (2020): 5122-5131.

50. doi.org/10.4121/20332305.

5

Chapter 5

A fiber-optic forward- and sideways-looking DRS probe

published as

Losch, M. S., Dankelman, J., & Hendriks, B. H. (2024). Seeing from a new angle: design of a sideways-looking fiber-optic probe to advance spine surgery. In *Advanced Biomedical and Clinical Diagnostic and Surgical Guidance Systems XXII* (Vol. 12831, pp. 46-53). SPIE.

ABSTRACT

Our research highlights the potential of Diffuse Reflectance Spectroscopy (DRS) in detecting cortical breaches during pedicle screw placement. We propose a sideways-looking fiber-optic probe, integrating diffuse light emission with both forward and sideways light collection. Experiments on an optical tissue phantom validate the probe's potential to distinguish bone tissues and provide real-time guidance for spine surgery. Our findings prove that DRS with diffuse emission can detect perpendicular breaches, and demonstrate how the integration of a 45° slanted fiber coated with gold enables parallel breach detection, advancing spine surgery by allowing for accurate pedicle screw placement.

INTRODUCTION

As the global population ages, a surge in degenerative diseases affecting the spine is seen [1]. This demographic shift has led to an increasing demand for spinal fusion surgery [2, 3], as medical intervention is often needed for pain relief. Through spinal fusion, the structural integrity of the spinal column is restored with an assembly of metal rods and screws typically placed through the pedicles. The placement of pedicle screws is a sensitive procedure that requires high accuracy given that even minor deviations in screw trajectory can cause serious injury to the delicate osseous, neural and vascular structures.

Various guidance systems have therefore been developed, including the use of intraoperative fluoroscopy, computer-assisted navigation, and robotic-assisted surgery [4]. While these existing methods have been helpful in improving the accuracy of pedicle screw placement, the associated additional cost hinders their widespread adoption and prevents access to this technology for many surgeons and healthcare facilities.

Tissue sensing offers a potential solution to this challenge, as it allows to detect changes in the physical properties of the surrounding tissue with relatively simple instrumentation. Earlier studies have shown the integration of optical fibers into medical devices, enabling spectral tissue sensing [5-7]. Specifically, DRS has demonstrated great potential in distinguishing different types of tissues, including bone [8, 9], providing insights into tissue composition and structure. By probing the region ahead of the pedicle screw during insertion, DRS could provide real-time tissue feedback, enabling surgeons to monitor the trajectory of the screw to avoid cortical breaches. However, current forward-looking approaches fail to exploit the potential of DRS for generating directional tissue feedback. Concretely, enabling sideways-directed DRS measurements could provide spine surgeons with guidance for the accurate placement of pedicle screws.

Through design of the distal end of a fiber-optic medical device, the light path is determined, which offers potential to control the angular distribution of light, and to emit and collect light off axis to allow for

sideways-directed DRS measurements [10]. Emitting light diffusely into the tissue through a diffuser tip will increase the illuminated volume [11]. To cover the full range of impending cortical breaches whilst keeping the complexity of the probe low and minimizing the amount of fibers used, the probed volume can be manipulated with obliquely oriented collecting fibers [12]. Collecting light both along the device axis ("forward") as well as perpendicularly ("sideways") allows to examine the tissue ahead of and lateral to the probe tip to avoid both perpendicular and parallel breaches. To overcome spatial constraints for fiber angulation in medical devices, sideways collection is enabled by slanted optical fibers, which can be coated with silver or gold to maximize the collected intensity [13].

This paper presents the design of a sideways-looking probe incorporating optical fibers with modified tips to provide directional feedback on tissue optical properties during spine surgery. Validation experiments on an optical tissue phantom prove the probe's capabilities for distinguishing bone tissues, demonstrating how it can contribute to improved pedicle screw placement accuracy.

MATERIALS AND METHODS

OPTICAL FIBER CHARACTERIZATION

Three different fiber tips for installation in the probe were manufactured by modifying 200 µm core diameter optical fibers with numerical aperture (NA) = 0.22 (M25L02, Thorlabs Inc., Newton (NJ), USA), see Figure 5.1a: (1) forward-emitting 90° tip (2) diffuser tip (3) sideways-emitting 45° tip with gold coating. The forward-emitting fiber is a standard terminated fiber with a 90° polished end surface. The diffuser tip was created from 10% barium sulfate (Acros Organics B.V.B.A., Geel, Belgium) dissolved in NIR-transparent optical adhesive (NOA68, Norland Products Inc., Jamesburg (NJ), USA). The sideways-emitting fiber features a polished surface with a 45° slant coated with gold through sputter deposition.

The fibers were connected to a tungsten halogen broadband light source (SLS201L, Thorlabs Inc., Newton (NJ), USA), and their angular emission was examined by placing an optical power sensor (S132C, Thorlabs Inc., Newton (NJ), USA) at a distance of d_{ps} = 20 mm and rotating it 180° around

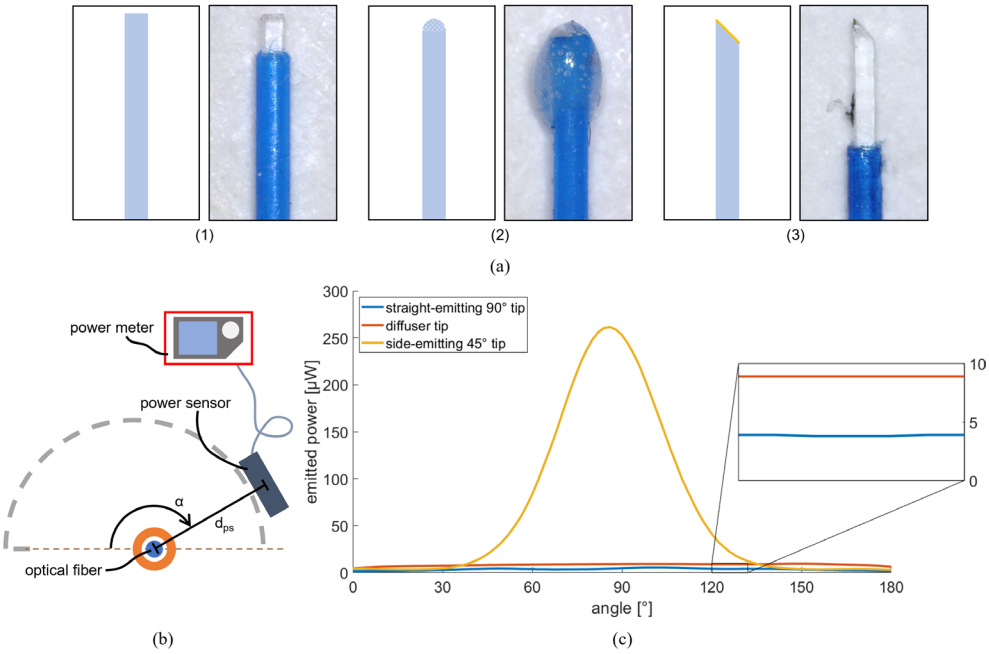

FIGURE 5.1: a Illustration and microscopic image of the three different fiber tips that were examined: (1) forward-emitting 90° tip (2) diffuser tip (3) sideways-emitting 45° tip with gold coating. b Setup of the optical fiber characterization (top view). c Angular emission of the optical fibers.

the fiber tip in $\Delta\alpha$ = 2° steps. The power sensor was read out with a power meter (PM100D, Thorlabs Inc., Newton (NJ), USA) at λ = 1310 nm. The setup is illustrated in Figure 5.1b.

While the sideways emission of the forward-emitting 90° tip is, as anticipated, very low, Figure 5.1c shows that the diffuser tip achieves almost threefold increase of sideways emission that is uniform over all angles α. The sideways-emitting 45° tip shows a Gaussian profile with a peak in emission around α = 90° that decays towards the edges to the same low value as the forward-emitting fiber, confirming that light can be steered sideways very precisely through a slanted, gold-coated optical fiber.

PROTOTYPE AND INSTRUMENTATION

A probe was designed that houses three optical fibers for diffuse light emission and forward and sideways light collection at d_f = 1.4 mm

distance each. The prototype is extended with a second, forward light-emitting fiber at d_f = 1.4 mm distance to the forward light-collecting fiber for conventional parallel DRS. The probe layout is illustrated in Figure 5.2a.

A prototype measuring 3 mm x 4 mm x 1 mm was manufactured from stainless steel, see Figure 5.2b. Either of the light emitting fibers can be connected to a tungsten halogen broadband light source with an integrated shutter (HAL-S, Avantes, Apeldoorn, The Netherlands). Either of the light collecting fibers can be connected to a NIR spectrometer with an InGaAs detector (S330-2 NIR, HORIBA Scientific, Piscataway (NJ), USA) to collect light at 255 distinct wavelengths between 839.65 nm and 1724.27 nm. The system is controlled using Philips custom-developed software and was calibrated prior to the experiments positioning the optical probe perpendicular to a Spectralon white reference standard (WS-1-SL, Labsphere Inc., North Sutton (NH), USA) at a distance of 3.2 mm.

OPTICAL TISSUE PHANTOM

Vertebrae are composite structures comprising a hard outer shell from cortical bone that surrounds the inner matrix of spongy cancellous bone, see Figure 5.3. The probe was validated on a two-layered optical tissue phantom consisting of a bottom layer simulating cortical bone made from water, NaCl (Groupe Salins, Clichy, France), 15% gelatin (250 bloom porcine gelatin powder, Dr. Oetker, Bielefeld, Germany), barium sulfate (Acros Organics B.V.B.A., Geel, Belgium), and sodium benzoate (Natural Spices B.V., Mijdrecht, The Netherlands), and a top layer simulating cancellous bone made from pure coconut milk with 19% fat (Thai Agri Foods Public Company Limited, Bang Sao Thong, Thailand) [12].

BREACH EXPERIMENTS

In the initial set of experiments, the probe's forward sensing capabilities were tested in a perpendicular breach scenario. The probe was oriented perpendicular to the interface of the two phantom layers and mounted onto a manual 25 mm linear translation stage equipped with an optical stage position encoder (Thorlabs Inc., Newton (NJ), USA). The diffuse light-emitting fiber was connected to the light source, and the forward light-collecting fiber was connected to the spectrometer. The fiber configuration is illustrated in Figure 5.4a. At various distances to the

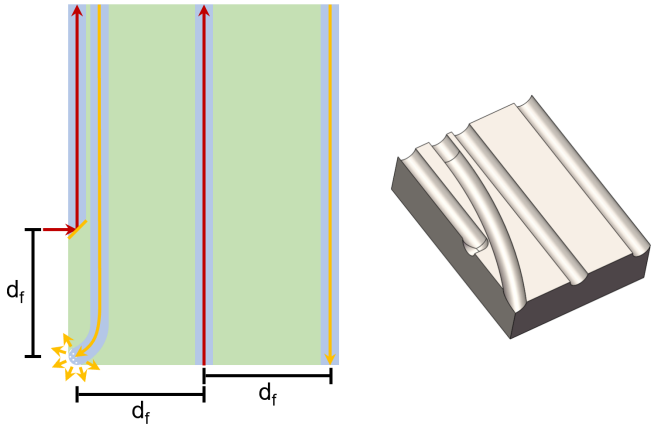

FIGURE 5.2: a Illustration of the probe layout encompassing three optical fibers for diffuse light emission and forward and sideways light collection, extended with a fourth optical fiber for forward light emission for conventional parallel DRS. b Illustration of the prototype with space for four optical fibers (dimensions: 3 mm x 4 mm x 1 mm).

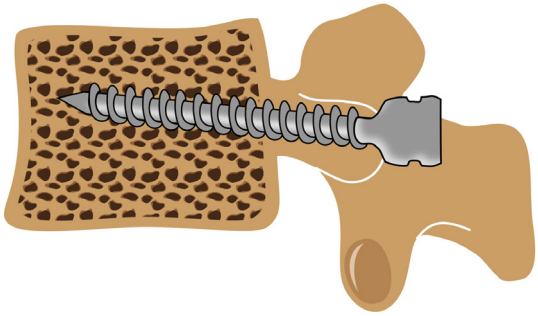

FIGURE 5.3: Illustration of a pedicle screw placed inside the vertebra (sagittal view).

interface of the two phantom layers d_p [mm] ∈ {0, 0.25, ..., 2.5}, ten diffuse reflectance spectra were measured in each case (integration time of 1000 ms), which subsequently were averaged, filtered using a third-order Savitzky-Golay filter (frame length of 11), and normalized to λ_o = 1211 nm. This experiment was repeated three times at different points within the phantom. The entire process was repeated for the conventional parallel DRS configuration, where light was emitted through the forward light-emitting fiber as illustrated in Figure 5.4b.

In the subsequent set of experiments, the probe's sideways sensing capabilities were tested in a parallel breach scenario. The probe was

mounted in parallel orientation to the interface of the two phantom layers. Light was emitted through the diffuser tip with the sideways light-collecting fiber connected to the spectrometer as illustrated in Figure 5.4c. The experimental steps from the first set of experiments were replicated, and this process was then repeated with light collection through the forward light-collecting fiber, see Figure 5.4d.

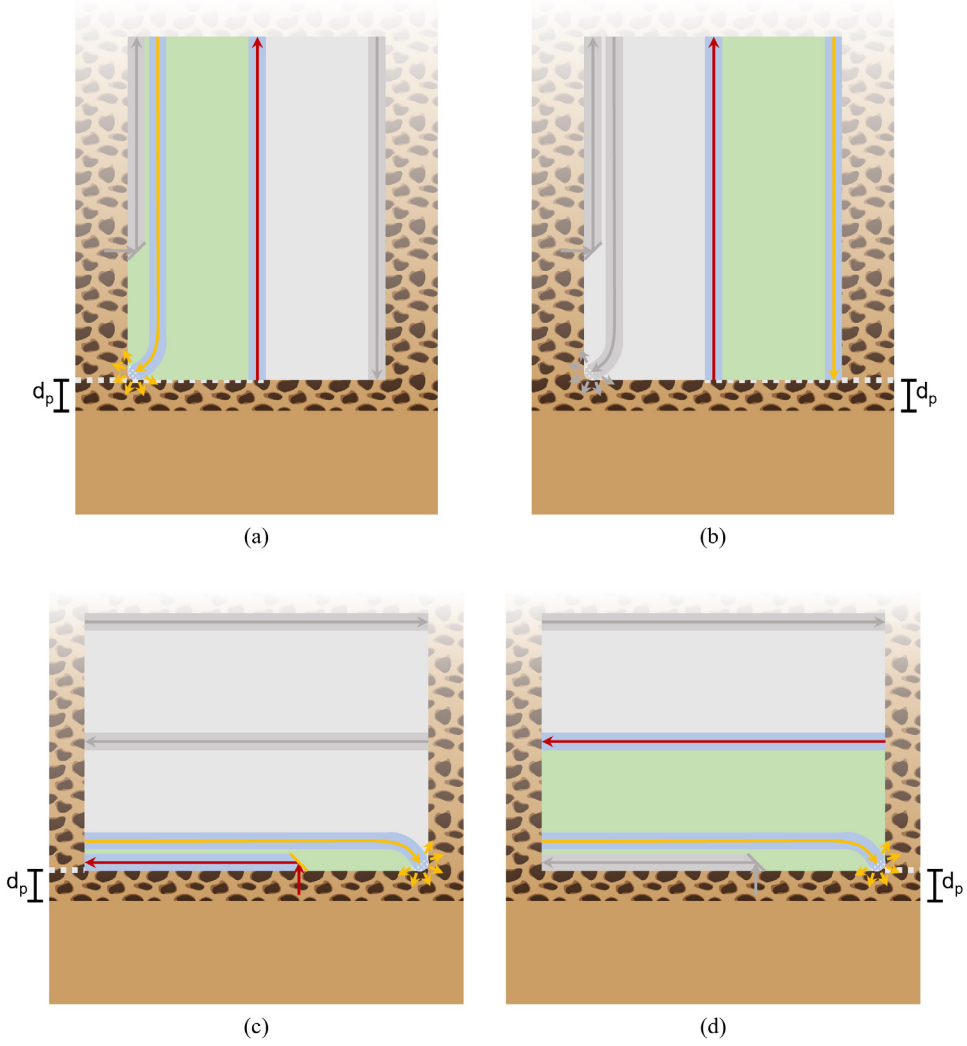

FIGURE 5.4: Illustration of the breach experiments on the two-layered optical tissue phantom in a-b perpendicular orientation c-d parallel orientation.

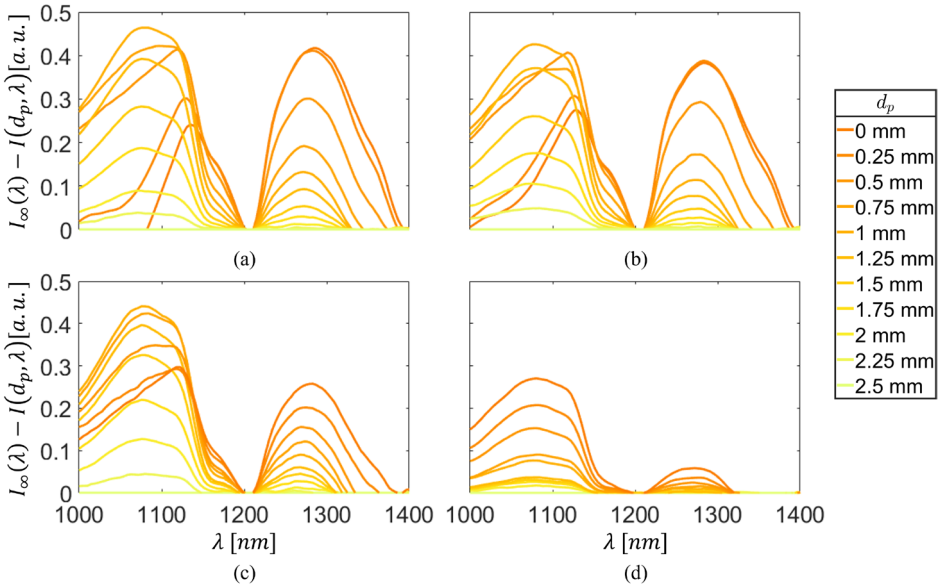

FIGURE 5.5: Normalized reflectance spectra (λ_o = 1211 nm) for different distances to the interface relative to the normalized reflectance spectrum of the pure cancellous bone-mimicking phantom with a diffuse light emission and forward light collection, perpendicular breach b forward light emission and forward light collection (conventional parallel DRS), perpendicular breach c diffuse light emission and sideways light collection, parallel breach d diffuse light emission and forward light collection, parallel breach.

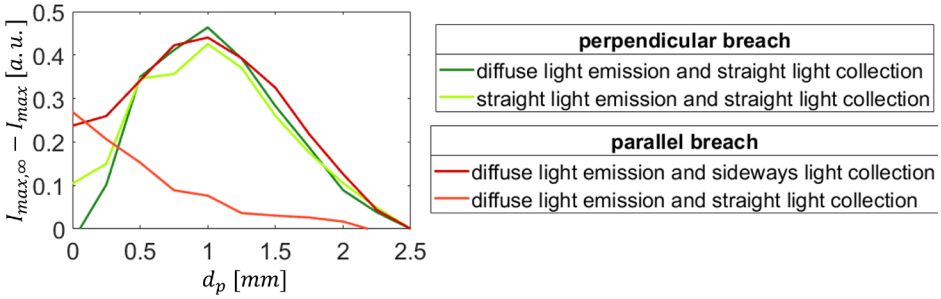

FIGURE 5.6: Normalized change in maximal intensity (λ_o = 1211 nm) for different breach scenarios and fiber configurations.

RESULTS

Figure 5.5 presents typical plots of the normalized reflectance spectra that are encountered as the probe approaches the interface between the two phantom layers, simulating two different breach scenarios (perpendicular or parallel) with different fiber configurations. The spectra are plotted relative to the normalized reflectance spectrum of the pure cancellous bone-mimicking phantom ($d_p \rightarrow \infty$) for the respective fiber configuration, enabling the detection of changes in spectrum occurring along the pedicle screw trajectory in the wavelength range of 1000 nm to 1400 nm.

Approaching the cortical bone-mimicking phantom layer perpendicularly results in a gradual change in spectrum (yellow to orange). Spectra acquired at a set distance from the interface d_p with diffuse emission (Figure 5.5a) are equivalent to those acquired with forward emission (Figure 5.5b) in their shape and magnitude.

In the parallel breach scenario, a similar gradual spectrum change is observed. Spectra acquired with sideways light collection (Figure 5.5c) are comparable in magnitude to those from the perpendicular breach scenario. With forward light collection (Figure 5.5d), however, the first change in spectrum is noticeable only relatively close to the interface (d_p = 1 mm), and the total difference in intensity is decreased between the spectrum measured on the pure cancellous bone-mimicking phantom and the spectrum measured at the interface.

Figure 5.6 provides a quantitative comparison of the different fiber configurations by illustrating the change in maximal intensity across all distances to the interface. When the interface is approached perpendicularly, the maximal intensity increases consistently with comparable slopes and total increases in intensity for both tested fiber configurations. A slight decrease in maximal intensity is experienced at short distances to the interface ($d_p \leq$ 1 mm).

Sideways light collection in a parallel breach scenario shows a very similar normalized change curve, yet with a slightly lower decrease close to the interface. In contrast, forward light collection during a parallel breach

results in a notably lower curve, characterized by a flatter slope and lower maximal value. The maximal intensity only shows an increase very close to the interface ($d_p \leq 1$ mm), aligning with observations from Figure 5.5d.

DISCUSSION AND CONCLUSION

Our experimental findings emphasize the potential of DRS for detecting cortical breaches. The increase in intensity near the cortical boundary in Figure 5.6 highlights the spectral differences between cancellous and cortical bone that can be leveraged for real-time tissue feedback. The spectral shape is also influenced by the differing scattering properties between the two phantom layers, and its gradual change is indicative of the combined scattering contributions from each layer. The decrease observed close to the interface of the two phantom layers* (Figure 5.5a-c) may be attributed to a refractive index mismatch causing specular reflection [12] This phenomenon is absent for forward light collection in a parallel breach scenario (Figure 5.5d), where the detector is not facing the interface.

In a perpendicular breach scenario, diffuse emission does not impede breach detection, as shown by the similarity between spectra obtained with both diffuse and forward emission configurations (Figures 5.5a,b, Figure 5.6). This suggests that DRS remains robust for perpendicular breach detection, irrespective of whether light is emitted to the tissue forward or diffusely. Really, diffuse emission may even facilitate sideways breach detection with a forward-collecting probe, though further investigation is required to demonstrate this correlation.

For parallel breaches, sideways light collection proves to be an important enhancement. While only minor changes in intensity are observed for forward light collection (Figure 5.5d), sideways collection, on the other hand, demonstrates important spectral differences between cancellous and cortical bone (Figure 5.5c, Figure 5.6) that match those obtained for perpendicular breach detection. This implies that diffuse emission with sideways collection provides comparable results to conventional parallel DRS. Thus, the combined approach of diffuse light emission and forward

*The exact distance at which it occurs will depend on the calibration for d_p.

and sideways light collection offers promising potential for directional tissue feedback, thereby enhancing the clinical applicability of DRS in spine surgical guidance.

LIMITATIONS

During the optical fiber characterization, we focused solely on side emission, making it challenging to precisely assess the quantity of light emitted in all directions, particularly forward. However, after proving that the diffuser tip increases sideways emission compared to a forward-emitting 90° tip, our optical tissue phantom experiments confirmed that the diffuser tip illuminates tissue in a way that enables both forward and sideways light collection.

The use of scattering particles to create the diffuser tip introduces a trade-off. Adding insufficient scattering particles may result in excessive forward emission, while an abundance of scattering particles may lead to increased backscattering into the fiber. Although our initial attempt with 10% barium sulfate appeared effective, the diffuser's performance can be optimized by exploring a range of concentrations.

Practical challenges in potential development of a DRS probe for spine surgery include the need for a white reference standard to allow for consecutive, or ideally simultaneous, calibration of both DRS systems (forward and sideways). Additionally, a mechanism to switch between inputs from both collecting fibers is essential for surgeons to determine whether a breach is impending ahead of or lateral to the probe.

Finally, while our current design incorporates a fourth optical fiber for conventional parallel DRS, our experimental findings proved its dispensability. Future miniaturization efforts could render the probe suitable for cervical vertebrae, expanding the area of potential applications.

CONCLUSION

DRS has the potential to enhance pedicle screw placement by detecting cortical breaches without compromising its ability to identify perpendicular breaches when incorporating diffuse emission. To address parallel breaches, integrating a 45° slanted fiber for lateral light collection proves effective. Combining diffuse light emission with both forward and sideways

light collection not only maintains the possibility to detect perpendicular breaches but also extends its application to scenarios involving (virtually) parallel breaches. Overall, these advancements broaden the practicality of DRS for pedicle screw placement, strengthening its potential for surgical guidance.

REFERENCES

1. Modic, Michael T., and Jeffrey S. Ross. "Lumbar degenerative disk disease." Radiology 245.1 (2007): 43-61.

2. Kobayashi, Kazuyoshi, et al. "Trends in the numbers of spine surgeries and spine surgeons over the past 15 years." Nagoya Journal of Medical Science 84.1 (2022): 155.

3. Grotle, Margreth, et al. "Lumbar spine surgery across 15 years: trends, complications and reoperations in a longitudinal observational study from Norway." BMJ open 9.8 (2019): e028743.

4. Bourgeois, Austin C., et al. "The evolution of image-guided lumbosacral spine surgery." Annals of Translational Medicine 3.5 (2015).

5. Utzinger, Urs, and Rebecca R. Richards-Kortum. "Fiber optic probes for biomedical optical spectroscopy." Journal of biomedical optics 8.1 (2003): 121-147.

6. Fisher, Michael A. "Smart pedicle tool." US patent US 8249696 B2 (2007)

7. Losch, Merle S., et al. "Fiber-Optic Pedicle Probes to Advance Spine Surgery through Diffuse Reflectance Spectroscopy." Bioengineering 11.1 (2024): 61.

8. Burström, Gustav, et al. "Diffuse reflectance spectroscopy accurately identifies the pre-cortical zone to avoid impending pedicle screw breach in spinal fixation surgery." Biomedical optics express 10.11 (2019): 5905-5920.

9. Swamy, Akash, et al. "Diffuse reflectance spectroscopy, a potential optical sensing technology for the detection of cortical breaches during spinal screw placement." Journal of biomedical optics 24.1 (2019): 017002-017002.

10. Losch, Merle S., et al. "Steering light in fiber-optic medical devices: a patent review." Expert review of medical devices 19.3 (2022): 259-271.

11. Williams, Jill A. “Method and apparatus for filling a dental root canal”. US patent US 7306459 B1 (2005)

12. Losch, Merle S., et al. “Diffuse reflectance spectroscopy of the spine: improved breach detection with angulated fibers.” Biomedical Optics Express 14.2 (2023): 739-750.

13. Green, Andrew D. M., et al. “Fibre optic probes for hysteroscopic measurement of uterine hypoxia.” European Conference on Biomedical Optics. Optica Publishing Group, 2023.

6

Chapter 6
A fiber-optic pedicle probe for spine surgery

published as
Losch, M. S., Heintz, J. D., Edström, E., Elmi-Terander, A., Dankelman, J., & Hendriks, B. H. (2024). Fiber-Optic Pedicle Probes to Advance Spine Surgery through Diffuse Reflectance Spectroscopy. *Bioengineering*, 11(1), 61.

data available at
doi.org/10.4121/9cb48608-2a57-4cc5-abae-78d78ae6e889.

ABSTRACT

Diffuse Reflectance Spectroscopy (DRS) can provide tissue feedback for pedicle screw placement in spine surgery, yet the integration of fiber optics into the tip of the pedicle probe, a device used to pierce through bone, is challenging, since the optical probing depth and signal-to-noise ratio (SNR) are affected negatively compared to those of a blunt DRS probe. Through Monte Carlo simulations and optical phantom experiments, we show how differences in the shape of the instrument tip influence the acquired spectrum. Our findings demonstrate that a single bevel with an angle of 30° offers a solution to anticipate cortical breaches during pedicle screw placement. Compared to a blunt probe, the optical probing depth and SNR of a cone tip are reduced by 50%. The single bevel tip excels with 75% of the optical probing depth and a SNR remaining at approximately 2/3, facilitating the construction of a surgical instrument with integrated DRS.

INTRODUCTION

The spine is the central support structure of the human body and provides both flexibility and stability. It consists of individual vertebrae, forming the spinal canal that functions as a protective tunnel for the spinal cord and nerves. Spinal deformities, back pain, tumors, or acute traumatic injury may require medical treatment in the form of spinal fusion [1-4]. During this surgical intervention, screws may be placed through the bone to connect adjacent vertebrae and ensure mechanical stability. Most commonly, screws are placed through the pedicles (see Figure 6.1). Accuracy is crucial for successful surgery, as misplaced screws may result in poor stability or cause severe complications such as nerve damage or spinal cord injury. Harming these vital structures can result in pain, loss of sensation, muscle weakness, or even complete paralysis below the level of injury [5, 6].

Pedicle screw misplacement frequency using the freehand technique is commonly reported at 10% [7, 8]. To improve upon this, real-time tissue feedback could be used to detect impending cortical breaches by probing ahead of the surgical instrument. Optical sensing has emerged as promising approach for tissue feedback, offering directed measurements to provide insights into tissue composition and structure. In this context, Diffuse Reflectance Spectroscopy a (DRS) has been proven to provide tissue feedback for spine surgery in a non-harmful way [9-11]. The reflectance spectra result from the interplay of light scattering and absorption by tissue constituents within the probed region. Bone tissue exhibits absorption peaks due to fat, water, and collagen, key absorbers within the wavelength range of interest (visible (VIS) – near infrared (NIR)).

DRS technology is sufficiently small to allow for integration into a variety of surgical devices, including pedicle screws [12] and surgical drills [13]. While these are feasible options, we aim to develop a more practical and effective method to integrate DRS into the surgical workflow by investigating the incorporation of optical fibers into pedicle probes, the main means for pedicle cannulation. Pedicle probes are used to pierce through bone during spinal fusion and typically have a tapered or cone-shaped tip, which poses a challenge for the incorporation of two parallel optical fibers. We explore this challenge by investigating how the optical

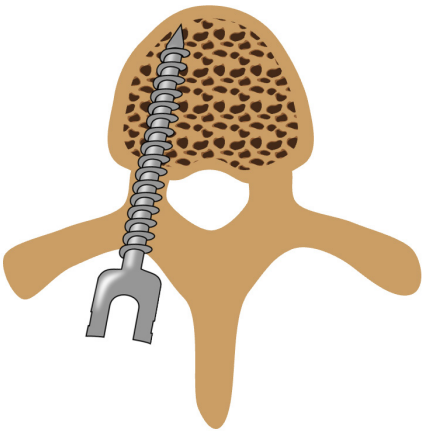

FIGURE 6.1: Illustration of a pedicle screw placed inside the vertebra (axial view).

signal is influenced by an extended, absorbing tip compared to a blunt probe. Moreover, we consider alternatives including a single-bevel design where one fiber is offset along the device axis to match the slant in a protruded position relative to the other fiber. By investigating cone and single-bevel design through Monte Carlo (MC) simulations and optical phantom experiments for different tip angles, we provide insights into the use of DRS during pedicle cannulation that highlight the importance of the tip shape of the pedicle probe.

MATERIALS AND METHODS

MONTE CARLO SIMULATIONS

To provide insight into the volume probed with different cone-shaped tips, MC simulations were run in MCmatlab [14]. In the simulation, photon packets are launched and their trajectories are traced through the simulated volume. As the photon packets propagate, energy is deposited based on the voxels' absorption coefficient, and scattering events can take place, the path length between and the scattering angle of which are computed pseudorandomly.

At λ = 1211 nm, the wavelength of maximum absorption of fat in the NIR range [15], 10^9 photons were emitted into a single-layer cancellous bone model (absorption coefficient μ_a (1211 nm) = 1.4220, reduced scattering

coefficient μ'_s (1211 nm) = 19.5129, Henyey–Greenstein scattering anisotropy factor g = 0.9 [10, 11]) with a resolution of 100 bins/mm. The extended tip (α [°] ∈ {0, 15, 30, 45, 60}) was assumed to be fully absorbing (μ_a (1211 nm) = 10^6). The scattering coefficient and anisotropy factor of the tip were set to the same values as for cancellous bone (μ'_s (1211 nm) = 19.5129, g = 0.9). The setup of the simulation is illustrated in Figure 6.2a.

To closely replicate the DRS setup, the emitted light was approximated by a top-hat beam. This beam had a focal plane intensity distribution width equal to $1/e^2$ times half the optical fiber core diameter (200 µm), and an angular intensity distribution half-angle equal to $1/e^2$ times the inverse sine of the optical fiber numerical aperture (NA) (0.22). The light collector, on the other hand, was defined as an optical fiber with a core diameter of 200 µm and an NA of 0.22, placed at a distance of d_f = 1.4 mm from the source.

For comparison, the same simulations were run for different single bevel-shaped tips. As MCmatlab does not allow for fibers to be placed inside the simulation volume, both fibers were instead tilted by α [°] ∈ {0, 15, 30, 45, 60}, and the fiber distance was adjusted to $d_f' = d_f / \cos(\alpha)$. The setup of the simulation is illustrated in Figure 6.2b.

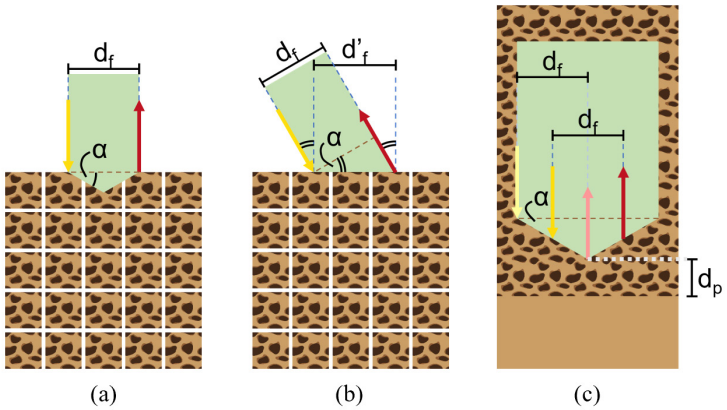

FIGURE 6.2: Illustration of the setup for a the cone simulation, b the single bevel simulation, and c the phantom experiment. The pose of the optical probe is indicated in green. The directions and locations of the emitting fibers are indicated with yellow arrows; the directions and locations of the light-collecting fibers are indicated with red arrows.

PHANTOM EXPERIMENTS

Skeletal bone is composed of a strong and compact outer layer, the cortical bone, and a less dense inner part called cancellous bone. Phantom experiments were conducted to investigate how the tip design affects the measured diffuse reflectance spectrum in the proximity of the cortical bone boundary. For the experiments, a two-layered optical phantom was created, with the bottom layer simulating cortical bone and the top layer simulating cancellous bone. The cortical bone-mimicking layer was created from a mixture of water, NaCl (Groupe Salins, Clichy, France), 15% gelatin (250 bloom porcine gelatin powder, Dr. Oetker, Bielefeld, Germany), barium sulfate (Acros Organics B.V.B.A., Geel, Belgium), and sodium benzoate (Natural Spices B.V., Mijdrecht, The Netherlands). As for the cancellous bone-mimicking layer, pure coconut milk with an 18% fat content (Go-Tan B.V., Kesteren, The Netherlands) was used as a cost-effective alternative to the commonly used Intralipid® 20% IV fat emulsion (Baxter International Inc., Deerfield (IL), USA) [11].

Based on our MC simulation results and the design of commercially available pedicle probes, we custom designed a probe with a tip of α = 30° (Figures 6.3a,b). The experimental setup illustrated in Figure 6.2c shows how the probe provides space for two pairs of parallel optical fibers (step-index multimode fiber optic patch cables, core diameter 200 µm, NA = 0.22, low OH, Thorlabs Inc., Newton (NJ), USA). The first pair consists of two fibers symmetrically arranged around the tip to emit and collect light to and from the tissue, at a distance d_f = 1.4 mm from each other (cone design); the second pair consists of one fiber at a distance d_f = 1.4 mm from the tip to emit light to the tissue and one fiber at the tip to collect light from the tissue (single-bevel design).

The probe was manufactured from stainless steel and coated with matte black spray paint (RAL 9005 matte black, Cosmos Lac, Athens, Greece). A close-up view of the probe tip with the fibers included is provided in Figure 6.3c. The light-emitting fibers can be connected to a tungsten halogen broadband light source with an integrated shutter (HAL-S, Avantes, Apeldoorn, The Netherlands). The light-collecting fibers can be connected to a NIR spectrometer with an InGaAs detector (S330-2 NIR, HORIBA Scientific, Piscataway (NJ), USA) to collect light at 255 distinct

wavelengths between 839.65 nm and 1724.27 nm. The DRS console runs Philips custom-developed software to control the system. Prior to conducting any measurements, the system underwent calibration using a Spectralon white reference standard (WS-1-SL, Labsphere Inc., North Sutton (NH), USA). The optical probe was positioned perpendicular to the standard at a distance of 3.2 mm, capturing an intensity calibration spectrum to correct for any wavelength-dependent sensitivities in the setup.

For the experiments, the probe was oriented perpendicular to the interface of the two model layers and mounted onto a manual 25 mm linear translation stage with an optical stage position encoder (Thorlabs Inc., Newton (NJ), USA). At various distances to the interface of the two phantom layers d_p [mm] $\in \{0, 0.25, \ldots, 2.5\}$, ten diffuse reflectance spectra were measured in each case, with an integration time of 1000 ms. The experiment was repeated three times at different points within the phantom. For each experiment, the ten spectra recorded at every distance were averaged and filtered with a third-order Savitzky-Golay filter (frame length of 11) to remove noise.

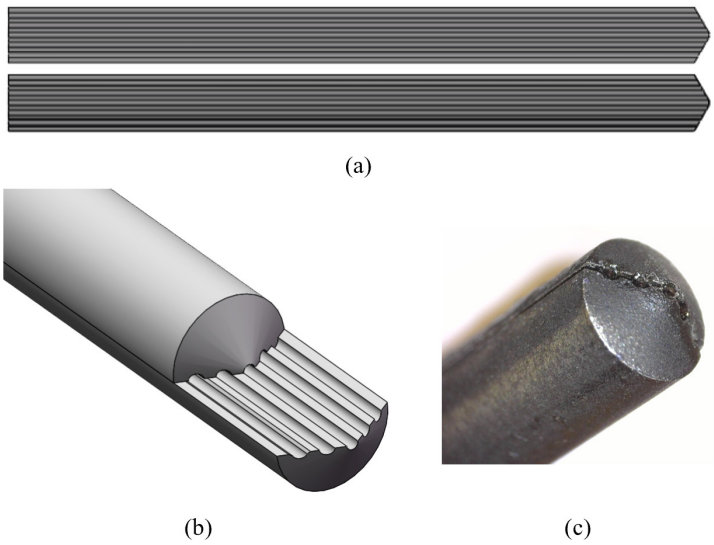

FIGURE 6.3: a-b Illustration of the custom-designed optical probe with a tip of $\alpha = 30^\circ$ and space for two pairs of parallel optical fibers. c Close-up view of the assembled probe tip.

RESULTS

MONTE CARLO SIMULATIONS

Figures 6.4a,b show the normalized fluence rate (the accumulated energy deposited into the voxels as photon packets propagate through the simulation volume, normalized to the input power and divided by the absorption coefficient [14]) of collected photons, orthogonally projected onto the plane of the two fibers for the two tip designs, cone, and single bevel. The probed volume was approximated as the mean photon path ± 1 std, which corresponds to a volume comprising the paths followed by 68.3% of all detected photons. The optical probing depth was defined as the distance between the probe tip and the deepest point to which the probed volume extends, and is indicated in the graph for the blunt probe ($\alpha = 0^{\circ}$). To compare the optical probing depth that can be achieved, the projected normalized fluence rates for all tip angles α are plotted next to each other.

With the cone design (Figure 6.4a), the plot shows that light goes beyond the absorbing probe tip for $\alpha \leq 45^{\circ}$. For a tip angle of $\alpha = 15^{\circ}$, the optical probing depth is reduced to approximately 75% of that of the blunt probe. For a tip angle of $\alpha = 30^{\circ}$, the optical probing depth has halved. The MC simulations show that not only the optical probing depth but also the total photon count depends heavily on the tip angle, as shown in Figure 6.4c. For $\alpha = 30^{\circ}$, the extended absorbing cone-shaped tip attenuates the obtained signal to well below half the original signal. The total photon count for $\alpha > 30^{\circ}$ suggests that the SNR suffers significantly for sharper tips.

With the single-bevel design (Figure 6.4b), light goes beyond the probe tip for all tip angles. For a tip angle of $\alpha = 15^{\circ}$, the optical probing depth is reduced only slightly. For a tip angle of $\alpha = 30^{\circ}$, the optical probing depth is still approximately 75% of that of the blunt probe. The probed volume for $\alpha = 45^{\circ}$ suggests that photons still reach relatively deep into the tissue, although the total photon count also decreases for higher tip angles (see Figure 6.4d). While exhibiting the same decreasing trend in signal-to-noise ratio (SNR), unlike the results observed in the cone simulation, the signal obtained with the single-bevel design for $\alpha = 30^{\circ}$ experiences considerably less attenuation, remaining at approximately 2/3 of the

photon count acquired with the blunt probe. For very sharp tips ($\alpha > 45^{\circ}$), in turn, the total photon count reaches similarly low values as for the cone design.

PHANTOM EXPERIMENTS

Figure 6.5 compares typical reflectance spectra for approaching the interface of the two phantom layers $I(d_p, \lambda)$ acquired with the two different tip designs. The spectra are plotted relative to the reflectance spectrum $I_{\infty}(\lambda)$ acquired on the pure cancellous bone-mimicking phantom ($d_p \rightarrow \infty$) with the respective tip design, recreating a pedicle screw placement scenario where the surgeon first obtains a reference spectrum from cancellous bone. This reference spectrum is then used to monitor the rest of the procedure through continuous measurements, alerting the surgeon about deviations to prevent impending breaches. The spectra are further normalized to the maximal intensity observed at the interface of the two phantom layers $I_{o,max}$, and are plotted for a wavelength range from 1000 nm to 1400 nm because the greatest differences in the signal are to be expected here.

With both the cone design (Figure 6.5a) and the single-bevel design (Figure 6.5b), a gradual change in spectrum can be seen between the cancellous bone-mimicking layer (d_p = 2.5 mm, dark brown) and the cortical bone-mimicking layer (d_p = 0 mm, light beige). While both tip designs yield similar results close to the interface of the two layers ($d_p \leq 1.5$ mm), a clear difference between the cone design and the single-bevel design can be seen when first approaching the cortical layer (d_p = 2.25 mm and d_p = 2.0 mm). With the cone design, the corresponding lines are very close to the pure cancellous spectrum, whereas a clear change in intensity magnitude and shape of the spectrum can be observed for the single-bevel design. Between d_p = 2.0 mm and d_p = 1.5 mm distance to the interface of the two phantom layers, the spectral shape is similar for both designs, yet the intensity is still higher for the single-bevel design.

These findings are supported by the (non-normalized) intensities at λ_o = 1211 nm shown in Figures 6.5c,d. The difference in intensity between the cancellous and the cortical bone-mimicking layers is relatively small with the cone design, as Figure 6.5c shows. With the single-bevel

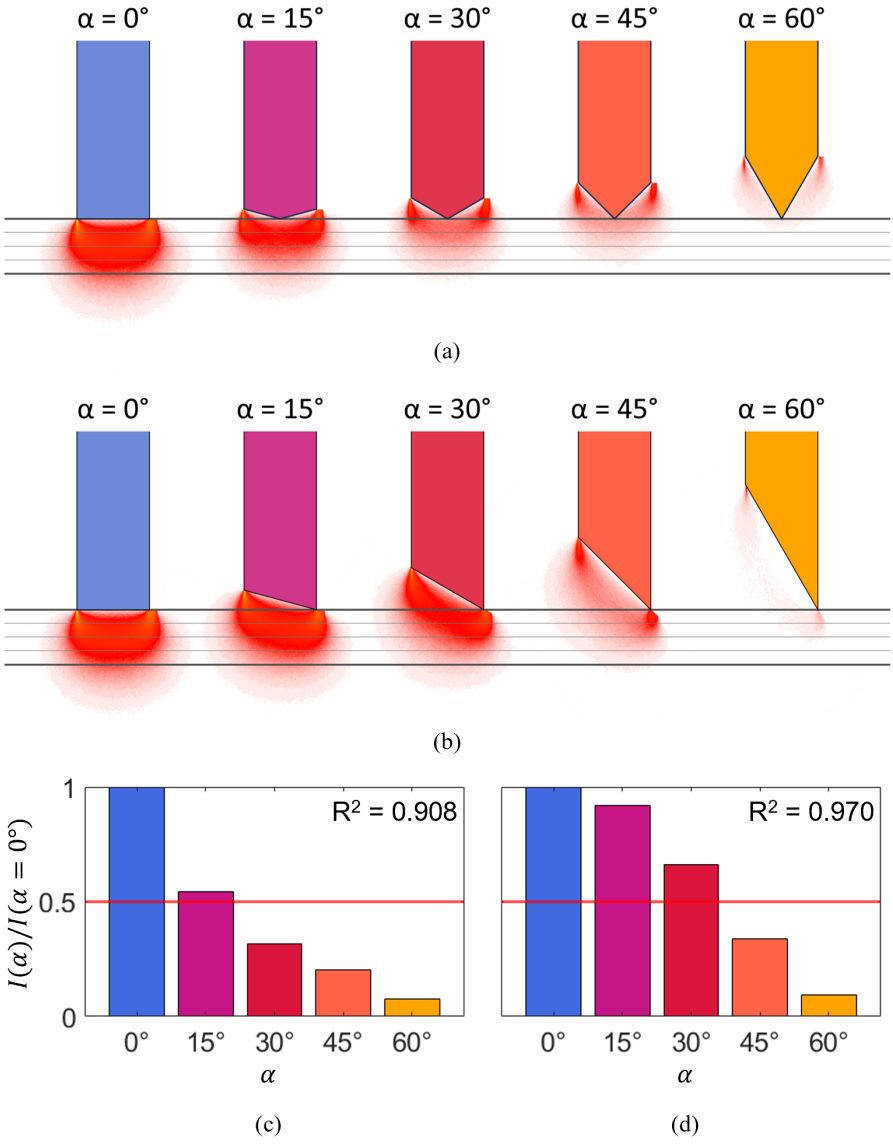

FIGURE 6.4: a-b Projected normalized fluence rate of collected photons for different tip angles for a the cone simulation, and b the single bevel simulation. The horizontal lines indicate the location of the probe tips and the optical probing depth of the blunt probe for reference. c-d Photon count for different tip angles relative to the photon count observed for α = 0° for c the cone simulation, and d the single-bevel simulation. Red line indicates half of the original photon count.

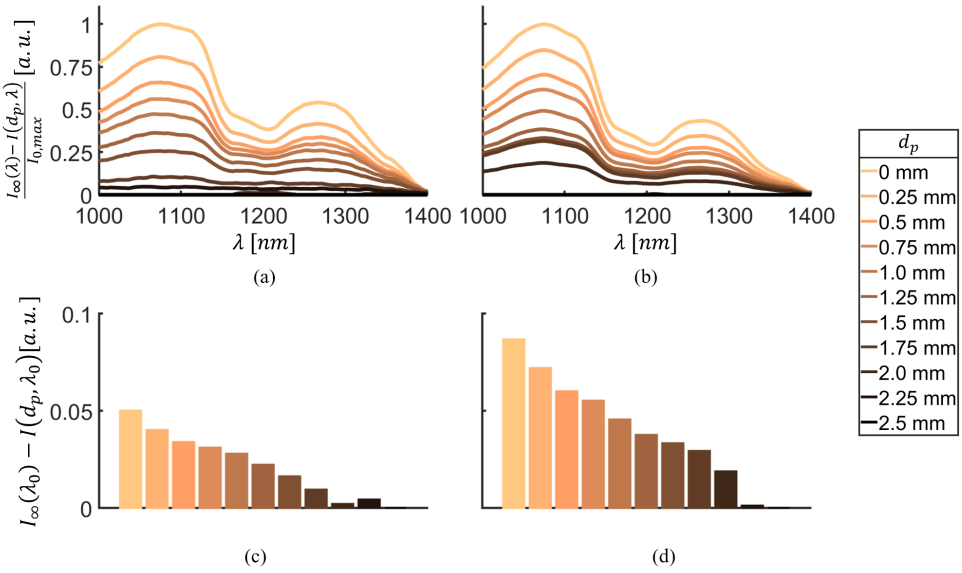

FIGURE 6.5: a-b Reflectance spectra for different distances to the interface relative to the reflectance spectrum of the pure cancellous bone-mimicking phantom, normalized to the maximal intensity of the pure cortical bone-mimicking phantom for a the cone design, and b the single-bevel design. c-d Intensity at λ_o = 1211 nm measured for different distances to the interface relative to the intensity at λ_o of the pure cancellous bone-mimicking phantom for c the cone design and d the single-bevel design.

design, the total difference in intensity between the two phantom layers is approximately double compared to the cone design, see Figure 6.5d.

DISCUSSION AND CONCLUSIONS

Pedicle cannulation requires a pedicle probe with a sharp tip; however, this tip shape poses a challenge for the incorporation of fiber optics as required for DRS. Next to investigating the influence of an extended cone-shaped tip on the optical signal, we therefore consider alternative designs that incorporate a single bevel where one fiber is offset along the device axis, in a protruded position relative to the other fiber. The MC simulation results show that light goes beyond the probe tip (optical probing depth > 0) with the cone design for tip angles up to 45° and with the single-bevel design for tip angles up to 60°. Still, the optical

probing depth decreases for sharper tip angles, as does the SNR. Optical probing depth and SNR seem to suffer more from the absorbing probe tip that extends between the two fibers in the cone design than they do from having one fiber protruded relative to the other fiber as in the single-bevel design.

From our simulation results, a tip angle of 30° seems to be the cut-off up to which reasonably good sensing results can be achieved with the single-bevel design, as it still allows for 75% of the original optical probing depth and 2/3 of the original signal strength. Therefore, we opted for this tip angle for our custom-designed probe, and made it accommodate both tip designs to allow for direct comparison.

The phantom experiments conducted with the custom-designed probe confirm our observations from the simulations that the single-bevel design outperforms the cone design. The difference in signal received between cancellous and cortical bone-mimicking phantom with the cone design was relatively low, supposedly for two reasons: due to the absorption happening at the extended tip, and because for high tip angles, light – following Fermat's principle – starts traveling around the tip instead of ahead, which alters the probed volume and reflects in the acquired spectrum. This is not the case when one of the fibers is protruded relative to the other fiber and placed at the tip of the pedicle probe. The difference in signal received between cancellous and cortical bone with the single-bevel design was therefore higher, suggesting that optical probing depth and SNR of this design allow for better detection of impending breaches. This is supported by the changes in magnitude and shape of the spectral lines when first approaching the cortical layer. As photons start to travel through both media, absorption and scattering properties change. The first signal changes are visible earlier for the single-bevel design, indicating that this design allows to detect cortical breaches well before they occur.

Two possible pedicle probe designs that arise from these insights are (1) an actual single bevel tip with a diameter of at least the fiber distance, or (2) a cone-shaped tip with a diameter of at least twice the fiber distance that houses one fiber in the tip. The latter would even allow for symmetric designs with a multitude of emitting fibers located around a single

collector inside the pedicle probe tip, allowing to further increase the SNR.

An optical pedicle probe can provide surgeons with real-time information on the bone composition inside the vertebra beyond tactile feedback alone. Dynamically redirecting the probe enables exploration of longer trajectories without breaching the cortical boundary, allowing for the insertion of screws with optimal dimensions for superior biomechanical strength, a critical advantage in compromised bone conditions like osteoporosis.

LIMITATIONS

This study's primary limitation is the assumption that the extended tip is fully absorbing. This assumption affects the results for the cone design, where we would expect higher optical probing depth and SNR for a reflecting tip compared to an absorbing tip. In contrast, the optical properties of the tip appear to have limited impact on the single bevel tip's performance, with little change in the probed volume up to tip angles of 30°. An absorbing probe tip represents the most challenging scenario, indicating that while the cone design is less effective with an absorbing tip, it may still function with a reflecting one. The single-bevel design remains effective for both a reflective and an absorbing tip.

Our study focused on two specific designs for probe tips, the cone and the single bevel. However, the spectrum of possible designs extends beyond these two options. We did not explore probe tips where one fiber is placed on the opposite side of the cone, but closer to the tip (so still protruded relative to the other fiber). While we anticipate such a design to yield results intermediate to the two extremes tested here, it merits further investigation to prove how much light is absorbed at the extended tip, and to what extent light travels around the tip instead of ahead. Although this design cannot compete with the single-bevel design in terms of signal strength and optical probing depth, placing the protruded fiber off of the tip can save some space in diameter if a cone-shaped tip is desired.

We also did not investigate the impact on the optical signal of rounding off the tip of a cone-shaped pedicle probe. Nevertheless, we expect the effect of such a modification to be minor compared to the substantial

effect that the single-bevel design can make, in addition to the impairment that a round tip poses for the pedicle probe's performance.

In this study, we investigated which would be the best pedicle probe from a sensing point of view, but the design of a pedicle probe is primarily dependent on mechanical and surgical factors (*e.g.*, the vertebral level operated on, the condition of the bone tissue in connection with age-related changes and the presence of osteoporosis, and the personal preference of the surgeon). These factors collectively determine the optimal design and must be taken into consideration before the final pedicle probe can be developed to actually promote the integration of DRS into the surgical workflow.

CONCLUSIONS

DRS could enhance spine surgery by allowing to detect impending cortical breaches. The aim of this study was to investigate the impact of the tip shape of a pedicle probe on the DRS signal. With our results from MC simulations and optical phantom experiments, we demonstrate that a single bevel with an angle of 30° is superior to a cone-shaped tip for detecting proximity to the cortical layer. These findings pave the way for future integration of DRS technology into surgical instruments for improved pedicle screw placement accuracy.

REFERENCES

1. Weinstein, Stuart L., et al. "Adolescent idiopathic scoliosis." The lancet 371.9623 (2008): 1527-1537.
2. Deyo, Richard A., et al. "United States trends in lumbar fusion surgery for degenerative conditions." Spine 30.12 (2005): 1441-1445.
3. Deyo, Richard A., and Sohail K. Mirza. "Trends and variations in the use of spine surgery." Clinical Orthopaedics and Related Research (1976-2007) 443 (2006): 139-146.
4. Dick, Walter, et al. "A new device for internal fixation of thoracolumbar and lumbar spine fractures: the 'fixateur interne'." Spinal Cord 23.4 (1985): 225-232.
5. Siddall, Philip J., and John D. Loeser. "Pain following spinal cord injury." Spinal cord 39.2 (2001): 63-73.
6. Roberts, Timothy T., et al. "Classifications in brief: American spinal injury association (ASIA) impairment scale." (2017): 1499-1504.
7. Kosmopoulos, Victor, and Constantin Schizas. "Pedicle screw placement accuracy: a meta-analysis." Spine 32.3 (2007): E111-E120.
8. Perdomo-Pantoja, Alexander, et al. "Accuracy of current techniques for placement of pedicle screws in the spine: a comprehensive systematic review and meta-analysis of 51,161 screws." World neurosurgery 126 (2019): 664-678.
9. Burström, Gustav, et al. "Diffuse reflectance spectroscopy accurately identifies the pre-cortical zone to avoid impending pedicle screw breach in spinal fixation surgery." Biomedical optics express 10.11 (2019): 5905-5920.
10. Swamy, Akash, et al. "Diffuse reflectance spectroscopy, a potential optical sensing technology for the detection of cortical breaches during spinal screw placement." Journal of biomedical optics 24.1 (2019): 017002-017002.

11. Losch, Merle S., et al. "Diffuse reflectance spectroscopy of the spine: improved breach detection with angulated fibers." Biomedical Optics Express 14.2 (2023): 739-750.

12. Fisher, Michael A. "Smart pedicle tool." US patent US 8249696 B2 (2007)

13. Fisher, Carl, et al. "Perspective on the integration of optical sensing into orthopedic surgical devices." Journal of Biomedical Optics 27.1 (2022): 010601.

14. Marti, Dominik, et al. "MCmatlab: an open-source, user-friendly, MATLAB-integrated three-dimensional Monte Carlo light transport solver with heat diffusion and tissue damage." Journal of biomedical optics 23.12 (2018): 121622-121622.

15. Nachabé, Rami, et al. "Estimation of lipid and water concentrations in scattering media with diffuse optical spectroscopy from 900 to 1600 nm." Journal of biomedical optics 15.3 (2010): 037015-037015.

7

Chapter 7
A handheld DRS setup for spine surgery

accepted for publication as
Losch, M. S., Visser, B. E., Dankelman, J., & Hendriks, B. H. (2024). A handheld fiber-optic tissue sensing device for spine surgery. *PLoS One*.

data available at
doi.org/10.4121/77363d00-f68c-4da7-b32e-3aabe957ef98.

ABSTRACT

The demographic shift has increased the demand for surgical interventions to address age-related degenerative diseases, such as spinal fusion. Accurate placement of pedicle screws, crucial for successful spinal fusion, varies widely with physician experience. Integrating tissue sensing into spine surgical instruments allows intraoperative examination of tissue properties, providing surgeons with additional information to prevent screw misplacement. This paper introduces a handheld fiber-optic tissue sensing device for real-time bone tissue differentiation during spine surgery using Diffuse Reflectance Spectroscopy (DRS).

Our prototype employs laser diodes at two distinct wavelengths for tissue illumination, eliminating the need for a spectrometer and enabling direct light collection with a photodiode. The device includes a printed circuit board (PCB) with driver circuits that are adjustable for varying laser diode output power, and signal amplification to convert the photodiode current to a measurable voltage signal. Controlled by a microcontroller, the device computes a reflectance ratio from both laser diode signals to provide real-time audio feedback to surgeons across various healthcare settings.

Despite challenges in coupling efficiencies from manual fiber-coupling of the diodes, our prototype is able to emit and collect light to distinguish bone tissues with DRS, demonstrating feasibility. It is compact, made of low-cost and readily available components, and offers fast, real-time feedback, thus serving as a successful proof-of-concept for enhancing surgical accuracy during spinal fusion procedures.

INTRODUCTION

Over the past decades, the world has witnessed a demographic shift towards increased life expectancy, accompanied by a growing need for surgical interventions to address age-related degenerative diseases [1, 2]. Among these interventions, spinal fusion is an option for patients seeking relief from debilitating spinal conditions. Central to the success of spinal fusion procedures is the accurate placement of pedicle screws, which provide stability to the spine during the fusion process [3]. Despite the emphasis on achieving surgical accuracy to avoid complications and revision surgeries, accurate screw placement remains a challenge due to the complex anatomy of the spine and the reliance on tactile feedback and anatomical expertise [4, 5].

Misplacement of pedicle screws can lead to severe complications including neurological injury, and the need for revision surgery [6]. To enhance the accuracy of screw placement, various guidance systems such as intraoperative fluoroscopy, computer-assisted navigation, and robotic assistance have been developed [7]. While these technologies have shown great promise in improving accuracy, they come with drawbacks including high costs, the need for specialized training, and limitations in availability [8-10].

Intra-operative ultrasonography is cost-effective and provides real-time imaging within a portable device. However, ultrasound has limitations in visualizing bony structures due to poor penetration through dense tissue and low signal-to-noise ratio (SNR), and its efficacy still largely depends on the operator's expertise [11, 12]. These limitations underscore the need for alternative approaches that offer more direct, consistent, and interpretable feedback during spine surgery.

Integrating tissue sensing into surgical instruments presents a promising alternative for improving the accuracy of pedicle screw placement. By examining the physical properties of surrounding tissue in real-time, tissue sensing devices offer valuable feedback to surgeons, allowing them to adjust screw trajectories and prevent misplacement. While the PediGuard system (Spine-Guard SA, Vincennes, France) has pioneered tissue sensing in spine surgery using Electrical Impedance Spectroscopy (EIS), it faces

challenges such as susceptibility to blood and tissue accumulation in the pilot hole [13, 14]. Additionally, as the device only measures tissue in direct contact with its tip, a cortical breach can only be identified once the breach is already in progress, limiting the opportunity for early intervention [13, 15]. Given these limitations, Diffuse Reflectance Spectroscopy (DRS) emerges as a compelling alternative.

DRS operates on the principle of light interaction with tissue to assess its composition. A spectrum of light is directed into tissue via optical fibers, inducing scattering and absorption processes that vary according to the tissue's structure and biochemical composition. The light that is reflected back carries information about the tissue's optical properties. Studies have demonstrated the effectiveness of DRS in distinguishing between cancellous and cortical bone based on fat content, thereby providing reliable feedback for pedicle screw placement [16, 17] This technology offers real-time feedback and the potential for integration into existing surgical devices through fiber-optic technology [18-22]. DRS enables early breach detection and remains unaffected by blood interference when using near-infrared (NIR) wavelengths [23, 24]. However, current DRS systems suffer from cumbersome and expensive setups which at present limit their application in the operating room.

In this paper, we present a handheld fiber-optic tissue sensing device for spine surgery. Unlike traditional DRS systems, our device uses only two distinct wavelengths instead of broadband light for illumination. This eliminates the need for the spectrometer typically used in DRS systems to separate the spectrum of the collected light, as light can be collected directly by a simple photodetector, making our system compact and affordable. Controlled by a microcontroller, our device provides real-time audio feedback to surgeons. Through this novel design, we aim to democratize the availability of tissue sensing technology, making it accessible to a wider range of healthcare practitioners and facilities.

SYSTEM COMPONENTS AND DESIGN

The design of the handheld fiber-optic tissue sensing device was driven by three main considerations:

(1) **size:** The components must be compact to accommodate placement within a handheld device.

(2) **cost:** The components must be readily available off-the-shelf or easily manufactured to ensure the device's affordability.

(3) **speed:** The sensing device must provide real-time tissue feedback based on DRS measurements.

All components – a light source, a photodetector, the electronic circuits, a microcontroller, the feedback system, and the casing – were selected and designed with these three criteria in mind.

LIGHT SOURCE

DR spectra vary based on the measured tissue's structure and composition. To extract biologically relevant information, the collected spectrum can be compared against absorption spectra of key chromophores, such as collagen, lipids, and water. While DRS typically employs a broadband light source for tissue illumination, we opted for just two wavelengths. By specifically selecting wavelengths where cancellous and cortical bone tissues show significant differences in optical properties, we can effectively distinguish between them based on the ratio of their signals, avoiding wavelengths dominated by hemoglobin or water absorption, which could hinder tissue differentiation.

Previous studies have identified optimal wavelengths for bone tissue differentiation in DRS measurements [16, 18, 25-28]. For distinguishing cortical bone from other tissues, four wavelength regions within the visible/NIR spectrum were identified: 695-699 nm, 925-927 nm, 1188 nm, and 1207-1211 nm [29].

As light-emitting diodes (LEDs) typically have low power output, laser diodes were chosen as the light source due to their higher focused output power and narrow emission spectrum (5-20 nm). To meet size and cost constraints, we selected simple TO-can laser diodes over fiber-coupled ones, which are readily available off-the-shelf and offer a wide range of wavelength options in a typical compact 5.6 mm TO-can packaging. Considering cost-effectiveness and time efficiency, we avoided custom-

ordering laser diodes and selected available wavelengths, including 690 nm, 905 nm, 940 nm, and 1270 nm. Additionally, 1310 nm was chosen as a reference wavelength with similar absorption in both cancellous and cortical bone. These wavelengths were input for Monte Carlo (MC) simulations in MCmatlab [30] to model light scattering and absorption within the bone tissue. The simulation results revealed the largest difference between cancellous and cortical bone in the intensities collected at 940 nm and 1310 nm, leading to their selection as the light sources for our device.

The chosen laser diodes, operating at 940 nm (QL94J6SA, Roithner Lasertechnik GmbH, Vienna, Austria) and 1310 nm (RLT1310-5MGS-P2, Roithner Lasertechnik GmbH, Vienna, Austria), Figure 7.1 (1), were selected based on their power ratings of 50 mW and 11 mW respectively. Both diodes provide sufficient power for a good SNR on tissue samples and are deemed safe for continuous illumination [31, 32].

To integrate DRS into a thin probe, we utilize 400 µm core diameter optical fibers with a numerical aperture (NA) of 0.22 (FG400LEA, Thorlabs Inc., Newton (NJ), USA). The laser diodes are coupled to the optical fibers using NIR-transparent optical adhesive (NOA81, Norland Products Inc., Jamesburg (NJ), USA).

DRIVER CIRCUIT

The two laser diodes are powered by electronic driver circuits that ensure constant output power. Automated power control (APC) circuitry enhances reliability and consistency, particularly in applications requiring precise power levels over extended durations, by stabilizing output and compensating for environmental variations. The TO-can packaging of the laser diodes used as the light source incorporates a photodiode to enable feedback control of the laser's output power. This photodiode generates a photocurrent proportional to the laser diode's emission, facilitating the monitoring of laser power.

To achieve APC of the laser diodes, driver integrated circuits (ICs) (iC-WJ SO8, iC-Haus, Bodenheim, Germany) are employed. These ICs are designed for the N-type built-in configuration of the laser diodes and can operate in constant or pulsed mode up to 300 kHz. The IC sets the desired

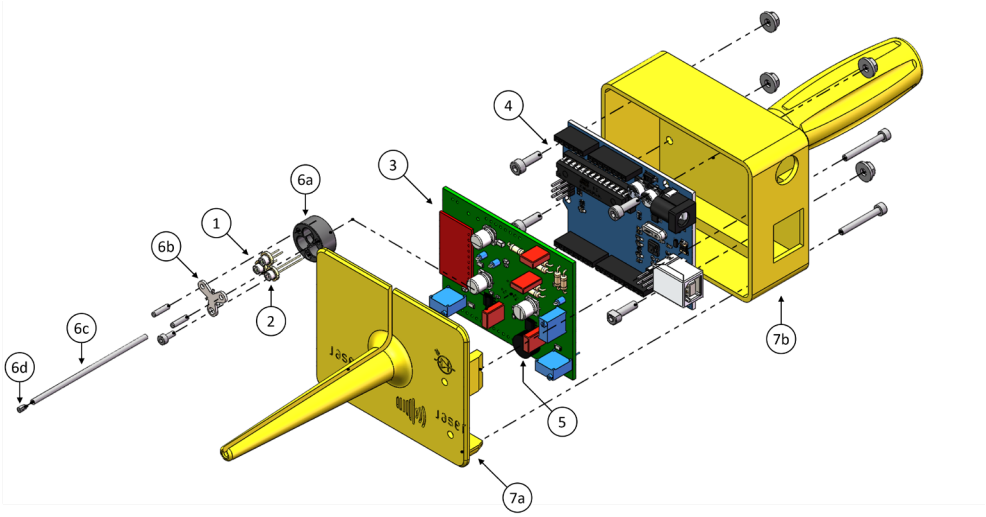

FIGURE 7.1: Exploded view of handheld fiber-optic tissue sensing device including two laser diodes (1), one photodiode (2), a PCB (3), an Arduino (4), a buzzer (5), a diode holder unit (6a-d), and a two-part housing (7a+b). The corresponding CAD files can be found at Ref. [60].

output through external resistors and capacitors. The schematic of the dynamic driver circuit is depicted in Figure 7.2.

The average optical output power, determined by the monitor current amplitude I_{av}(AMD), is set by adjusting R_{SET} (potentiometer ranging up to 25 kΩ), with R_{SET2} = 2.7 kΩ serving as the minimum value within this control range:

$$R_{SET} + R_{SET2} = \frac{CR \cdot V(\mathrm{ISET})}{I_{av}(\mathrm{AMD})} \quad [\Omega] \ (1)$$

The IC specifies a current ratio CR of 1 and a constant voltage V(ISET) of 1.22V as its electrical characteristics. The expected monitor currents under continuous mode are 0.2 mA for the 940 nm laser diode and 0.3 mA for the 1310 nm laser diode. Operating the laser diodes with a pulse duty factor of 50% yields R_{SET} values of 9.5 kΩ for 940 nm and 5.4 kΩ for 1310 nm.

To smooth out the control, a capacitor C_1 is employed. This prevents peak values from reaching the laser diode during pulse control, reducing the risk of damage. According to the IC's specifications, capacitor C_1 can be set to 100 nF in constant mode, while maintaining input pin IN at 5V. For pulse

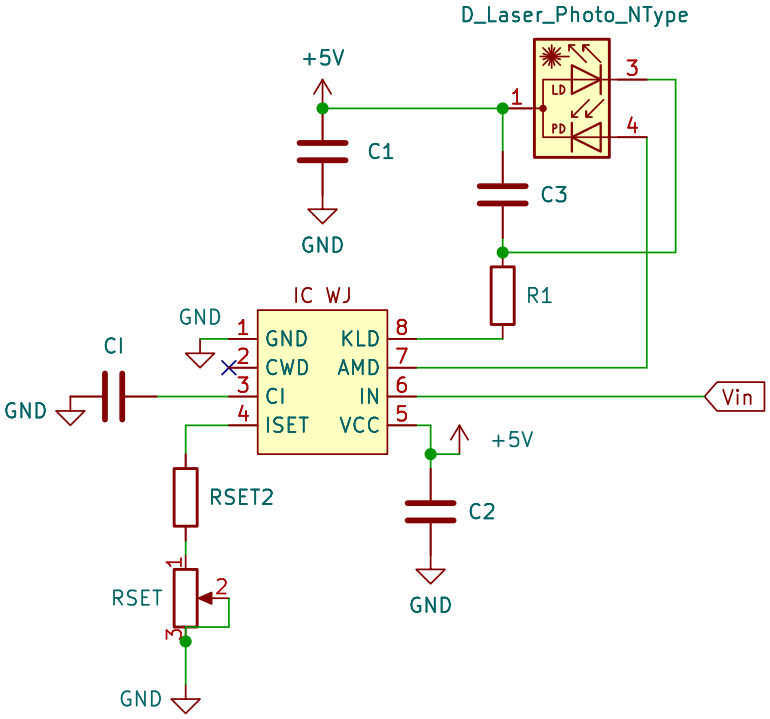

FIGURE 7.2: Schematic of the dynamic driver circuit for N-type laser diodes.

mode operation, input pin IN can be alternated between 0V and 5V at the desired frequency. As specified by the manufacturer, the capacitor's value should be increased with slower pulse repetition frequency f or larger monitor current to accommodate the larger charge buildup:

$$CI \geq \frac{440 \cdot I(\mathrm{ISET})}{f \cdot V(\mathrm{ISET})} = \frac{440}{f \cdot (R_{SET} + R_{SET2})}. \qquad \text{[F] (2)}$$

Additionally, capacitors C_1 = 100 µF and C_2 = 0.1 µF serve to stabilize the power supply, preventing voltage fluctuations for increased reliability. Capacitor C_3 = 2 nF protects the laser diode from electrostatic discharge or transients that could cause damage. Finally, series resistor R_1 = 12 Ω reduces the total power consumption of the IC by limiting current and damping oscillations from the power supply.

PHOTODETECTOR

DRS relies on reflectance-based measurements, requiring that the light source and photodetector be placed side by side for *in-vivo* probing. The

source-detector separation (SDS) is set at 1.3 mm to ensure sufficient look-ahead distance into the bone tissue while maintaining a compact setup and reasonable light attenuation in the tissue [16, 23].

The reflected light from the bone tissue can be directly measured by a photodiode. When illuminated by light, a photodiode generates an electric current. The output current I_{PD} of the photodiode is proportional to the optical power P_{in} incident on its surface. To ensure a linear relationship between optical power and output current, the photodiode operates in photoconductive mode (reverse-biased) rather than photovoltaic mode (zero bias). This choice increases the responsivity while possibly leading to a higher dark current due to the widened depletion junction. The photodiode current comprises both the signal current and the offset dark current.

The photodiode selected for our device is a wide spectral range InGaAs photodiode (IG17X500S4ix, Laser Components Germany GmbH, Olching, Germany), Figure 7.1 (2), which we fiber-coupled in the same way as the aforementioned laser diodes. It exhibits varying responsivity R_{PD} across the wavelength spectrum (500-1700 nm), with a peak responsivity of 1.05 A W^{-1} observed around 1550 nm.

EXPECTED SIGNAL

Using the wavelength-specific responsivity of the photodiode R_{PD} (λ), the photodiode current is determined as follows:

$$I_{PD} = P_{in} \cdot R_{PD}(\lambda) \ . \qquad \text{[A] (3)}$$

The incident optical power P_{in} on the photodiode surface is calculated as:

$$P_{in} = P_{LD} \cdot \eta_{LD} \cdot R_{tissue}(\lambda) \cdot \eta_{PD} \ , \qquad \text{[W] (4)}$$

where P_{LD} represents the emitted power of the laser diode, η_{LD} denotes the laser-diode-to-light-guide coupling efficiency, R_{tissue} (λ) refers to the percentage of emitted photons at a specific wavelength λ that reach the collecting fiber after interaction with the tissue, and η_{PD} denotes the light-guide-to-photodiode coupling efficiency. Table 7.1 gives an overview of the expected values for all parameters influencing the photodiode current.

The driver circuits were designed to emit light at a power of 51.1 mW for the 940 nm laser diode and 10.3 mW for the 1310 nm laser diode. Some of this light is lost due to butt-coupling, the process of bonding the diode to the fiber end with optical adhesive. Butt-coupling typically achieves a maximum efficiency of 50% [33-35]. We conservatively estimated the laser- and photodiode coupling efficiencies at 30% each.

Since the incident optical power is dependent on tissue reflection, the fractions of collected photons (expressed as permille) for cancellous (R_{canc}) and cortical bone (R_{cort}) at 940 nm and 1310 nm were estimated through MC simulations of our setup. With emitter and collector simulated as optical fibers (core diameter 400 µm, NA = 0.22) at SDS = 1.3 mm, we simulated 10^9 photons of a wavelength of 940 nm and 1310 nm each within either a single-layer cancellous bone model (μ_a (940 nm) = 0.216, μ'_s (940 nm) = 28.6, μ_a (1310 nm) = 0.833, μ'_s (1310 nm) = 17.3, g = 0.9 [16]) or a single-layer cortical bone model (μ_a (940 nm) = 0.223, μ'_s (940 nm) = 16.4, μ_a (1310 nm) = 0.920, μ'_s (1310 nm) = 11.3, g = 0.9 [16]) with the dimensions 3.0 mm x 3.0 mm x 3.0 mm and a resolution of 100 bins/mm (simulation run for 300 x 300 x 300 voxels) using MCMatlab [30]. The obtained reflectance values are ranging around 0.1‰-0.15‰ as listed in Table 7.1.

Photodiode responsivity is found in the datasheet as 0.62 A W^{-1} at 940 nm and 0.91 A W^{-1} at 1310 nm. Considering our estimation and the equations presented above, a projected photocurrent ranging from 81 nA to 432 nA is anticipated.

TABLE 7.1: Parameters affecting I_{PD}.

	940 nm	1310 nm
P_{LD} [mW]	51.1	10.3
η_{LD} [%]	30	30
η_{PD} [%]	30	30
R_{canc} [‰]	0.152	0.120
R_{cort} [‰]	0.149	0.0955
R_{PD} [A W^{-1}]	0.62	0.91

SIGNAL AMPLIFICATION

Given the anticipated low levels of the photodiode current, a transimpedance amplifier (TIA) is necessary to amplify these currents into measurable voltage signals V_{out} for further processing. The estimated maximum photodiode current plays a critical role in determining the gain G of the TIA:

$$V_{out} = I_{PD} \cdot G\,. \qquad \text{[V] (5)}$$

The chosen operational amplifier (op-amp) (MAX44263AXA+T, Analog Devices Inc., Wilmington (MA), USA) was selected for its low bias current, offset voltage, power consumption, and input capacitance, along with a large gain-bandwidth product (GBP). Its rail-to-rail input/outputs maximize dynamic range for precise analog-to-digital converter (ADC) readouts. The op-amp comes in a dual SC70 package enabling a two-stage design to mitigate the impact of a single large feedback resistor R_F, which can introduce parasitic capacitance and increase noise contribution.

The first stage acts as a transimpedance amplifier with a gain of up to 5 MV A^{-1}, while the second stage functions as an inverting amplifier with a gain of 10 V V^{-1}, potentially resulting in a cumulative transimpedance gain of 50 MV A^{-1}. The schematic of the amplifier circuit is depicted in Figure 7.3.

The op-amp operates on a single 5V direct current (DC) power supply (V_{supply}) with two stabilizing capacitors C_4 = 0.1 µF and C_5 = 1 µF in parallel that filter noise, stabilize voltage fluctuations, and provide localized energy reservoirs to ensure stable and reliable operation of the TIA by minimizing ground bounce and preventing parasitic oscillations that could affect the output.

To establish a linear dynamic range and prevent saturation at the negative power supply in the absence of photocurrent, a bias of 2.7V is selected for the non-inverting inputs. This bias voltage serves a dual purpose: it facilitates an inverting amplifier stage crucial for single power supply operation where negative voltage swing cannot be achieved, and it establishes a virtual ground reference point, determining the maximum voltage swing of the TIA.

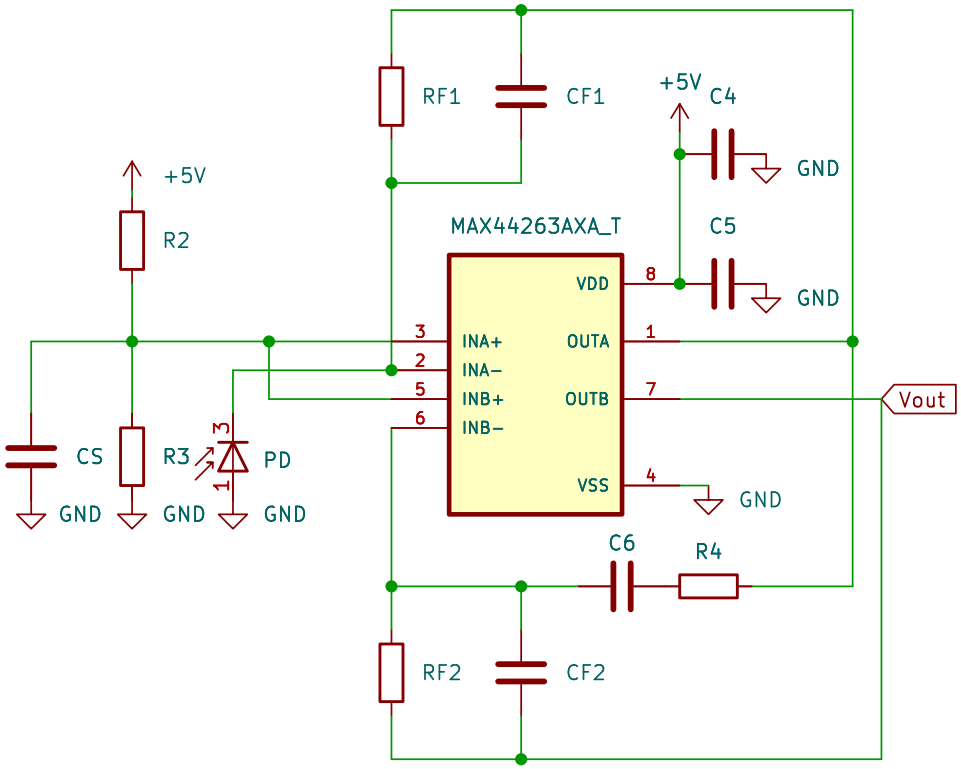

FIGURE 7.3: Schematic of the two-stage, low-noise transimpedance amplifier circuit.

Single-supply op-amps with a midway bias voltage ensure efficient operation within their specified parameters. While a higher bias voltage might offer a larger inverting range and potential for greater amplification, it could also increase noise levels and cause earlier saturation for larger signals.

The power supply voltage and the bias voltage for photoconductive mode collectively determine the amplifier's effective operating range:

$$0V \leq V_{out} + V_{bias} \leq V_{supply} \,. \qquad \text{[V] (6)}$$

Achieving this operating range involves utilizing a voltage divider consisting of resistors R_2 = 22 kΩ and R_3 = 27 kΩ. To mitigate noise from the voltage divider and power supply, a capacitor C_S is added in parallel with resistor R_3. With a value of 1 µF, this capacitor establishes a corner frequency f_b (-3 dB) per Eq. (7), eliminating frequency noise above 13 Hz:

$$f_b = \frac{1}{2\pi \cdot R_2 \parallel R_3 \cdot C_S}. \quad \text{[Hz] (7)}$$

The electrical behavior of the photodiode under zero bias is represented by a current source and a junction capacitance C_j of 60 pF as specified by the manufacturer. This inherent capacitance contributes to instability and noise in the amplifier. To counteract this effect and minimize high-frequency noise at the op-amp output, feedback capacitors C_F are introduced. The initial feedback capacitor C_{F1} compensates for both the photodiode's junction capacitance and the op-amp's input capacitance and is set to 6.8 pF. The feedback resistor R_{F1}, a potentiometer ranging up to 5 MΩ, is initially set at its maximum value, resulting in a bandwidth (-3 dB) of at least 4.68 kHz:

$$f_{-3dB} = \frac{1}{2\pi \cdot R_F \cdot C_F}. \quad \text{[Hz] (8)}$$

With an estimated maximum photocurrent of 432 nA, the amplifier configuration provides ample headroom: to ensure that the cumulative transimpedance gain is sufficient even for small incident powers and map the obtained output voltage of the photodiode V_{out} with a bias voltage of 2.7V, a total gain of 6 MV A^{-1} is sufficient according to Eq. (5). With a set gain of G_2 = 10 V V^{-1} for the second amplifier stage, a gain of G_1 = 600 kV A^{-1} (R_{F1} = 600 kΩ) is needed for the first stage. As the value of R_{F1} is reduced, the bandwidth of the circuit increases. Alternatively, the feedback capacitor can be exchanged for a larger capacitor.

Notably, a substantial portion of the gain is allocated to the initial transimpedance stage. The noise contribution from the second amplifier stage is relatively lower compared to the first stage. To minimize high-frequency noise in the second stage, another 6.8 pF capacitor C_{F2} is introduced in parallel with resistor R_{F2} to roll-off high-frequency gain. Since the cumulative transimpedance gain is the product of R_{F1} and R_{F2} divided by R_4, R_{F2} is chosen as 470 kΩ, resulting in a bandwidth of 50 kHz according to Eq. (8). Consequently, R_4 is set to 47 kΩ.

Due to the high gain of the amplifiers, an output coupling capacitor C_6 = 10 µF is required, placed in series with the output of the first op-amp.

This capacitor blocks DC voltages and allows only alternating current (AC) signals to pass, ensuring that steady-state signals such as ambient light or constant offsets from electrical components are not amplified. Only the pulsating signals from the illuminated tissue are processed. This capacitor, in conjunction with the resistor, creates a time constant τ due to the RC behavior of the circuit:

$$\tau = R \cdot C. \qquad \text{[s] (9)}$$

The parameter τ corresponds to the time it takes for the capacitor to charge to approximately 63% of its maximum voltage. In our setup, a large time constant of τ = 0.47 s results. This ensures an almost flat pulse response, as the slow charging of the capacitor smooths out rapid voltage changes. However, when the circuit is first turned on, the capacitor C_6 takes about two seconds to charge to the bias voltage and establish equilibrium (Figure 7.4a). During this initial charging period, false voltages may be outputted. This phenomenon is referred to as the capacitor's settling time or initialization phase [36].

The AC coupling introduced may affect both the frequency response and transient behavior of the circuit. In cases where the gain of the second-stage op-amp is low, this capacitor may be bypassed, given that the amplification of offset and noise is insignificant.

We simulated the transient response of the TIA in Micro-Cap 12 (Spectrum Software, Sunnyvale (CA), USA) to verify its operational principle. For the simulation, two alternating square wave signals with an amplitude of 432 nA (photodiode current estimated for 940 nm on cancellous bone) and 101 nA (photodiode current estimated for 1310 nm on cancellous bone), a frequency of 500 Hz, and 50% duty cycle each are generated to test the amplifier's time response. The simulated response for both op-amp stages is illustrated in Figure 7.4.

For a first amplifier stage gain of 600 kV A^{-1}, the difference in input signal ΔI_{PD} leads to a peak-to-peak voltage of

$$\Delta V_{out,1} = \Delta I_{PD} \cdot G_1 = 198.6\ \text{mV}.$$

The second stage is an inverter and amplifies the signal towards ground, resulting in a peak-to-peak voltage of

$$\Delta V_{out} = \Delta V_{out,1} \cdot G_2 = 1.986\ \text{V}.$$

The output voltage is fluctuating around the bias voltage of 2.7V, yielding outputs of V_{out} = 3.693V and V_{out} = 1.707V as visualized in Figure 7.4b.

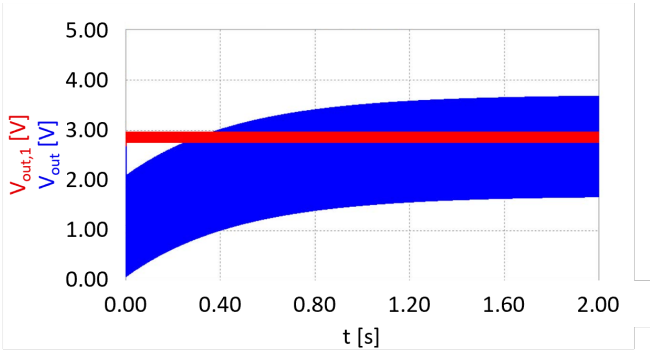

(a)

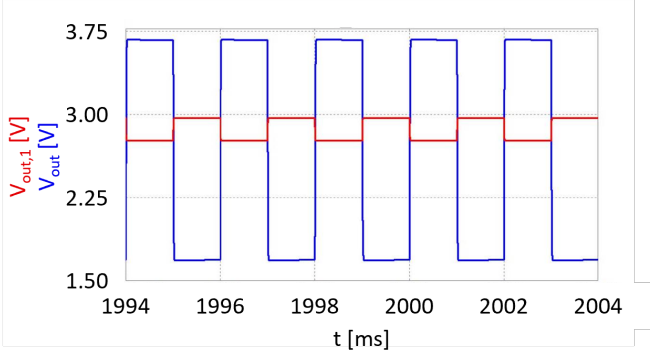

(b)

FIGURE 7.4: Response simulation of the two-stage, low-noise transimpedance amplifier circuit with 2.7V bias for two alternating square wave signal inputs with amplitudes of 432 nA and 101 nA, a frequency of 500 Hz, and 50% duty cycle each. The output voltage after the first stage (G_1 = 600 kV A^{-1}) is illustrated in red; the output voltage after the second stage (G_2 = 10 V V^{-1}) is illustrated in blue. a Simulation over the first two seconds showing the system's initial behavior. The settling time of the output capacitor C_6 is evident from the increasing output voltage over time, reaching equilibrium at the bias voltage. b Simulation showing the system's steady-state behavior. Peak-to-peak voltages are $\Delta V_{out,1}$ = 198.6 mV and ΔV_{out} = 1.986 V, fluctuating around the bias voltage of 2.7V.

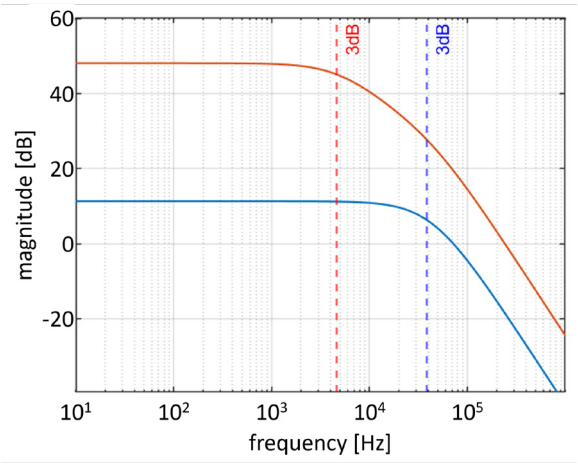

FIGURE 7.5: Frequency response simulation of the two-stage, low-noise transimpedance amplifier circuit, indicating a bandwidth of 4.68 kHz for a total gain of 50 MV A^{-1} (red) and a bandwidth of 39 kHz for a total gain of 6 MV A^{-1} (blue).

The simulated frequency response of the amplifier is shown in Figure 7.5, where the amplitude of the test input signal is swept from 10 Hz to 1 MHz. For a total gain of 50 MV A^{-1} (G_1 = 5 MV A^{-1}), the bandwidth is limited to 4.68 kHz by the first amplifier stage (red curve); for a total gain of 6 MV A^{-1} (G_1 = 600 kV A^{-1}), the bandwidth is limited to 39 kHz by the first amplifier stage (blue curve).

ELECTRONICS

The electonics comprise the driver circuits for the laser diodes and the signal amplification of the detected photodiode current, implemented on a double-sided printed circuit board (PCB), Figure 7.1 (3), designed using KiCad 7.0 software, available at https://www.kicad.org/. The PCB is constructed from FR4 material with a thickness of 1.6 mm, and finished using the common and cost-effective hot air solder leveling (HASL) process with lead technology.

The PCB features varying tracing widths based on component requirements. Notably, the dual SC70 op-amp package necessitates a 0.3 mm tracing width due to its small pin spacing, while the 5V supply line employs a wider 0.5 mm width. All other traces are set at 0.4 mm.

The layout of the PCB prioritizes efficient design. Laser diodes and the photodiode are centrally positioned to facilitate optical fiber coupling without excessive bending. Nearby placement of related components minimizes potential tracing issues. To optimize op-amp performance, the ground pour around the op-amp area is removed, reducing parasitic capacitance to the inverting inputs.

To meet size constraints, most components are surface-mount devices (SMDs), chosen for their compact packaging. However, for greater flexibility during prototyping, several components including feedback resistors, capacitors, bias voltage elements, the integrator capacitor, and potentiometers, are designated as through-hole rather than SMD, facilitating easy replacement if needed. A front and backside view of the PCB can be seen in Figure 7.6 with the corresponding PCB schematic found at Ref. [60].

The system can be powered via a USB supply from a connected laptop or similar device. Alternatively, a screw terminal labeled J_1, equipped with a bypass capacitor, allows connection to alternative power sources. Strategically placed test points (TP_1, TP_2, TP_3) facilitate measurements of bias voltage and amplifier output voltages.

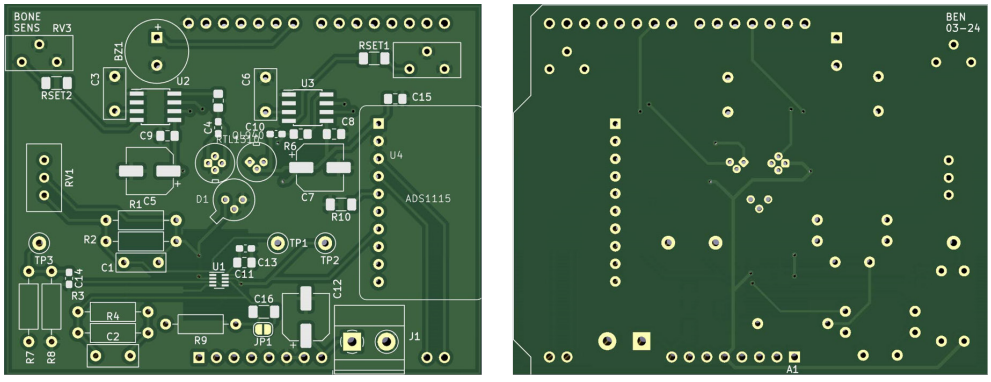

(a) (b)

FIGURE 7.6: PCB layout: a Front view b Back view. Conductive pathways connecting nodes are visible within the ground pour. SMD pads are depicted in silver, and through-holes are represented as golden circles. Components outlines are highlighted in white. The corresponding schematic can be found at Ref. [60].

CONTROL SYSTEM

For this proof-of-concept, we selected an Arduino microcontroller board (Arduino Uno Rev3, Arduino SA, Chiasso, Switzerland), Figure 7.1 (4), for its extensive documentation, support, and ease of programming. The Arduino provides sufficient processing power and memory to handle all aspects of the device's intended functionality, including real-time control of laser diodes, readout and storage of photodiode output, computing for tissue classification, and operating the feedback system.

To convert the output voltage from the receiver's TIA into digital values, we use an external 16-bit ADC (ADS1115, Texas Instruments Inc., Dallas (TX), USA). This ADC offers higher resolution than the Arduino's internal 10-bit ADC, enabling finer granularity and increased accuracy in capturing the analog signals from the TIA. This enhanced resolution is crucial for accurately detecting the small analog signals from the photodiode. Additionally, the selected ADC features programmable gain settings, allowing amplification of weak signals without compromising resolution if needed. The ADC operates independently of the Arduino's processor, handling A/D conversion tasks and freeing up processing power for control functions.

The converted values are communicated to the Arduino using inter-integrated circuit (I2C) communication, which is facilitated by the SCL (serial clock) and SDA (serial data) inputs of the Arduino. The SCL line provides a clock signal to synchronize data transfer, while the SDA line facilitates bidirectional communication. In this setup, the Arduino acts as the master device, controlling the communication process by initiating data transmission, generating the clock signal, and addressing the ADC to send or receive information.

The ADC is mounted on the PCB. To establish a stable connection between PCB and Arduino, male headers are soldered onto the PCB, matching the pin configuration of the Arduino's female headers.

FEEDBACK SYSTEM

In the operating room, efficient feedback representation is vital. While visual feedback offers comprehensive data presentation, audio feedback,

with its capacity to encode one-dimensional data through pitch variation, proves particularly effective in capturing the surgeon's attention without diverting focus from the surgical site, as demonstrated by the PediGuard [37, 38].

We chose a constant tone buzzer (Multicomp Pro MP-ABI-050-RC, Premier Farnell Ltd., Farnell, UK), Figure 7.1 (5), for audio feedback with a sound output of 75 dB. The buzzer uses a piezoelectric element controlled by modulating the digital output to produce distinct auditory signals. The buzzer is mounted on the PCB.

CASING & ASSEMBLY

The diodes are securely housed within a custom 3D-printed diode holder, Figure 7.1 (6a), manufactured using a digital light processing (DLP) printer (Perfactory 4 Mini XL, EnvisionTEC GmbH, Gladbeck, Germany) and HTM 140 V2 resin. They are fixed in place by a lid (6b) fabricated from a stainless steel (AISI 301) sheet using wire electrical discharge machining (EDM). The diode holder and lid are connected by one M2x5 screw and two dowel pins. A stainless steel (AISI 304) capillary tube with an outer diameter of 2.1 mm and an inner diameter of 1.9 mm serves as the shaft (6c) that guides the optical fibers to the probe tip (6d). The tip, made from stainless steel (AISI 316), was crafted on a lathe machine, with holes for the fibers created using wire EDM.

All components are embedded in a two-part housing comprising a tip, Figure 7.1 (7a), and a handle (7b) resembling a screwdriver grip. The flat section of the tip part is milled from stainless steel (AISI 316) with a slot created using wire EDM. The pointed section of the tip part as well as the entire handle part are 3D-printed using DLP with HTM 140 V2 resin. The two tip sections are glued together, and both parts (tip and handle) are connected by three M2.5x20 screws. The Arduino is mounted to the handle using four M3x10 screws and nuts. Figure 7.7 shows the fully assembled probe.

FIGURE 7.7: Photo of the fully assembled handheld probe.

OPERATION OF THE SYSTEM

At startup, the system initializes by configuring ports and communication protocols. During operation, the Arduino generates 5V pulse-width modulation (PWM) signals on pins 6 and 11 to control the laser diodes via their driver ICs. The PWM frequency is set to 55 Hz with a 50% duty cycle. This frequency is synchronized with the ADC readout (55 samples per second (SPS)) to ensure simultaneous activation and readout of each of the laser diodes.

Human auditory response times are typically around 200 ms [39, 40]. Consequently, the user output is set at 5 Hz, and the resulting digital values x from the first (940 nm) and second (1310 nm) laser diode pulses are collected and averaged every 200 ms to calculate the reflection ratio Q:

$$Q = \frac{\bar{x}_{940}}{\bar{x}_{1310}}. \qquad [-] \ (10)$$

The Arduino activates the buzzer connected to pin 8 based on the comparison between Q and a set threshold ratio Q_t. Based on the expected photocurrents, Q_t is set to 4.75. If the currently measured ratio exceeds the threshold ratio, the buzzer is activated, indicating contact with cortical bone; otherwise, it remains inactive.

VALIDATION

DRIVER CIRCUIT

To assess whether the driver circuit is adjustable and able to autonomously regulate the operating current, the input pin IN on the IC mounted on the PCB was connected to a regulated 5V DC power supply for continuous operation. A spare NIR laser diode with a typical operating current of 20 mW and a monitor current of 0.2 mA was used for testing. The IC achieved a stable operating current of 20 mA, as expected, and adjustments to the R_{SET} resistor demonstrated effective current regulation.

To validate proper functionality, an artificial monitor current of 0.5 mA (the maximum allowable for the IC) was generated using a 5V source and a 10 kΩ resistor, simulating high incident power on the photodiode integrated within the laser diode. Applying this current to pin AMD on the IC decreased the operating current and reduced the optical output power, confirming the driver's ability to autonomously regulate current to ensure consistent light output for reliable feedback even over extended periods.

SIGNAL AMPLIFICATION

To validate the AC-coupled TIA, we generated a small AC signal simulating the expected photocurrent using a function generator with an 8.3 MΩ resistor in series, approximating a photocurrent of 337 nA with a bias voltage of 2.8V. A 300 Hz square waveform with a 50% duty cycle was applied to the input of the TIA (negative pin of the first-stage op-amp), and the amplified signal was observed using an oscilloscope (TDS2022B, Tektronix, Beaverton (OR), USA) connected to the output of the two-stage TIA. The system's response is shown in Figure 7.8a. The input frequency was then swept from 300 Hz to 1.5 kHz to observe changes in gain or waveform distortion, see Figure 7.8b.

The gain of the first stage G_1 was set to 440 kV A^{-1}, and the second stage inverts and amplifies the signal by a factor of G_2 = 10 V V^{-1}. The measured output voltage was around 1.4V, indicating a slight deviation from the theoretical output voltage of 1.32V. This discrepancy was consistent among input signal frequencies and may be attributed to minor variations in photocurrent estimation or gain measurement accuracy.

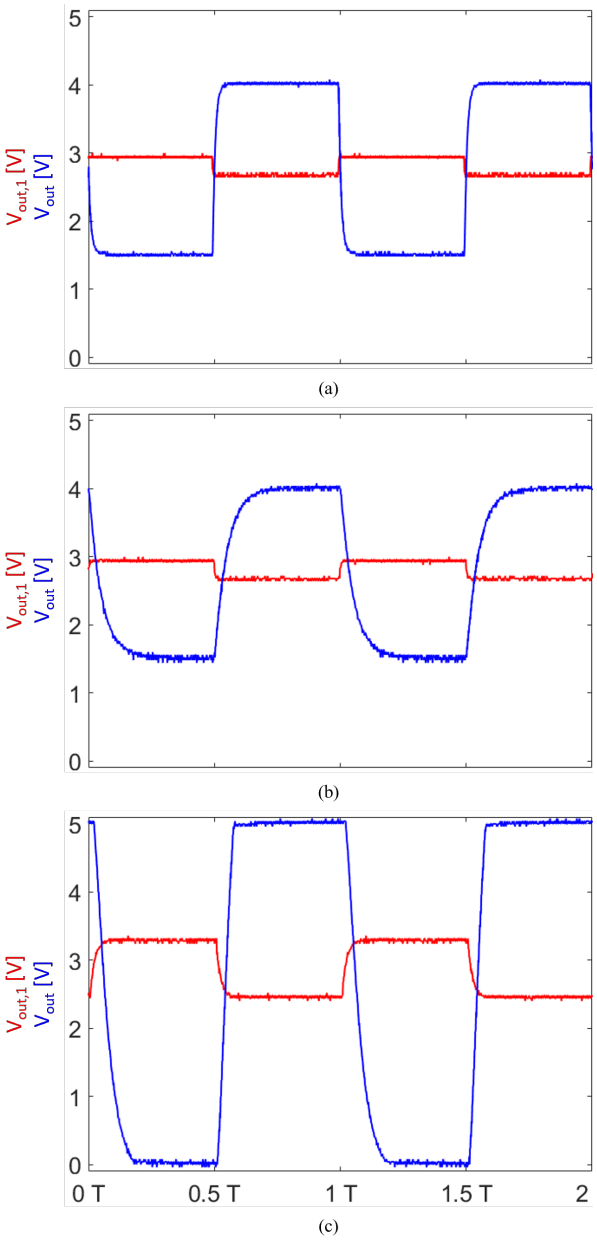

FIGURE 7.8: Response of the two-stage, low-noise transimpedance amplifier circuit with 2.8V bias for a square wave signal input with an amplitude of 337 nA, recorded using an oscilloscope. The output voltage after the first stage is illustrated in red; the output voltage after the second stage is illustrated in blue. a Input signal frequency of 300 Hz with a 50% duty cycle, G_1 = 440 kV A^{-1}. b Input signal frequency of 1.5 kHz with a 50% duty cycle, G_1 = 440 kV A^{-1}. c Input signal frequency of 1.5 kHz with a 50% duty cycle, G_1 ≥ 831 kV A^{-1}.

For a photocurrent of 337 nA, the maximum output swing is achieved at 831 kV A^{-1}. Increasing the gain beyond this value resulted in output saturation, as shown in Figure 7.8c. The AC coupling was verified by confirming that the TIA's output returned to bias when a DC signal was applied.

ASSEMBLED PROTOTYPE

An initial measurement for the assembled prototype was taken with both laser diodes turned off to establish a baseline and confirm a steady output. We expected V_{out} to be 2.7V, corresponding to the selected bias voltage. The device showed steady ADC readings of x_{940} and x_{1310} around 2755, confirming correct bias voltage and no influence from ambient light.

To assess the butt-coupling efficiencies of the diodes, a power meter (S132C + PM100D, Thorlabs Inc., Newton (NJ), USA) measured the output power from the tip of the prototype for both laser diodes in a dark environment. The laser diodes were operated individually in constant mode by holding pin IN on the IC at 5V. The measured incident powers were 7.2 mW for the 51.1 mW 940 nm laser diode (coupling efficiency of 14%) and 80 µW for the 10.3 mW 1310 nm laser diode (essentially no light coupling).

A spare NIR laser diode with a nominal output power of 50 mW was placed in front of the tip of the prototype and operated at 55 Hz with a 50% duty cycle to assess photodiode coupling. No incoming signal was registered (x = 2755), indicating no light coupling for the photodiode.

To verify correct functioning of our assembled prototype, apart from the optical coupling, we replaced the 940 nm laser diode with a fiber-coupled laser diode of comparable properties (same wavelength and output power) including a single-mode fiber with 9 µm core diameter (SPL940-50-9-PD, Roithner Lasertechnik GmbH, Vienna, Austria). The photodiode is replaced by a fiber-receptacle photodiode with an active area of 1 mm diameter (FCPD-1000-FC, Roithner Lasertechnik GmbH, Vienna, Austria). The photodiode is connected to a 400 µm core diameter optical fiber with an NA of 0.22 through an FC/PC connector (M146L02, Thorlabs Inc., Newton (NJ), USA). The fibers are included in a modified probe tip that matches the new fiber diameters while maintaining the SDS at 1.3 mm.

The fiber-coupled laser diode was activated using a PWM frequency of 55 Hz with a 50% duty cycle. The probe was positioned 3 mm away from a Spectralon white reference standard (WS-1-SL, Labsphere Inc.,North Sutton (NH), USA) to assess the device's optical functionality. With amplification set at its highest setting of 50 MV A^{-1} and 99% reflection from the reference standard, we expected V_{out} to drop and saturate at 0V. When the 940 nm laser was activated, the digitized reflectance value was indeed x_{940} = 0, confirming that photons are emitted by the 940 nm laser diode, reflected off the white reference standard, and collected by the photodiode.

Next, the probe was placed in cancellous bone-mimicking phantom (pure coconut milk with a fat content of 17% [23]), providing a highly controlled environment, allowing us to isolate and validate the technical performance of the device without the biological variability inherent in *ex-vivo* or *in-vivo* tissue. Reflectance was measured, and with an amplification of 50 MV A^{-1}, the digitized reflectance value was saturating at x_{940} = 0. Reducing the amplification to 6 MV A^{-1} resulted in a digitized reflectance value of $x_{940} \approx$ 500, demonstrating that even with low tissue reflectance, our device can collect a measurable signal.

DISCUSSION

In this paper, we presented a handheld fiber-optic tissue sensing device for spine surgery. Our design prioritizes size, cost, and speed, and comprises two laser diodes as the light source, a photodiode as the photodetector, a double-sided PCB for the electronic circuits, an Arduino Uno as the control unit, a buzzer for audio feedback, and a casing to house all components within a handheld device. The device generates real-time audio feedback to help surgeons prevent pedicle screw breaches and improve overall accuracy during spinal fusion.

The limited availability of compact and cost-effective laser diodes with the required wavelengths led us to use manually fiber-coupled laser diodes with butt-coupling in our prototype, resulting in low coupling efficiencies. Despite its simplicity and common use in practical device implementation, butt-coupling is the least efficient method for coupling

a light source to a fiber because it does not match the fiber's numerical aperture. The high divergence of laser light emitted from the diode's active area causes a significant portion of light to fall outside the fiber core's diameter and acceptance angle, leading to leakage and only a fraction being permanently guided through the fiber [34, 41], and potential misalignments further reduce throughput efficiency. Additionally, excessive optical adhesive and reflections within the diode holder or housing can cause light to reach the sensor without interacting with the tissue. By replacing butt-coupled diodes with off-the-shelf fiber-coupled alternatives, our research demonstrated successful light emission and collection from tissue phantom within a handheld device. However, purchasing fiber-coupled laser diodes imposes constraints regarding size, wavelength, and fiber type/diameter, and can be significantly more expensive, especially for customized components.

To mitigate these shortcomings, reliable assembly tools and processes for butt-coupling have to be established to align the fiber and diode surfaces with high precision. Innovative methods can help with the alignment of the optical fiber and the diode. For example, integrating optical fibers during 3D printing through continuous fiber reinforcement (CFR) can be advantageous. The Mark Two printer (Markforged, Watertown (MA), USA) can reinforce 3D printed parts with carbon, fiberglass, or Kevlar fibers [42], which could facilitate the integration of fiber optics. Alternatively, tapered micro lenses offer better coupling efficiency by addressing both internal factors (such as laser wavelength and beam waist radius, lens shape and refractive index, fiber diameter and refractive index) and external factors (like alignment errors) [43].

While our prototype specifically focuses on spine surgery, DRS has been demonstrated as a useful tool in other body regions like the colon, lungs, or breast [44-47].

SIZE CONSIDERATIONS

The bone sensing device was designed so that the PCB functions as a shield for the Arduino Uno, with diodes positioned for easy connection and coupling of the electronics and optics. By optimizing the PCB layout and placing components on both sides, a smaller and more compact

housing can be achieved, improving the handling of the handheld probe. Integrating a microcontroller onto the PCB and using only SMD components can further reduce the overall size.

The handheld device is currently powered via a USB supply, with the alternative option to power it via a screw terminal. For autonomous operation, a battery is required to power the device. The op-amp consumes a maximum of 2 mA. The 940 nm laser diode operates at 60 mA, and the 1310 nm laser diode operates at 35 mA. Since the laser diodes are pulsed at a 50% duty cycle, their effective current draw is halved. The ADC uses 150 µA in continuous mode, and the IC consumes up to 15 mA. This results in a total current consumption of approximately 65 mA for the optics and electronics. The Arduino Uno has an idle current consumption of 50 mA, increasing to an estimated maximum of 100 mA when running code. Consequently, the total current consumption for the device is approximately 165 mA.

Spinal fusion surgery can take up to 8 hours, depending on the extent of damage, the method of fusion, and the surgical approach used [48, 49]. To ensure a safety margin, the battery should last for at least 12 hours. Therefore, a battery capacity of 1980 mA h at 5V is required. This can be provided by a suitable battery pack (*e.g.*, 5V 18650 Lithium Ion Battery Pack 2200mAh, Himax Electronics Co. Ltd., Shenzhen, China), a 1.5V AA battery with sufficient capacity and a boost converter (*e.g.*, U1V10F5, Pololu, Las Vegas (NV), USA), or three AA or AAA batteries in series to achieve the necessary voltage. With the current design, the handle of the housing still leaves some space for a battery to fit in.

COST CONSIDERATIONS

The optical and electronic components integrated into our handheld device are low-cost and readily available. By determining the output power requirements of the light source, we can explore the feasibility of replacing laser diodes with much cheaper LEDs to optimize costs without compromising device functionality. Although integrating optical components inherently increases production costs compared to electric-only devices like the PediGuard, this increase may be justified by the potential for superior performance. Additionally, alternative microcontroller

options could offer cost-effective substitutes for the Arduino used in this proof-of-concept, further enhancing the device's affordability.

Currently, manufacturing and assembly efforts are significant factors in the overall cost. While initial prototype costs are higher than those in serial production, there is potential to reduce these costs. Soldering small components onto the PCB is currently done manually under a microscope, but with known component sizes, PCB assembly can be outsourced. Manufacturing EDM parts requires special equipment and training, so the design should be revised to employ cheaper manufacturing techniques such as computerized numerical control (CNC) machining or laser cutting. Although 3D printing is beneficial for prototyping or personalization of medical instruments [50], it is relatively slow and expensive for serial production. Therefore, printed parts should be redesigned for production-friendly manufacturing methods like injection molding.

SPEED CONSIDERATIONS

The device's operational frequency, capped at 55 Hz by the Arduino's capabilities, presents a significant constraint. While the Arduino Uno is ideal for prototyping thanks to its user-friendly interface and ease of programming, its 10-bit ADC resolution is insufficient for high-accuracy measurements, limiting its application in specialized designs. To mitigate this constraint, an external high-resolution ADC with a maximum sampling rate of 860 SPS was integrated. However, the slow communication between the external ADC and Arduino diminishes the device's operating speed. This communication bottleneck is compounded by I2C protocol delays, ADC conversion times, and software overhead, which collectively reduce the practical sampling rate.

To overcome these challenges, upgrading to a more powerful microcontroller like ARM (ARM Holdings Limited, Cambridge, UK) or ESP (Espressif Systems, Shanghai, China) variants offers superior processing power, memory, and versatile Input/Output (I/O) capabilities. Choosing the right microcontroller depends on specific application requirements for functionality, operational conditions, and packaging. Both options represent significant advancements over the Arduino Uno, ensuring a more robust and efficient system [51], next to cutting size and cost.

The current speed limitation results in a slow pulse repetition frequency. Increasing this frequency for faster probing allows to detect changes in signal more rapidly, and with higher pulse and sampling rates, larger datasets can be generated within the same time frame to facilitate smoother and more stable averaged signals for calculating the reflection ratio.

FUTURE WORK

We acknowledge that the current experiments are foundational and relatively simple, thus unable to fully assess the performance of our device in a clinical setting. However, as this work represents an early-stage proof-of-concept, the primary goal was to demonstrate the feasibility of this novel approach and validate our design through initial testing. Future optimization will involve more comprehensive evaluations, including *ex-vivo* trials, validation against conventional guidance technologies, and design iterations to fully validate its potential for clinical translation.

In the next step, the device should be validated according to its intended use by testing the prototype on cancellous and cortical bone samples from *ex-vivo* human or porcine vertebrae to replicate tissue sensing during spine surgical interventions. A sufficiently large sample of reflectance values ($\approx$ 50) should be obtained for both tissues, and their distributions should be assessed. The reflection ratio Q for both cancellous and cortical bone should be computed for each reading and analyzed to verify the set threshold ratio and adjust it if necessary. The final threshold will be determined based on the results from experiments using human tissues. If Q_{t} successfully separates the distributions of Q_{canc} and Q_{cort}, it indicates that the two tissue types can be distinguished. Otherwise, a more complex metric than the reflection ratio may be necessary.

Furthermore, our study raises several considerations for the design and implementation of a handheld fiber-optic tissue sensing device. Variations in optical coupling efficiency among prototypes may influence the recorded signal, necessitating time-consuming calibration of each device to establish the threshold ratio. Ensuring uniformity in threshold ratio values across prototypes and procedures is crucial to avoid the need for recurrent recalibration by manufacturers or surgeons.

Additionally, in the future, our device will need to be validated against conventional guidance technologies in spine surgery, such as fluoroscopy and computer-assisted navigation. Notably, DRS has previously been benchmarked against Magnetic Resonance Imaging (MRI) for quantifying vertebral bone fat fraction [52], underscoring its potential to provide reliable tissue feedback. Previous work on *ex-vivo* human tissue and *in-vivo* swine models has established DRS as a viable tissue sensing technology for spine surgery [16, 20]. Comparative studies will further establish the device's performance and its potential for integration into clinical practice.

Moreover, future iterations of our device must prioritize enhanced mechanical robustness to accommodate *in-vivo* operations, where surgeons apply considerable forces to the bone [53]. Drawing from experience in earlier *ex-vivo* and *in-vivo* tests of DRS probes [18, 20], we focused on securely coupling the optical fibers in this design. Redesign efforts should ensure that the device withstands the substantial mechanical stresses exerted on the handle and probe shaft during surgical procedures. In addition to mechanical robustness and sensing capabilities, usability in clinical practice is essential, and close collaboration with surgeons is encouraged to ensure the device meets clinical needs and integrates seamlessly into surgical workflows.

Design considerations extend to choosing between a single-use or a sterilizable device. While single-use devices mitigate contamination risks, they raise concerns about environmental sustainability. Achieving complete sterilizability poses challenges in ensuring the functionality of all components post-sterilization [54]. However, technologies for sterilizing fiber-based systems, such as fiber-optic endoscopes, are well-established [55], demonstrating that sterilization of optical components is feasible. Alternatively, a semi-reusable approach is imaginable, where only the shaft that comes in touch with the patient is disposable while the remaining components are reusable, balancing cost-effectiveness with environmental impact.

To further advance fiber-optic tissue sensing, several research directions could be explored. One potential improvement is multi-directional sensing, which would enable directional tissue feedback to detect

breaches impending from various angles [56]. Another promising avenue is the integration of machine learning algorithms for real-time classification of tissue types, potentially increasing the speed and reliability of intraoperative feedback [57, 58]. Additionally, combining DRS with complementary sensing modalities, such as ultrasound or electrical impedance, could provide a more comprehensive assessment of tissue properties, broadening the applicability of fiber-optic sensing across various surgical specialties.

Eventually, implementing optical systems and fiber optic probes in medical environments requires regulatory approval and large-scale manufacturing of sterile probes, necessitating cost and complexity reduction. Future steps for translation into clinical settings include comprehensive clinical studies to validate device performance and usability for regulatory compliance and eventual commercialization. Biocompatibility of device components, particularly those in direct patient contact, must be guaranteed. Medical-grade stainless steel for the tip and biocompatible fibers [59] ensure patient safety and regulatory approval.

CONCLUSION

Our handheld fiber-optic tissue sensing device utilizes DRS to distinguish bone tissues, demonstrating potential to provide surgical guidance in spinal fusion procedures. Thanks to its compact size and low cost, the device is well-suited for healthcare facilities with limited access to expensive surgical technologies, while also being compatible as an add-on to existing computer-assisted navigation or robotic-assisted systems. Despite initial challenges with fiber coupling, the device's compact design, affordability, and real-time feedback capabilities highlight its value as a potential tool in clinical settings, aimed at enhancing patient outcomes through improved pedicle screw placement accuracy.

REFERENCES

1. Lee, Ronald. "The demographic transition: three centuries of fundamental change." Journal of economic perspectives 17.4 (2002): 167-190.

2. Beschloss, Alexander, et al. "Marked increase in spinal deformity surgery throughout the United States." Spine 46.20 (2021): 1402-1408.

3. Boucher, Harold H. "A method of spinal fusion." The Journal of Bone & Joint Surgery British Volume 41.2 (1959): 248-259.

4. Inamasu, Joji, and Bernard H. Guiot. "Vascular injury and complication in neurosurgical spine surgery." Acta neurochirurgica 148 (2006): 375-387.

5. Manbachi, Amir, et al. "Guided pedicle screw insertion: techniques and training." The Spine Journal 14.1 (2014): 165-179.

6. Gautschi, Oliver P., et al. "Clinically relevant complications related to pedicle screw placement in thoracolumbar surgery and their management: a literature review of 35,630 pedicle screws." Neurosurgical focus 31.4 (2011): E8.

7. Bourgeois, Austin C., et al. "The evolution of image-guided lumbosacral spine surgery." Annals of Translational Medicine 3.5 (2015).

8. Härtl, Roger, et al. "Worldwide survey on the use of navigation in spine surgery." World neurosurgery 79.1 (2013): 162-172.

9. Liu, Hao, et al. "Comparison of the accuracy between robot-assisted and conventional freehand pedicle screw placement: a systematic review and meta-analysis." International journal of computer assisted radiology and surgery 11 (2016): 2273-2281.

10. Ghasem, Alexander, et al. "The arrival of robotics in spine surgery: a review of the literature." Spine 43.23 (2018): 1670-1677.

11. Zaffino, Paolo, et al. "A review on advances in intra-operative

imaging for surgery and therapy: imagining the operating room of the future." Annals of Biomedical Engineering 48.8 (2020): 2171-2191.

12. Park, Hangeul, et al. "The utility of intraoperative ultrasonography for spinal cord surgery." Plos one 19.7 (2024): e0305694.

13. Bolger, Ciaran, et al. "Electrical conductivity measurement: a new technique to detect iatrogenic initial pedicle perforation." European Spine Journal 16 (2007): 1919-1924.

14. Chaput, Christopher D., et al. "Reduction in radiation (fluoroscopy) while maintaining safe placement of pedicle screws during lumbar spine fusion." (2012): E1305-E1309.

15. Guillen, Phillip T., et al. "Independent assessment of a new pedicle probe and its ability to detect pedicle breach: a cadaveric study." Journal of Neurosurgery: Spine 21.5 (2014): 821-825.

16. Swamy, Akash, et al. "Diffuse reflectance spectroscopy, a potential optical sensing technology for the detection of cortical breaches during spinal screw placement." Journal of biomedical optics 24.1 (2019): 017002-017002.

17. Losch, Merle S., et al. "Proton density fat fraction of the spinal column: an MRI cadaver study." BioMedical Engineering OnLine 20 (2021): 1-11.

18. Burström, Gustav, et al. "Diffuse reflectance spectroscopy accurately identifies the pre-cortical zone to avoid impending pedicle screw breach in spinal fixation surgery." Biomedical optics express 10.11 (2019): 5905-5920.

19. Fisher, Michael A. "Smart pedicle tool." US patent US 8249696 B2 (2007)

20. Swamy, Akash, et al. "Diffuse reflectance spectroscopy for breach

detection during pedicle screw placement: a first in vivo investigation in a porcine model." BioMedical Engineering OnLine 19 (2020): 1-12.

21. Fisher, Carl, et al. "Perspective on the integration of optical sensing into orthopedic surgical devices." Journal of Biomedical Optics 27.1 (2022): 010601.

22. Losch, Merle S., et al. "Fiber-Optic Pedicle Probes to Advance Spine Surgery through Diffuse Reflectance Spectroscopy." Bioengineering 11.1 (2024): 61.

23. Losch, Merle S., et al. "Diffuse reflectance spectroscopy of the spine: improved breach detection with angulated fibers." Biomedical Optics Express 14.2 (2023): 739-750.

24. Zijlstra, Willem G., et al. "Absorption spectra of human fetal and adult oxyhemoglobin, de-oxyhemoglobin, carboxyhemoglobin, and methemoglobin." Clinical chemistry 37.9 (1991): 1633-1638.

25. Nachabé, Rami, et al. "Estimation of biological chromophores using diffuse optical spectroscopy: benefit of extending the UV-VIS wavelength range to include 1000 to 1600 nm." Biomedical optics express 1.5 (2010): 1432-1442.

26. Nachabé, Rami, et al. "Validation of interventional fiber optic spectroscopy with MR spectroscopy, MAS-NMR spectroscopy, high-performance thin-layer chromatography, and histopathology for accurate hepatic fat quantification." Investigative radiology 47.4 (2012): 209-216.

27. Duperron, Matthieu, et al. "Diffuse reflectance spectroscopy-enhanced drill for bone boundary detection." Biomedical optics express 10.2 (2019): 961-977.

28. Li, Celina L., et al. "Extended-wavelength diffuse reflectance spectroscopy dataset of animal tissues for bone-related biomedical applications." Scientific Data 11.1 (2024): 136.

29. Li, Celina L., et al. "Frameworks of wavelength selection in diffuse reflectance spectroscopy for tissue differentiation in orthopedic surgery." Journal of Biomedical Optics 28.12 (2023): 121207-121207.

30. Marti, Dominik, et al. "MCmatlab: an open-source, user-friendly, MATLAB-integrated three-dimensional Monte Carlo light transport solver with heat diffusion and tissue damage." Journal of biomedical optics 23.12 (2018): 121622-121622.

31. Frank, Christopher J., et al. "Raman spectroscopy of normal and diseased human breast tissues." Analytical chemistry 67.5 (1995): 777-783.

32. Chen, Yongmei, et al. "Thermal effects of transcranial near-infrared laser irradiation on rabbit cortex." Neuroscience letters 553 (2013): 99-103.

33. Hall, Dennis G., et al. "Simple Gaussian-beam model for GaAlAs double-heterostructure laser-diode-to-diffused-waveguide coupling calculations." Optics letters 4.9 (1979): 292-294.

34. Karioja, Pentti, and Dennis Howe. "Diode-laser-to-waveguide butt coupling." Applied optics 35.3 (1996): 404-416.

35. Heinrich, Jürgen, et al. "Butt-coupling efficiency of VCSELs into multimode fibers." IEEE Photonics Technology Letters 9.12 (1997): 1555-1557.

36. Horowitz, Paul, et al. The art of electronics. Vol. 2. Cambridge: Cambridge university press, 1989.

37. Cho, Byunghyun, et al. "A surgical navigation system for guiding exact cochleostomy using auditory feedback: a clinical feasibility study." BioMed research international 2014.1 (2014): 769659.

38. Bhogal, Harkirat, et al. “Bone conductivity and spine fluoroscopy, Hand-Eye-Ear dialogue, during pedicle screw positioning: a new human cognitive system for precision and radiation-decrease; better than artificial intelligence and machine learning system?.” International Orthopaedics 47.2 (2023): 421-428.

39. Thompson, Philip D., et al. “Voluntary stimulus-sensitive jerks and jumps mimicking myoclonus or pathological startle syndromes.” Movement disorders: official journal of the Movement Disorder Society 7.3 (1992): 257-262.

40. Jain, Aditya, et al. “A comparative study of visual and auditory reaction times on the basis of gender and physical activity levels of medical first year students.” International journal of applied and basic medical research 5.2 (2015): 124-127.

41. Ivanov, Oleg V., et al. “Cladding modes of optical fibers: properties and applications.” Physics-Uspekhi 49.2 (2006): 167.

42. Melenka, Garrett W., et al. “Evaluation and prediction of the tensile properties of continuous fiber-reinforced 3D printed structures.” Composite Structures 153 (2016): 866-875.

43. Zhou, Haibo, et al. “Review of the technology of a single mode fiber coupling to a laser diode.” Optical Fiber Technology 55 (2020): 102097.

44. Zonios, George, et al. "Diffuse reflectance spectroscopy of human adenomatous colon polyps in vivo." Applied optics 38.31 (1999): 6628-6637.

45. Baltussen, Elisabeth J. M., et al. "Using diffuse reflectance spectroscopy to distinguish tumor tissue from fibrosis in rectal cancer patients as a guide to surgery." Lasers in surgery and medicine 52.7 (2020): 604-611.

46. Evers, Daniel J., et al. "Diffuse reflectance spectroscopy: a new guidance tool for improvement of biopsy procedures in lung malignancies." Clinical lung cancer 13.6 (2012): 424-431.

47. de Boer, Lisanne L., et al. “Fat/water ratios measured with diffuse reflectance spectroscopy to detect breast tumor boundaries.” Breast cancer research and treatment 152 (2015): 509-518.

48. Kim, Bobby D., et al. “Operative duration as an independent risk factor for postoperative complications in single-level lumbar fusion: an analysis of 4588 surgical cases.” Spine 39.6 (2014): 510-520.

49. Yamato, Yu, et al. “Extensive spinal fusion surgery in patients with Parkinson disease or atypical Parkinsonism: time course of clinical outcomes in 5 years progress report.” Spine 45.4 (2020): E217-E226.

50. Culmone, Costanza, et al. "A fully 3D-printed steerable instrument for minimally invasive surgery." Materials 14.24 (2021): 7910.

51. Parai, Manas K., et al. "An overview of microcontroller unit: from proper selection to specific application." International Journal of Soft Computing and Engineering (IJSCE) 2.6 (2013): 228-231.

52. Swamy, Akash, et al. "Validation of diffuse reflectance spectroscopy with magnetic resonance imaging for accurate vertebral bone fat fraction quantification." Biomedical optics express 10.8 (2019): 4316-4328.

53. Timmermans, Maikel, et al. “State-of-the-Art of Non-Radiative, Non-Visual Spine Sensing with a Focus on Sensing Forces, Vibrations and Bioelectrical Properties: A Systematic Review.” Sensors 23.19 (2023): 8094.

54. Stolov, Andrei A., et al. "Effects of sterilization methods on key properties of specialty optical fibers used in medical devices." Optical Fibers and Sensors for Medical Diagnostics and Treatment Applications XIII. Vol. 8576. SPIE, 2013.

55. Widmer, Andreas F., and Reno Frei. "Decontamination, disinfection, and sterilization." Manual of clinical microbiology (1999): 138-164.

56. Losch, Merle S., Jenny Dankelman, and Benno HW Hendriks. "Seeing from a new angle: design of a sideways-looking fiber-optic probe to advance spine surgery." Advanced Biomedical and Clinical Diagnostic and Surgical Guidance Systems XXII. Vol. 12831. SPIE, 2024.

57. Dahlstrand, Ulf, et al. "Extended-wavelength diffuse reflectance spectroscopy with a machine-learning method for in vivo tissue classification." Plos one 14.10 (2019): e0223682.

58. Nguyen, Mayna H., et al. "Machine learning to extract physiological parameters from multispectral diffuse reflectance spectroscopy." Journal of Biomedical Optics 26.5 (2021): 052912-052912.

59. Wang, Yue, et al. "Biocompatible and biodegradable polymer optical fiber for biomedical application: A review." Biosensors 11.12 (2021): 472.

60. doi.org/10.4121/77363d00-f68c-4da7-b32e-3aabe957ef98.

08

DISCUSSION

FINDINGS OF THIS THESIS

The rising aging population and an increase in the number of spinal fusion surgeries have created a growing clinical need for better technologies to guide pedicle screw placement [1, 2]. One of the major reasons for not using surgical navigation today is its costs [3], emphasizing the need for a simple, less resource-intensive device to detect breaches during spinal fusion surgery. The aim of this PhD research therefore was to investigate the potential of Diffuse Reflectance Spectroscopy (DRS) for directional tissue feedback, and to overcome practical challenges encountered during its integration into surgical instruments and workflows.

TISSUE COMPOSITION OF THE SPINE

Our preliminary investigation into the composition of bone tissues in the spine was motivated by the hypothesis that DRS can distinguish between different tissues based on their compositions. Building upon prior studies [4, 5], we identified a decline in fat fraction at 1 mm from the cortical boundary, followed by a significant drop occurring at the boundary itself **(Chapter 2).**

The observed decrease in fat fraction within cancellous bone near the cortical boundary supports the existence of a transition zone between these tissue types. The relationship between lipid content and bone tissue type establishes fat fraction as a reliable indicator for differentiating cancellous and cortical bone, highlighting the potential of DRS for intra-operative guidance and setting the foundation for developing a DRS device for spine surgery. Moreover, these findings provide physiological support for the use of specific wavelengths associated with lipid absorption in spine surgical DRS applications.

DRS FOR DIRECTIONAL TISSUE FEEDBACK

Fiber-optic technology enables the manipulation of light emission and collection in DRS systems. Our exploration of light-beam steering in fiber-optic medical devices showed a variety of industry-driven innovations **(Chapter 3)**. Refraction and reflection predominantly facilitate off-axis light emission and collection, and a decrease in angular distribution of light. Conversely, scattering increases angular distribution, while diffraction enables light beam splitting.

An investigation into the impact of angulated fibers on the DRS probing volume led to a decision for a high fiber angle over two parallel fibers **(Chapter 4)**. This configuration enabled breach detection at various angles with just two fibers, ranging from perpendicular to acute 45° breaches. Although this setup still requires a relatively large probe due to the angulated fibers, light beam steering with modified fiber tips for diffuse emission and sideways collection allows integration of directional sensing into a probe with confined dimensions. Diffuse emission introduced no disturbance on perpendicular breach detection, while sideways collection considerably enhanced the detection of parallel breaches **(Chapter 5)**. Breaches can thus be prevented by sensing in multiple directions with a three-fiber probe, establishing DRS as a strong alternative to current surgical guidance systems.

TOWARDS PRACTICAL IMPLEMENTATION OF DRS IN THE OPERATING ROOM

The potential applications of DRS in enhancing pedicle screw placement are twofold. Firstly, it can serve as a standalone aid in low-resource settings; secondly as an add-on to existing computer-assisted navigation or robot-assisted spinal fusion surgeries. Current surgical guidance systems often struggle with real-time visualization of internal structures, making it challenging to detect subtle spine movements affecting instrument positioning. Complementing these systems with DRS offers improved accuracy and patient safety.

To facilitate the integration of DRS into spinal fusion procedures, it needs to be incorporated into surgical instruments such as pedicle screws [5, 6], K-wires and Jamshidi needles [7], or bone drills [8]. Our investigation focused on incorporating DRS into pedicle probes commonly used to pierce through bone during spinal fusion. Our findings stressed the importance of balancing tip angle with probing depth and signal-to-noise ratio (SNR) **(Chapter 6)**. Tips featuring a single 30° bevel proved optimal for sensing while maintaining mechanical performance. Alternatively, a cone-shaped tip design can be realized by positioning one fiber at the tip.

Our fiber-optic pedicle probe connects to a DRS console to produce a raw spectrum, which then requires efficient processing to ensure that surgical

staff can interpret the data and make informed decisions in surgery. Conventionally, fitting algorithms are employed to compare the collected spectrum against known absorption spectra of selected chromophores [9-13]. However, with the availability of large datasets, machine learning techniques emerge as an alternative for processing spectral information and classifying probed tissue without the need for prior knowledge [14-17]. Unlike end-to-end learning, feature selection identifies the best wavelengths for tissue distinction while preserving physiological interpretability [18-20].

These recent advancements have allowed us to rethink DRS implementation to overcome the limitations inherent in current systems, which are characterized by bulky, expensive setups and complex computational requirements for spectral processing. With our latest prototype, we created a simple, handheld device for real-time tissue feedback. By employing laser diodes at only two distinct wavelengths for tissue illumination rather than broadband light, we eliminated the need for a spectrometer and directly measured light with a photodiode **(Chapter 7)**. This design choice simplified our system, keeping it compact and affordable to make DRS accessible to spine surgeons across various settings. A microcontroller served as the central unit to operate the components and provide real-time audio feedback. Despite challenges with fiber coupling, our prototype demonstrated potential for surgical guidance by successfully emitting and collecting light for DRS.

RECENT DEVELOPMENTS

Applying our insights on DRS for directional tissue feedback, we designed a flexible fiber-optic probe capable of multi-directional sensing by integrating diffuse light emission with forward and sideways light collection. The probe tip layout, illustrated in Figure 8.1a, features three fibers positioned at a distance d_f = 1.4 mm each. Manufactured from stainless steel and measuring only 1.8 mm in diameter and 2 mm in length (Figure 8.1b-c), the tip prototype connects to a flexible polyimide tubing shaft (ID = 1.47 mm, wall thickness = 0.064 mm, Nordson Medical, Loveland (CO), USA) covered with polyester shrink tubing

(ID = 1.98 mm, wall thickness = 0.0076 mm, Nordson Medical, Loveland (CO), USA), to yield the probe shown in Figure 8.2.

To evaluate tissue differentiation capabilities, we obtained various porcine tissues from a local butcher, including cortical bone, cancellous bone, adipose tissue, muscle, skin, intervertebral disk, spinal cord, and interspinous ligament. We conducted multiple measurements across different tissue locations (ten locations for spinal cord and interspinous ligament, 25 for all other tissues), averaging ten readings per location.

In Figure 8.3a, the filtered and normalized reflectance spectra (λ_o = 1211 nm) are plotted relative to the normalized reflectance spectrum of cortical bone to investigate spectral differences and reveal distinct shapes for each tissue type within the wavelength range of 1000 nm to 1400 nm. Notably, cancellous bone (blue) exhibits unique intensity changes around 1110 nm and 1290 nm, distinguishing it from other tissues. Moreover, intensity ratios at specific wavelengths (*e.g.*, 1188 nm vs. 1211 nm) can serve as quantitative metrics for tissue distinction [20], with cortical and cancellous bone exhibiting clear differences across the boxplots shown in Figure 8.3b.

These findings demonstrate that DRS effectively distinguishes between tissues based on their spectral shapes or individual intensity ratios and support DRS as a valid alternative to existing systems. Miniaturization facilitates integration into steerable surgical instruments, exemplified by the tsetse fly-inspired bone drill [21], thereby expanding the utility of DRS.

FUTURE PERSPECTIVES

To promote the adoption of DRS in surgical settings, some remaining obstacles need to be cleared out of the way. With a prototype that incorporates all findings presented in this dissertation and is capable of addressing practical challenges, the next steps on the way to market readiness can be completed. Other future applications are also imaginable.

MULTI-DIRECTIONAL SENSING

While our research enables tissue sensing in both forward and sideways directions within a miniature tip, restricting surgeons to probing tissue in

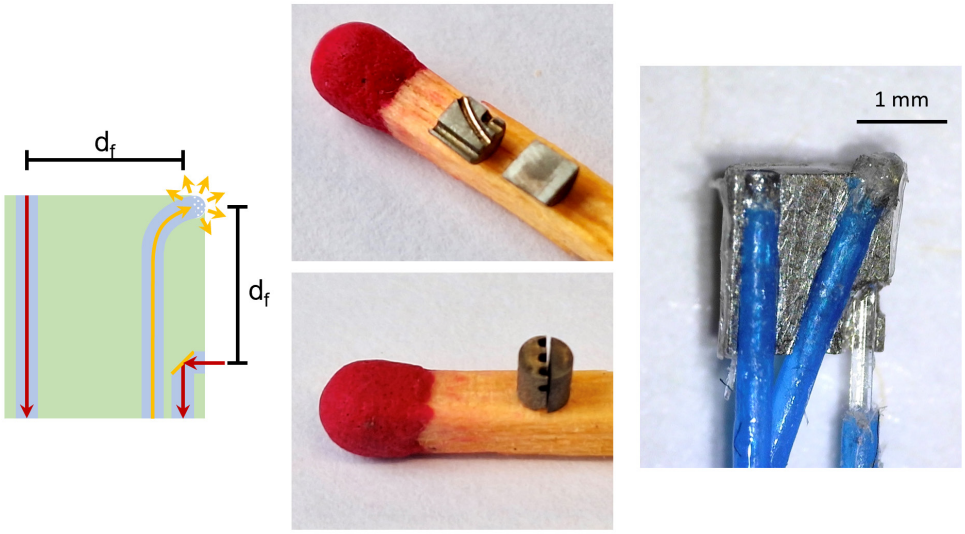

FIGURE 8.1: a Illustration of the probe tip layout encompassing three optical fibers for diffuse light emission and forward and sideways light collection. b Tip prototype with space for three optical fibers (dimensions: ø 1.8 mm, 2 mm long). c Microscopic image of the tip prototype with three optical fibers inserted.

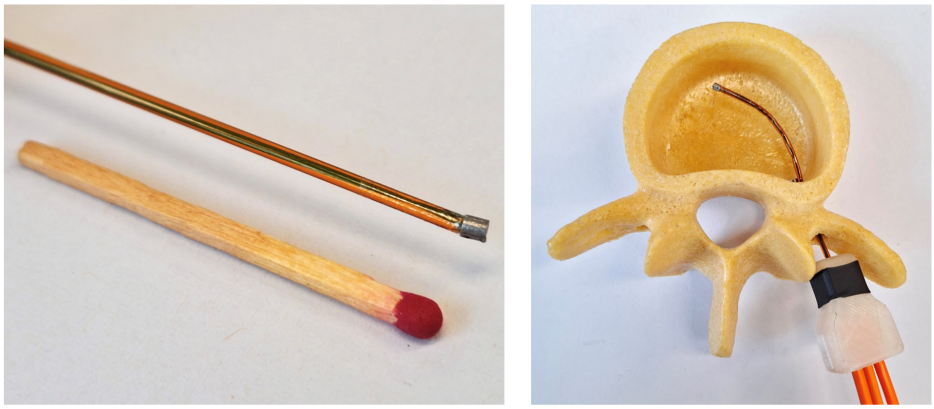

FIGURE 8.2: Probe prototype with tip and flexible shaft: a straight alignment b curved alignment within artificial vertebra.

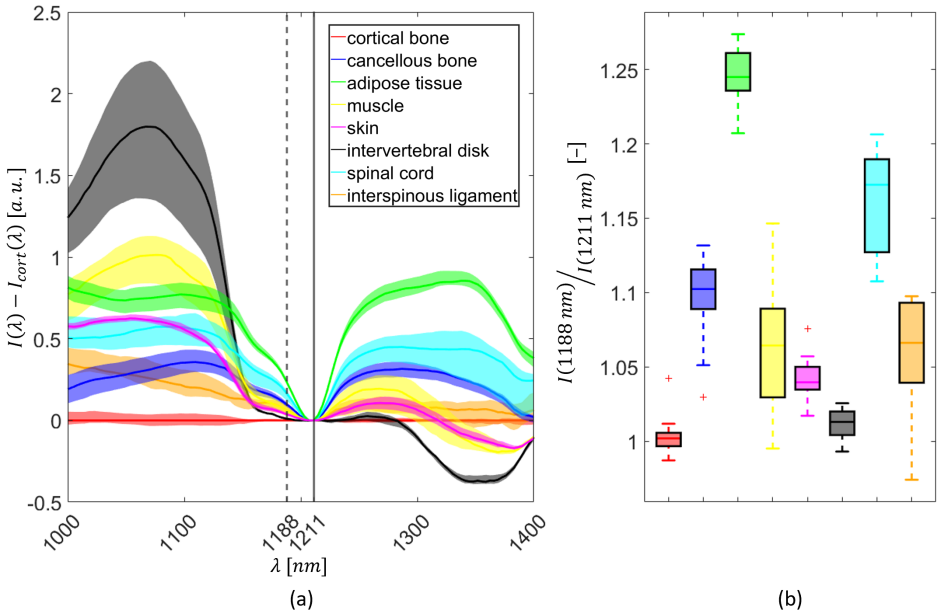

FIGURE 8.3: a Normalized reflectance spectra (λ_o = 1211 nm) for different tissues relative to the normalized reflectance spectrum of cortical bone with forward light collection. The median spectrum is displayed as a solid line. Around the median spectrum, the interquartile range is highlighted in the corresponding color. b Normalized intensity at λ = 1188 nm (λ_o = 1211 nm) for different tissues.

a single sideways direction proves impractical. Incorporating additional fibers into the probe design allows simultaneous sensing in multiple directions, albeit at the cost of increased device complexity. Determining the optimal number of fibers, along with addressing associated practical challenges such as implementing a mechanism for switching between inputs from the individual collecting fibers and establishing a white reference standard for quick calibration, are required to enhance the probe's usability in the operating room.

COMBINING ELEMENTS FOR THE IDEAL DRS PROBE

Insights from our various projects show that developing the ideal DRS probe for pedicle screw placement requires the integration of several crucial elements. Firstly, our handheld probe simplifies the setup considerably. Ergonomic design will enhance user comfort and usability. The inclusion of a sharp tip to facilitate tissue penetration impacts the

probe's sensing capabilities. Adjusting the fiber layout to protrude the collecting fiber relative to the emitter(s) can mitigate this influence. Lastly, incorporating fibers with modified tips to steer light enables directional feedback. By combining these components, a DRS probe suited for surgical guidance can be developed.

CLINICAL VALIDATION, REGULATORY COMPLIANCE, AND COMMERCIALIZATION

Upon finalizing the prototype, the next steps involve validating, obtaining regulatory approval for, and commercializing the technology for widespread clinical adoption. Firstly, clinical studies are needed to assess the efficacy and safety of the prototype in real-world surgical scenarios [22]. Randomized controlled trials are recommended to address the gap in high-quality studies on patient outcomes, and evaluate mortality, revision surgery, and morbidity associated with neural and vascular injuries and pain. Usability testing is also essential to ensure that the device is user-friendly in a clinical setting [23, 24].

Secondly, obtaining regulatory approval, such as compliance with the Medical Device Regulation (MDR) in Europe or the regulations set forth by the Food and Drug Administration (FDA) in the United States, will ensure safety and effectiveness of the technology for clinical use. Adherence to regulatory standards and guidelines, such as ISO 13485 for quality management, ISO 14971 for risk management, and ISO 10993 for biocompatibility assessment, is essential to meet the strict requirements for medical device certification and market access [25-27].

Finally, strategic decisions must be made to pave the way for commercialization and make DRS accessible to healthcare providers. This includes comprehensive market analysis, devising pricing strategies, establishing distribution channels, and developing marketing strategies. Navigating these last steps will conclude the transition from prototype to practical implementation.

OTHER POSSIBLE APPLICATIONS

The findings of our research extend beyond spine surgical navigation, holding promise for various other minimally invasive surgery (MIS)

scenarios where DRS can distinguish tissues in multiple directions based on their composition. Studies have demonstrated the potential of DRS in tumor detection and margin assessment across multiple anatomical sites, including the bladder [28], bowels [29, 30], liver [31, 32], lung [33, 34], breast [35-39], and oral cavity [40]. Especially during biopsies, directional DRS could enhance tissue sampling and improve diagnostic accuracy. In anesthesia procedures, DRS facilitates needle guidance by detecting nerves, thereby ensuring accurate placement for reduced patient discomfort [41-44]. Moreover, DRS has been shown to enhance safety during procedures such as laser lithotripsy by aiding in the detection of kidney and bladder stones [45]. In laser surgery, DRS enables real-time tissue differentiation, allowing to automatically stop laser ablation upon reaching the next tissue layer [46, 47]. These diverse applications underscore the versatility and clinical relevance of DRS across medical specialties.

CONCLUDING REMARKS

Our research demonstrates that breaches during spinal fusion procedures can be effectively prevented by using a three-fiber probe capable of sensing in multiple directions, establishing DRS as a valid technology to support surgeons during spine surgery. The simple instrumentation of DRS and our miniaturization efforts have facilitated its integration into surgical instruments such as pedicle probes, a flexible probe, and a handheld device, proving the feasibility of this technology for real-time tissue feedback in surgical settings.

Hospitals stand to benefit from adopting breach detection technologies. Improved accuracy in pedicle screw placement reduces the need for revision surgeries, and expanding the eligibility for MIS offers advantages such as reduced soft tissue and muscle damage, blood loss, and surgical time, along with faster recovery times [48-51]. These benefits translate into substantial cost savings for healthcare facilities [52, 53].

While our most recent prototype addresses many practical challenges, further steps are necessary to achieve market readiness, and overcoming the remaining obstacles is crucial for promoting the adoption of DRS in

the operating room. The versatility of DRS across medical specialties opens new avenues for research and development beyond spinal fusion.

Ultimately, the usability of DRS-enhanced devices depends not only on their sensing capabilities but also on addressing surgical and mechanical factors. Collaboration among interdisciplinary teams of researchers, surgeons, and engineers is encouraged during the development process. On the path towards practical implementation, this collaborative approach ensures that DRS-based surgical guidance systems are tailored to meet clinical needs and align with surgeon preferences, rather than forcing surgeons to adapt their technique to the new system. Through such efforts, we can maximize the potential benefits of DRS to enhance accuracy and safety in spinal fusion surgery.

REFERENCES

1. Lee, Ronald. "The demographic transition: three centuries of fundamental change." Journal of economic perspectives 17.4 (2002): 167-190.

2. Beschloss, Alexander, et al. "Marked increase in spinal deformity surgery throughout the United States." Spine 46.20 (2021): 1402-1408.

3. Härtl, Roger, et al. "Worldwide survey on the use of navigation in spine surgery." World neurosurgery 79.1 (2013): 162-172.

4. Swamy, Akash, et al. "Diffuse reflectance spectroscopy, a potential optical sensing technology for the detection of cortical breaches during spinal screw placement." Journal of biomedical optics 24.1 (2019): 017002-017002.

5. Burström, Gustav, et al. "Diffuse reflectance spectroscopy accurately identifies the pre-cortical zone to avoid impending pedicle screw breach in spinal fixation surgery." Biomedical optics express 10.11 (2019): 5905-5920.

6. Fisher, Michael A. "Smart pedicle tool." US patent US 8249696 B2 (2007)

7. Swamy, Akash, et al. "Diffuse reflectance spectroscopy for breach detection during pedicle screw placement: a first in vivo investigation in a porcine model." BioMedical Engineering OnLine 19 (2020): 1-12.

8. Fisher, Carl, et al. "Perspective on the integration of optical sensing into orthopedic surgical devices." Journal of Biomedical Optics 27.1 (2022): 010601.

9. Farrell, Thomas J., et al. "A diffusion theory model of spatially resolved, steady-state diffuse reflectance for the noninvasive determination of tissue optical properties in vivo." Medical physics 19.4 (1992): 879-888.

10. Nachabé, Rami, et al. “Estimation of lipid and water concentrations in scattering media with diffuse optical spectroscopy from 900 to 1600 nm.” Journal of biomedical optics 15.3 (2010): 037015-037015.

11. Kanick, Stephen C., et al. “Method to quantitate absorption coefficients from single fiber reflectance spectra without knowledge of the scattering properties.” Optics letters 36.15 (2011): 2791-2793.

12. Hennessy, Ricky, et al. “Monte Carlo lookup table-based inverse model for extracting optical properties from tissue-simulating phantoms using diffuse reflectance spectroscopy.” Journal of biomedical optics 18.3 (2013): 037003-037003.

13. Pifferi, Antonio, et al. “Optical biopsy of bone tissue: a step toward the diagnosis of bone pathologies.” Journal of biomedical optics 9.3 (2004): 474-480.

14. Engelhardt, Alexander, et al. “Comparing classification methods for diffuse reflectance spectra to improve tissue specific laser surgery.” BMC medical research methodology 14 (2014): 1-15.

15. Dahlstrand, Ulf, et al. “Extended-wavelength diffuse reflectance spectroscopy with a machine-learning method for in vivo tissue classification.” PLoS One 14.10 (2019): e0223682.

16. Fanjul-Vélez, Félix, et al. “Application of classification algorithms to diffuse reflectance spectroscopy measurements for ex vivo characterization of biological tissues.” Entropy 22.7 (2020): 736.

17. Nguyen, Mayna H., et al. “Machine learning to extract physiological parameters from multispectral diffuse reflectance spectroscopy.” Journal of Biomedical Optics 26.5 (2021): 052912-052912.

18. Chan, Jireh Y. L., et al. “Mitigating the multicollinearity problem and its machine learning approach: a review.” Mathematics 10.8 (2022): 1283.

19. Arifler, Dizem, et al. "Optimal wavelength combinations for near-infrared spectroscopic monitoring of changes in brain tissue hemoglobin and cytochrome c oxidase concentrations." Biomedical Optics Express 6.3 (2015): 933-947.

20. Li, Celina L., et al. "Frameworks of wavelength selection in diffuse reflectance spectroscopy for tissue differentiation in orthopedic surgery." Journal of Biomedical Optics 28.12 (2023): 121207-121207.

21. de Kater, Esther P., et al. "Tsetse fly inspired steerable bone drill—a proof of concept." Frontiers in Bioengineering and Biotechnology 11 (2023): 1197940.

22. Clinical investigation of medical devices for human subjects – Good clinical practice. ISO 14155:2020, International Organization for Standardization, 2020.

23. Ergonomics of human-system interaction – Part 11: Usability: Definitions and concepts. ISO 9241-11:2018, International Organization for Standardization, 2018.

24. Medical devices – Part 1: Application of usability engineering to medical devices. IEC 62366-1:2015, International Organization for Standardization, 2015.

25. Medical devices – Quality management systems – Requirements for regulatory purposes. ISO 13485:2016, International Organization for Standardization, 2016.

26. Medical devices – Application of risk management to medical devices. ISO 14971:2019, International Organization for Standardization, 2019.

27. Biological evaluation of medical devices – Part 1: Evaluation and testing within a risk management process. ISO 10993-1:2018, International Organization for Standardization, 2018.

28. Koenig, Frank, et al. "Spectroscopic measurement of diffuse reflectance for enhanced detection of bladder carcinoma." Urology 51.2 (1998): 342-345.

29. Zonios, George, et al. "Diffuse reflectance spectroscopy of human adenomatous colon polyps in vivo." Applied optics 38.31 (1999): 6628-6637.

30. Baltussen, Elisabeth J. M., et al. "Using diffuse reflectance spectroscopy to distinguish tumor tissue from fibrosis in rectal cancer patients as a guide to surgery." Lasers in surgery and medicine 52.7 (2020): 604-611.

31. Spliethoff, Jarich W., et al. "In vivo characterization of colorectal metastases in human liver using diffuse reflectance spectroscopy: toward guidance in oncological procedures." Journal of biomedical optics 21.9 (2016): 097004-097004.

32. Keller, Alina, et al. "Diffuse reflectance spectroscopy of human liver tumor specimens-towards a tissue differentiating optical biopsy needle using light emitting diodes." Biomedical Optics Express 9.3 (2018): 1069-1081.

33. Evers, Daniel J., et al. "Diffuse reflectance spectroscopy: a new guidance tool for improvement of biopsy procedures in lung malignancies." Clinical lung cancer 13.6 (2012): 424-431.

34. Reich, Christian. "Side-looking lung biopsy device." US patent US 10405838 B2 (2015)

35. Cerussi, Albert, et al. "In vivo absorption, scattering, and physiologic properties of 58 malignant breast tumors determined by broadband diffuse optical spectroscopy." Journal of biomedical optics 11.4 (2006): 044005-044005.

36. Nachabé, Rami, et al. "Diagnosis of breast cancer using diffuse optical spectroscopy from 500 to 1600 nm: comparison of classification methods." Journal of biomedical optics 16.8 (2011): 087010-087010.

37. de Boer, Lisanne L., et al. "Fat/water ratios measured with diffuse reflectance spectroscopy to detect breast tumor boundaries." Breast cancer research and treatment 152 (2015): 509-518.

38. de Boer, Lisanne L., et al. "Towards the use of diffuse reflectance spectroscopy for real-time in vivo detection of breast cancer during surgery." Journal of translational medicine 16 (2018): 1-14.

39. Amiri, Sara A., et al. "Intraoperative tumor margin assessment using diffuse reflectance spectroscopy: the effect of electrosurgery on tissue discrimination using ex vivo animal tissue models." Biomedical Optics Express 11.5 (2020): 2402-2415.

40. Einstein, Gnanatheepam, et al. "Diffuse reflectance spectroscopy for monitoring physiological and morphological changes in oral cancer." Optik 127.3 (2016): 1479-1485.

41. Rathmell, James P., et al. "Identification of the Epidural Space with Optical Spectroscopy: An In Vivo Swine Study." The Journal of the American Society of Anesthesiologists 113.6 (2010): 1406-1418.

42. Balthasar, Andrea, et al. "Optical detection of peripheral nerves: an in vivo human study." Regional Anesthesia & Pain Medicine 37.3 (2012): 277-282.

43. Schols, Rutger M., et al. "Differentiation between nerve and adipose tissue using wide-band (350–1,830 nm) in vivo diffuse reflectance spectroscopy." Lasers in surgery and medicine 46.7 (2014): 538-545.

44. Langhout, Gerrit C., et al. "Nerve detection during surgery: optical spectroscopy for peripheral nerve localization." Lasers in medical science 33 (2018): 619-625.

45. Lange, Birgit, et al. "Stone/tissue differentiation during intracorporeal lithotripsy using diffuse white light reflectance spectroscopy: In vitro and clinical measurements." Lasers in surgery and medicine 46.8 (2014): 614-619.

46. Stelzle, Florian, et al. "In vivo optical tissue differentiation by diffuse reflectance spectroscopy: preliminary results for tissue-specific laser surgery." Surgical innovation 19.4 (2012): 385-393.

47. Bergauer, Bastian, et al. "Does laser surgery interfere with optical nerve identification in maxillofacial hard and soft tissue?—an experimental ex vivo study." Sensors 15.10 (2015): 25416-25432.

48. Lovecchio, Francis, et al. "Single-position Minimally Invasive Surgery for Correction of Adult Spinal Deformity." JAAOS-Journal of the American Academy of Orthopaedic Surgeons (2022): 10-5435.

49. Lokhande, Pramod V. "Full endoscopic spine surgery." Journal of Orthopaedics 40 (2023): 74-82.

50. Orosz, Lindsay D., et al. "The Role of Robot-Assisted MIS Spinal Deformity Surgery." Technical Advances in Minimally Invasive Spine Surgery: Navigation, Robotics, Endoscopy, Augmented and Virtual Reality. Singapore: Springer Nature Singapore, 2022. 311-320.

51. Yang, Wanliang, et al. "Meta-analysis of the clinical effect of MIS-TLF surgery in the treatment of minimally invasive surgery of the orthopaedic spine." Computational Intelligence and Neuroscience 2022 (2022).

52. Watkins IV, Robert G., et al. "Cost-effectiveness of image-guided spine surgery." The open orthopaedics journal 4 (2010): 228.

53. Menger, Richard P., et al. "A cost-effectiveness analysis of the integration of robotic spine technology in spine surgery." Neurospine 15.3 (2018): 216.

ACKNOWLEDGMENTS

I want to express my heartfelt thanks to those who have supported and guided me throughout my PhD. Jenny, you are an inspiring person, and I feel very lucky to have been supervised by you. Benno, you always left just enough breadcrumbs for me to find my way through the labyrinth of this project, and I am very grateful for your direction. Paul, thank you for providing a fresh perspective on my topic all throughout my PhD. To my committee, I appreciate your time and presence during my defense. Thank you for being part of this important moment.

Akash and Sara, thank you for providing me with a starting point and introducing me to the fascinating field of tissue optics, which I had the pleasure of exploring over the past four years. Adrian and Erik, I am grateful for the medical expertise you brought to my research, as discussions with you were always a helpful reality check. David and Remi, as our skilled instrument makers, not a single working prototype would have ever seen the light of day without your practical advice and steady hands. Helge, Tess, Stijn, Famke, Justin, May, and Benjamin, working alongside students who are not only capable but also truly nice individuals like you made my job all the more enjoyable.

Esther, working on this project with you was a true gamechanger for me, as I never had to struggle alone. Jette, your company made the workspace feel pleasantly alive at 8 am (and the rest of the day). Vera, I'm grateful for the energy that you and your octopus arms brought to our office. Having wonderful colleagues like you has been an absolute bliss.

Kirsten, it was a pleasure to work alongside you in the office from the first day of my PhD to the last. Mostafa, thank you for sharing your enthusiasm for your research with us. Niko, your big smile as you walk into our office has brightened my day on many occasions. To all my other colleagues whose names I won't list here for fear of omitting someone, thank you for the wonderful company!

Thank you, Robert & Johanna, for making De Groene Haven a home away from home. Maxi & Toni, thank you for not only being great friends during the challenges of the pandemic, but also for the spontaneous late-night

runs to the pharmacy. Emily & Max, navigating the parenting journey with you has created a special bond, and I'm grateful that we've done so without ever comparing or judging. Knowing you lovely people makes it so much harder to bid farewell to the Netherlands...

Bea, your interest in my work and constant inquiries about my progress have meant a lot to me, and I admire the precision and modesty you bring to everything you do. Kerstin, Saša & Lina, Tale, Emma & Simon, Ena, thank you all for your longstanding friendship. The happy moments and memories we have created together have been invaluable during the completion of my PhD.

Papa, Mama & Nantje, thank you for always being there to support me, for inspiring me with your resilience and wisdom, and for being individuals I deeply admire and look up to. Max, thank you for being my incredibly unromantic romantic partner through it all. Knowing you are always by my side is what kept me sane over the past years, and I look forward to everything that's yet to come. Luna, you brought immense joy to my life, and I couldn't have imagined completing this PhD without you.

I look forward to what lies ahead, knowing I carry the support of so many amazing people with me. Thank you all for being part of my life!

CURRICULUM VITÆ

Merle Sophie Losch was born on the 5th of March, 1996, in Aachen, Germany. After graduating from High School in 2013, she started her academic journey in Mechanical Engineering at RWTH Aachen University. From 2015 to 2017, she relocated to Marseille, France, to participate in the double degree program "Top Industrial Managers for Europe" at École Centrale Marseille, from which she holds a Diplôme d'Ingénieur.

After completing her Bachelor's degree with an internship at HalioDx focusing on cell detection and tissue classification in Digital Pathology, she continued her education by pursuing a Master's degree in Mechanical Engineering at RWTH Aachen University. She graduated with a Master's thesis titled "Synergistic Guidance of a Cooperative Robot for the Alignment of a Drilling Guide during Spinal Surgery", for which she was awarded the Springorum Commemorative Coin in recognition of passing the Master examination with distinction.

In January 2020, she joined the BioMechanical Engineering Department at Delft University of Technology in The Netherlands, focusing her PhD research on enhancing spinal fusion surgery through the application of tissue optics for surgical guidance.

SCIENTIFIC OUTPUT

Losch, M. S., Swamy, A., Elmi-Terander, A., Edström, E., Hendriks, B. H., & Dankelman, J. (2021). Proton density fat fraction of the spinal column: an MRI cadaver study. *BioMedical Engineering OnLine*, 20(1), 1-11.

Losch, M. S., Kardux, F., Dankelman, J., & Hendriks, B. H. (2022). Steering light in fiber-optic medical devices: a patent review. *Expert Review of Medical Devices*, *19*(3), 259-271.

Losch, M. S., Kardux, F., Dankelman, J., & Hendriks, B. H. (2023). Diffuse reflectance spectroscopy of the spine: improved breach detection with angulated fibers. *Biomedical Optics Express*, 14(2), 739-750.

Losch, M. S., Heintz, J. D., Edström, E., Elmi-Terander, A., Dankelman, J., & Hendriks, B. H. (2024). Fiber-optic pedicle probes to advance spine surgery through Diffuse Reflectance Spectroscopy. *Bioengineering*, 11(1), 61.

Losch, M. S., Dankelman, J., & Hendriks, B. H. (2024). Seeing from a new angle: design of a sideways-looking fiber-optic probe to advance spine surgery. In *Advanced Biomedical and Clinical Diagnostic and Surgical Guidance Systems XXII* (Vol. 12831, pp. 46-53). SPIE.

Losch, M. S., Visser, B. E., Dankelman, J., & Hendriks, B. H. (2024). A handheld fiber-optic tissue sensing device for spine surgery. *PLoS One*.

CONFERENCE CONTRIBUTIONS

8th Dutch BME Conference (January 2021)
oral presentation
"Proton density fat fraction of the spinal column: an MRI cadaver study"

iSMIT 2021/22 (May 2022)
poster presentation
"Non-perpendicular breach detection for spinal fusion surgery"

Biophotonics '22 (June 2022)
poster presentation
"Enhancing spine surgery by Diffuse Reflectance Spectroscopy with obliquely oriented fibers"

9th Dutch BME Conference (January 2023)
oral presentation
"Real-time tissue feedback for spine surgery using a customized fiber-optic probe"

European Conferences on Biomedical Optics 2023 (June 2023)
poster presentation
"Real-time tissue feedback for spine surgery using a customized DRS probe"

Photonics West 2024 (January 2024)
oral presentation
"A sharp insight: fiber-optic awls to advance spine surgery through Diffuse Reflectance Spectroscopy"

Photonics West 2024 (January 2024)
oral presentation
"Seeing from a new angle: design of a sideways-looking fiber-optic probe to advance spine surgery"


TU Delft